THE INFLUENCE OF PROCESSING ON MICROSTRUCTURE AND PROPERTIES OF IRON ALUMINIDES

R. N. Wright, J. K. Wright, and M. T. Anderson

Idaho National Engineering and Environmental Laboratory
Lockheed Martin Idaho Technologies Company
Idaho Falls, ID 83415-2218

ABSTRACT

Oxide dispersion strengthened (ODS) iron aluminide alloys based on Fe3Al have been formed by reaction synthesis from elemental powders followed by hot extrusion. The resulting alloys have approximately 2.5% by volume Al_2O_3 particles dispersed throughout the material. A proper combination of extrusion temperature, extrusion ratio, and post-consolidation heat treatment results in a secondary recrystallized microstructure with grain sizes greater than 25mm. ODS material with 5% Cr addition exhibits approximately an order of magnitude increase in time to failure at 650°C compared to a similar alloy without the oxide dispersion. Addition of Nb and Mo along with Cr results in decreased minimum creep rates, however, the time to rupture is greatly reduced due to fracture at low strains initiated at large Nb particles that were not put into solution. The activation energy for creep in the 5% Cr ODS material is on the order of 210kJ/mole and the power law creep exponent is 9-9.5. Transmission electron microscopy examination of the substructure of deformed samples indicates some formation of low angle dislocation boundaries, however, most of the dislocations are pinned at particles. The TEM observations and the value of the creep exponent are indicative of dislocation breakaway from particles as the rate controlling deformation mechanism. The TEM results indicate that particles smaller than about 100nm and larger than about 500nm do not contribute significantly to dislocation pinning.

INTRODUCTION

Iron aluminides near the composition Fe_3Al display outstanding resistance to sulfidation and are attractive for possible applications in fossil fired plants.[1] Although these alloys were investigated extensively in the 1960's, brittle room temperature behavior resulted in little industrial interest. More recent studies have identified the brittle behavior as a result of a hydrogen effect associated with water vapor. In the absence of water vapor, Fe_3Al has reasonable tensile ductility at room temperature.[2] More significantly from an applications point of view, it has been found that room temperature tensile elongation of greater than 20% can be achieved under ambient conditions through alloying with 2-5% Cr and control of the microstructure to retain the maximum amount of B2 order.

Despite major advances in increasing the ambient temperature ductility, relatively poor elevated temperature properties is still a limitation for applications of iron aluminides.[3] It has been suggested that as a result, iron aluminide coatings on high strength ferrous alloys may be an attractive alternative.[4] In addition a number of strategies for increasing the creep resistance of alloys based on Fe_3Al have been suggested. Alloying with refractory metal additions, principally Mo, Nb and Zr, has been shown to be effective, particularly if fine refractory carbides can be formed.[5] Experience with oxide dispersion strengthened nickel based and FeCrAl based alloys has suggested that the creep resistance of Fe_3Al can be dramatically improved by dispersion of fine stable oxide particles. The most common approach to oxide dispersion strengthening is through high energy ball milling of prealloyed powders with a rare earth oxide, followed by hot consolidation. An alternative approach, reported here, is to use the natural tendency of reaction synthesis from elemental powders to result in a finely distributed oxide to improve the creep resistance of Fe_3Al + 5%Cr.[6]

DISCUSSION OF CURRENT ACTIVITIES

Experimental Procedure

Reaction synthesized material was made using carbonyl iron (8μm diameter), helium gas atomized aluminum (10μm diameter) and chromium (1-5μM diameter) powders, mixed in proper proportions to yield Fe-28Al-5Cr (all compositions are given in this paper in atomic percent). Reaction between the elemental iron and aluminum, and solution of the chromium in the iron aluminide, occurred during a two hour thermal treatment at 1100°C under flowing argon. This process resulted in porous pre-forms that were subsequently sealed in steel cans and extruded in a 16:1 reduction in area ratio at 900°C. Test specimens were machined from the extruded material and heat treated at 1200°C to form large (>25mm in length) grains elongated in the test direction, by secondary recrystallization. Appropriate extrusion ratio, extrusion temperature, and grain growth temperature were selected based on previous work.[7]

Creep tests were performed in laboratory air in constant load testing frames with applied stresses from 50 to 135MPa, and temperatures from 600 to 800°C. Many of the tests were carried out to failure to obtain creep rupture data. A few tests were interrupted to obtain specimens for examination using transmission electron microscopy. Those samples were held under the applied stress while the furnace was turned off and the specimen allowed to cool to room temperature to prevent relaxation of the dislocation structure. In order to determine the power law creep exponent, additional tests were conducted by allowing steady state creep to be attained and subsequently jumping the stress to higher values while maintaining constant temperature. For these tests to be valid it is assumed that the sample remains isostructural; given the relatively small creep strains observed in these tests and the small jumps in stress, this condition is valid for the values reported below.

Results and Discussion

Creep data for the dispersion strengthened material and conventional powder metallurgy processed (P/M) material of the same composition are given in Table 1. Larson-Miller plots for conventional P/M Fe_3Al and the dispersion strengthened material are shown in Figure 1. The increased time to rupture is clearly evident from this plot. Note that the P/M alloy considered in the Larson-Miller plot contains only 2% Cr, rather than the 5% in the dispersion strengthened material. We have shown previously the increasing the Cr from 2 to 5% reduces the creep rupture life, however, since the dispersion strengthened material has poor room temperature ductility, 5% Cr was used to obtain maximum tensile properties.

Assuming that the dispersion strengthened material follows conventional power law creep behavior, the apparent activation energy for creep can be determined from the data as plotted in Figure 2. The value determined in this study is 210kJ/mole ±20 kJ/mole. This value compares reasonably well with values determined for binary Fe_3Al, 280kJ/mole.[8] Although this value is in agreement with the self-diffusion activation energy for iron in Fe_3Al, 204kj/mol, the apparent value determined from the plot should be corrected somewhat for the threshold stress associated with particle pinning.[9] The corrected value has not yet been determined because an accurate temperature dependent shear modulus is not available. The apparent activation energy reported here is more than an order of magnitude larger than the value reported by McKamey for carbide strengthened Fe_3Al.[10] The reason for this large difference is not yet known.

The power law stress exponent can be determined from the data plotted in Figure 3. The slope of the plots yields an approximate average value of 9.5. This value is much greater than commonly observed for metals and alloys (4-5), however, large stress exponents have been reported for a number of dispersion strengthened materials.[11] Arzt et al., found values of >50 for particle strengthened Al alloys and on the order of 13 for NiAl containing several different dispersions.[12-13] It has also been reported that values of 13-14 are found in high energy ball milled FeAl alloys.[14] The value determined here is also in reasonable agreement with the value of 10 reported for carbide strengthened Fe_3Al by McKamey et al.[10]

Table 1. Creep properties of conventional P/M and oxide dispersion strengthened materials.

Material	Heat Treatment (°C-time)	Test Temp. (°C)	Applied Stress (MPa)	Creep Rate (s^{-1})	Time to Rupture (hrs)
P/M	N/A	500	137.9	4.72E-09	3398
P/M	N/A	500	275	7.32E-08	125
P/M	N/A	600	76	138	418
P/M	N/A	600	103	275	72
P/M	N/A	600	138	2.08E-06	15
P/M	N/A	650	34	2.36E-08	1464
P/M	N/A	650	76	5.99E-07	47
ODS	1200-1 hr	650	75.8	4.97E-09	512.8
ODS	1200-1 hr	675	78.5	4.82E-08	62
ODS	1200-1 hr	700	50	4.86E-09	255.8
ODS	1200-1 hr	800	50	1.33E-08	15
ODS	1200-1 hr	600	50	8.33E-11	>4400
ODS	1200-1 hr	600	75.8	2.08E-09	2527.4
ODS	1200-1 hr	650	50	2.5E-10	>2100
ODS	1200-1 hr	675	50	9.17E-10	856.3
ODS	1200-1 hr	625	50	6.94E-9	N/A
ODS	1200-1 hr	625	60	1.67E-09	N/A
ODS	1200-1 hr	625	110	1.02E-06	N/A
ODS	1200-1 hr	625	75.8	8.64E-09	N/A
ODS	1200-1 hr	625	100	4.42E-07	N/A
ODS	1200-1 hr	650	60	3.22E-09	N/A
ODS	1200-1 hr	650	100	9.03E-07	N/A
ODS	1200-1 hr	675	60	8.75E-09	N/A
ODS	1200-1 hr	675	85	7.0E-07	N/A

Dislocation structures were examined in several samples deformed in creep to different total strains. There was some evidence of recovery of dislocation structures into low angle boundaries, Figure 4, however, the majority of dislocations were found to be uniformly distributed throughout the microstructure. A representative region of a sample deformed to about 10% plastic strain and cooled under load to pin the dislocations is shown in Figure 5. Note in the figure that the majority of dislocations are pinned at particles that are on the order of 100nm in diameter or greater.

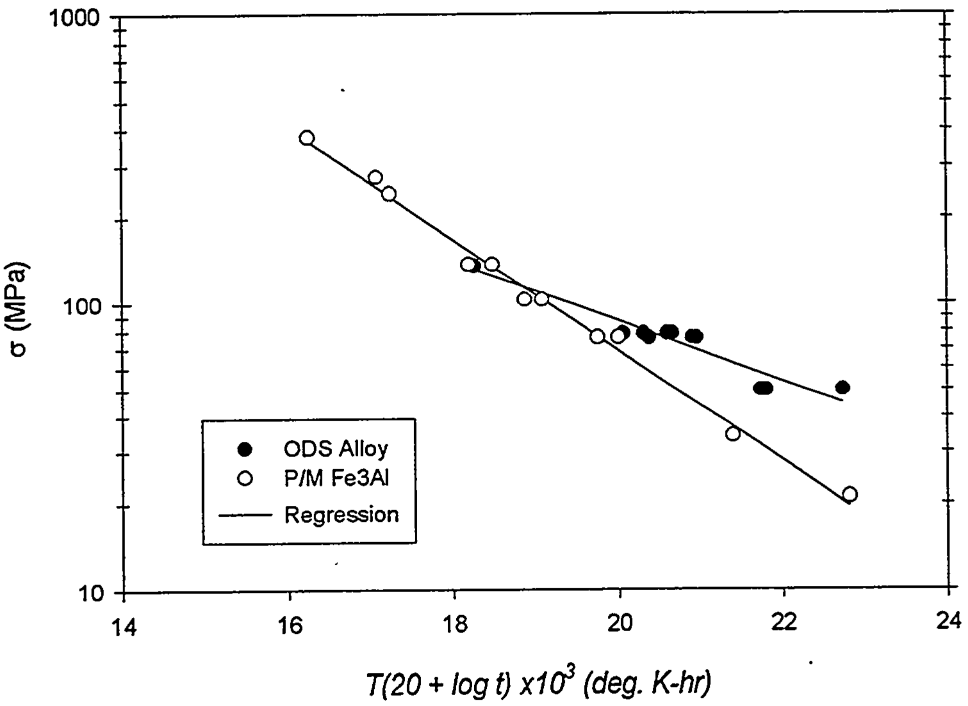

Figure 1. Larson-Miller plots for powder metallurgy and dispersion strengthened materials.

The Burgers vector of dislocations active in Fe_3Al during creep deformation is somewhat controversial. It has been reported that <111> superdislocations and <100> dislocations that are perfect in the B2 structure are both mobile under creep conditions.[6] A Burgers vector analysis was carried out in the current study, however, with the zone axes that could be accessed in the heavily textured material the results could not differentiate unambiguously between the two types of dislocation. It does appear that many of the dislocations observed in the dispersion strengthened material deformed in creep above 600°C were superdislocations, suggesting at least some fraction of the pinned dislocations were of the <111> type.

It is clear form the TEM results that the interaction between the particles and dislocations was attractive, rather than repulsion from strain fields associated with dislocations, for example. The unit process responsible for improved creep resistance in these materials therefore appears to be dislocation climb and breakaway from pinning particles. This particle pinning mechanism is consistent with the relatively high value of the power law creep exponent (≈9) that was determined for these alloys. There was no evidence of dislocation loop formation around particles that might suggest that an alternative, Orowan looping, process was active.

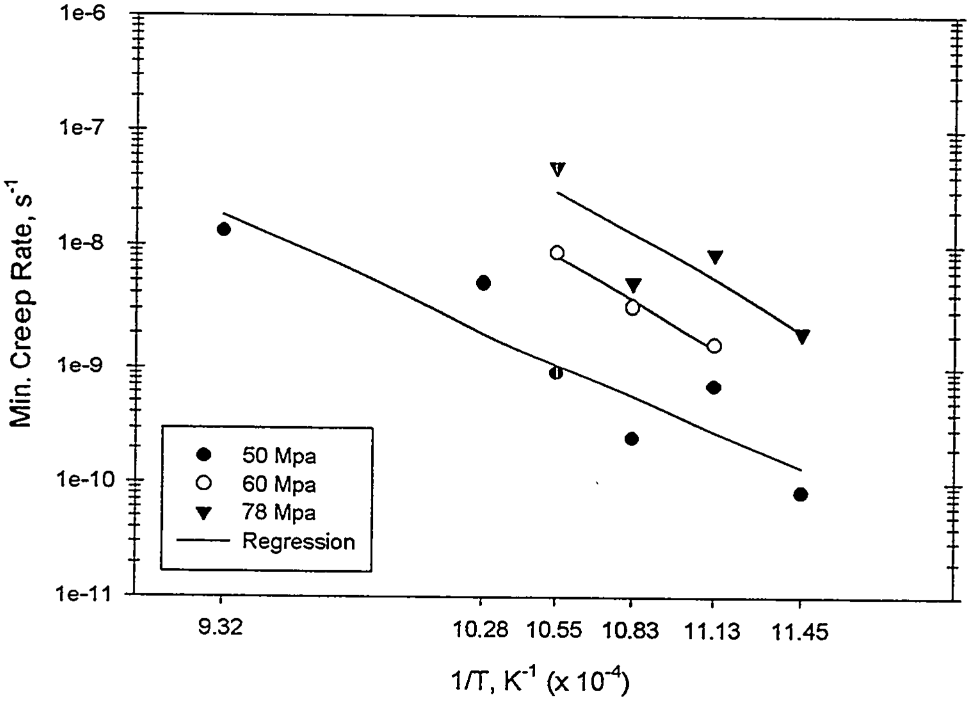

Figure 2 Minimum creep rate as a function of reciprocal temperature for three stress levels.

Additions of refractory metals to the Fe_3Al based alloys have been shown to increase the resistance to creep.[10] This effect can occur due to increasing the critical temperature or solution strengthening, however, the most significant increase in time to rupture appears to be as a result of precipitation of fine carbides. Since transition metal carbides are probably not stable with respect to coarsening at temperatures above about 800°C no effort was made in this study to incorporate their effect. An attempt was made to improve the creep resistance of the matrix material by additions of about 2% Mo and Nb. An improvement in minimum creep rate was observed in some cases compared to the dispersion strengthened material with only Cr additions, however, large elemental Nb particles remained undisolved in the matrix which initiated fracture, resulting in short time to rupture values. Additional alloys have been processed with additions of very fine particle sizes of Mo and Nb which are expected to result in complete dissolution of the alloying elements, testing of these alloys has recently begun.

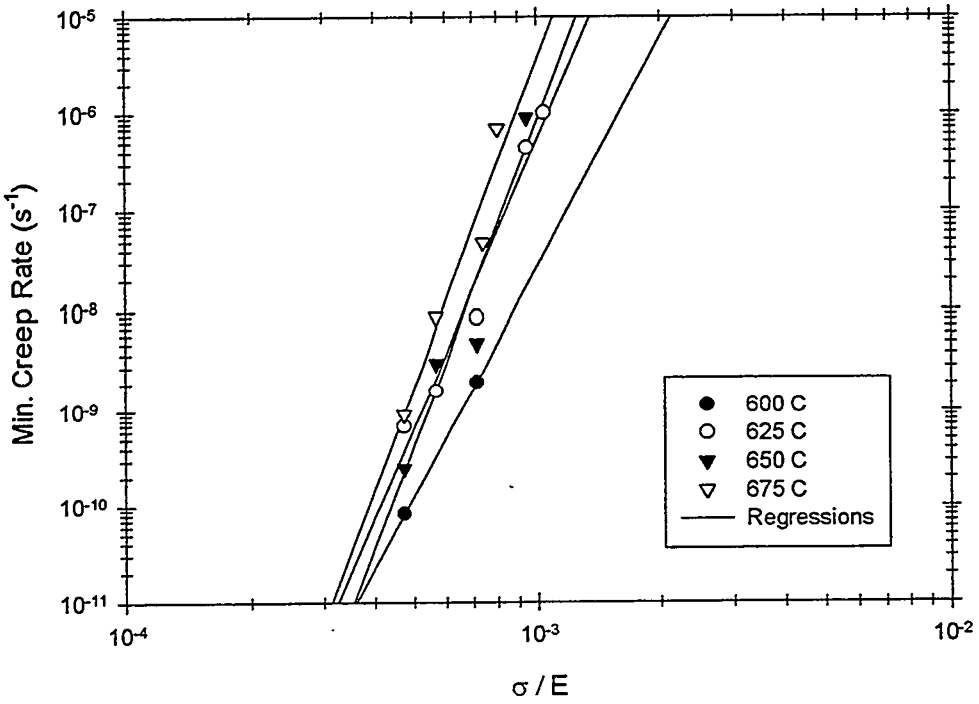

Figure 3. Minimum creep rate plotted as a function of the applied stress normalized to Youngs modulus.

Conclusions

A dispersion of fine oxides from reaction synthesis of Fe_3Al from elemental powders significantly increases the time to rupture of the material compared to conventional powder metallurgy processing. Increased creep lifetime is a result of reduced minimum, or steady state, creep rates. The elongation to failure is reduced in the dispersion strengthened material compared to conventional powder metallurgy alloy. The TEM results show that here is an attractive interaction between the oxide particles and dislocations, which results in a power law creep exponent of ≈9. This value is about twice that normally found for metals and alloys, and is indicative of particle strengthening. The activation energy for creep was determined to be 210kj/mole, a value that is approximately the same as Fe_3Al without the particle dispersion and roughly equal to the activation energy for self-diffusion of iron in the intermetallic.

Figure 5. Dislocation structure in a sample deformed to 5% plastic strain at 675°C and a stress of 78MPa.

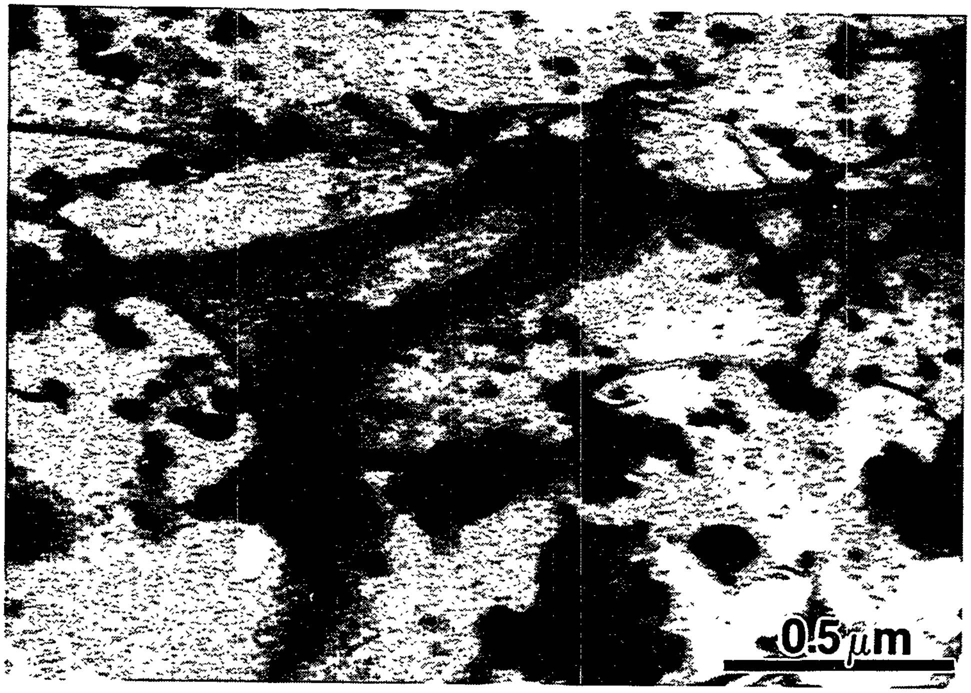

Figure 6. Dislocation structure in a sample deformed to 10% plastic strain at 675°C and a stress of 50MPa.

REFERENCES

1. C. G. McKamey, J. H. DeVan, P. F.Tortorelli, and V. K. Sikka, "A Review of Recent Developments in Fe_3Al Based Alloys", J. Mater Res., Vol. 6, 1991, pp. 1779-1804.
2. C. T. Liu, C. G. McKamey and E. H. Lee, "Environmental Effects on Room Temperature Ductility and Fracture in Fe_3Al", Scripta Metall. Et Mater., Vol. 24, 1990, pp. 385-390.
3. C. R. Clark, R. N. Wright, J. K. Wright and B. H. Rabin, "Elevated Temperature Mechanical Properties of Reaction Synthesized Fe_3Al". Scripta Metall. Et Mater., Vol. 32, 1995, pp. 1883-1887.
4. R. N. Wright, J.R. Fincke, W. D. Swank, D. C. Haggard and C. R. Clark, "The Influence of Process Parameters on the Microstructure and Properties of Fe_3Al Based Coatings", Elevated Temperature Coatings: Science and Technology, N. B. Dahotre, et al., eds., TMS, 1995, pp. 157-166.
5. R. N. Wright and J. K. Wright, "The Influence of Processing on the Microstructure and Properties of Iron Aluminides", Proc. 10th Conf. On Fossil Energy Materials, ORNL, 1996, pp. 373-380.
6. D. G. Morris, M. Nazmy and C. Noseda, "Creep Resistance of a New Alloy Based on Fe_3Al", Scripta Metall et Mater., Vol. 31, 1994, pp. 173-178.
7. T. M. Lillo, R. N. Wright, B. H. Rabin and J. K. Wright, "Microstructure and Properties of Reaction Synthesized Iron Aluminides", Inter. Conf. On Heat Resistant Alloys II, K. Natesan, et al., eds., ASM International, 1995, pp. 579-587.
8. J. A. Jimenez and G. Frommeyer, "Creep Behavior of Intermetallic Fe-Al and Fe-Al-Cr Alloys, Mater. Sci. Eng., Vol. A220, 1996, pp. 93-99.
9. Z. S. Tokei, J. Bernardini, P. Gas and D. L. Beke, "Volume Diffusion of Iron in Fe_3Al: Influence of Ordering", Acta Metall. Et Mater., Vol. 45, 1997, pp. 541-546.
10. C. G. McKamey and P. J. Maziasz, "Effect of Heat Treatment at 1150°C on Creep Properties of Alloy FA-180", Proc. 10th Conf. On Fossil Energy Materials, ORNL, 1996, pp. 215-221.
11. A. M. Brown and M. F. Ashby, "On the Power Law Creep Equation", Scripta Meatll., Vol. 14, 1980, pp. 1297-1302.
12. E. Arzt, E. Gohring and P. Grahle, "Dispersion Strengthened Intermetallics by Mechanical Alloying: Creep Results and Dislocation Mechanisms", Mater. Res. Soc. Proc. Vol. 288, 1993, pp. 861-866.
13. J. Rrosler, R. Joos and E. Arzt, "Microstructure and Creep Properties of Dispersion-Strengthened Aluminum Alloys", Metall. Trans., Vol. 23A, 1992, pp. 1521-1314.
14. K. Wolski, F. Thevenot and J. Le Coze, "Influence of Nanometric Oxide Dispersion on Creep Resistance of ODS FeAl Prepared from Prealloyed Powders", Scripta Meatll. Et Mater., Vol 34, 1996, pp. 815-823.

MECHANISMS OF DEFECT COMPLEX FORMATION AND ENVIRONMENTAL-ASSISTED FRACTURE BEHAVIOR OF IRON ALUMINIDES

B. R. Cooper[1], L.S. Muratov[1], B.S.-J. Kang[2], and K.Z. Li[2]

[1] Physics Department

[2] Mechanical and Aerospace Engr. Dept.

West Virginia University

Morgantown, WV 26506

ABSTRACT

Iron aluminide has excellent corrosion resistance in high-temperature oxidizing-sulfidizing environments; however, there are problems at room and medium temperature with hydrogen embrittlement as related to exposure to moisture. In this research, a coordinated computational modeling/experimental study of mechanisms related to environmental-assisted fracture behavior of selected iron aluminides is being undertaken. The modeling and the experimental work will connect at the level of coordinated understanding of the mechanisms for hydrogen penetration and for loss of strength and susceptibility to fracture. The focus of the modeling component at this point is on the challenging question of accurately predicting the iron vacancy formation energy in $Fe_3A\ell$ and the subsequent tendency, if present, for vacancy clustering. We have successfully performed, on an *ab initio* basis, the first calculation of the vacancy formation energy in $Fe_3A\ell$. These calculations include lattice relaxation effects which are quite large. This has significant implications for vacancy clustering effects with consequences to be explored for hydrogen diffusion. The experimental work at this stage has focused on the relationship of the choice and concentration of additives to the improvement of resistance to hydrogen embrittlement and hence to the fracture behavior. For this reason, comparative crack growth tests of FA-186, FA-187, and FA-189 iron aluminides (all with basic composition of Fe-28$A\ell$-5Cr, at % with micro-alloying additives of Zr, C or B) under, air, oxygen, or water environment have been performed. These tests showed that the alloys are susceptible to room temperature hydrogen embrittlement in both B2 and DO_3 conditions. Test results indicated that FA-187, and FA-189 are intrinsically more brittle than FA-186.

INTRODUCTION

Because of their excellent corrosion resistance in high temperature oxidizing-sulfidizing environments in combination with low cost and other advantages, iron aluminides are of great potential use in fossil energy technology, however, there are problems at room and medium temperatures with hydrogen embrittlement as related to exposure to moisture.[1,2] In this research, a coordinated computational modeling/ experimental study of mechanisms related to environmental-assisted fracture behavior of selected iron aluminides is being undertaken. The modeling and the experimental work will connect at the level of coordinated understanding of the mechanisms for hydrogen penetration and for loss of strength and susceptibility to fracture.

The vacancy formation behavior and the likelihood of the vacancies clustering and/or forming complexes with additives (or impurities) or other defects will play a central role in determining susceptibility to fracture, both directly and indirectly via the effects on crucial diffusion processes. Therefore the focus of the modeling component at this point is on the challenging question of accurately predicting the iron vacancy formation energy in $Fe_3A\ell$ and the subsequent tendency, if present, for vacancy clustering. We have successfully performed, on an *ab initio* basis, the first calculation of the vacancy formation energy[3] in $Fe_3A\ell$. These calculations include lattice relaxation effects. Interestingly, there are two types of iron sites and hence two rather different vacancy formation energies. Both types of vacancy site involve quite large atomic movements, of the order 13-15% of the unrelaxed relative position, for the nearest neighbors.

For the experimental component, environmental-assisted fracture behavior of three iron aluminides (designated as FA-186, FA-187, and FA-189, all with various alloy additives such as Zr, C,or B) were investigated to study the effect of alloy additives on fracture behavior, in particular, resistance to hydrogen embrittlement. Crack growth tests of the iron aluminides subjected to constant tensile loading in air, oxygen or water environment were conducted. Moire interferometry was applied to obtain full-field crack-tip displacements, from which crack extension, crack growth rate, and the stress intensity factor were evaluated. Evidence of moisture embrittlement for the three iron aluminides was observed. We found that the presence of a small amount of moisture is sufficient to cause embrittlement. The comparative tests also showed that specimens in B2 condition have slightly better crack resistance than those in DO_3 condition. Test results indicated that FA-187 and FA-189 are intrinsically more brittle than FA-186 in both B2 and DO_3 conditions. SEM fractographic and optical microstructural analyses relevant to failure analysis of the iron aluminides was also performed and is discussed below.

COMPUTATIONAL MODELING

Atomistic computational modeling is being undertaken to find the preferred geometries and the formation energies of iron vacancies and vacancy pairs (Fe-Fe) for FeAℓ and $Fe_3A\ell$. An indication of vacancy clustering in $Fe_3A\ell$, with consequences for dislocation behavior, may be important for understanding the role of dislocation-assisted diffusion in the hydrogen embrittlement mechanism.

A fully quantum mechanical full-potential LMTO technique, including force calculations, is being applied to find the formation energies of iron vacancies and vacancy pairs (Fe-Fe) in FeA$\ell$and $Fe_3A\ell$. The method being used is our well established fully quantum mechanical full potential linear combination of muffin-tin-orbitals (LMTO) technique.[4,5] This is an *ab initio* all-electron technique with full relativistic corrections included. To assure high accuracy we have implemented an augmented basis through use of multiple κ's and energy windows.[5,6] Initially we have found the preferred unrelaxed geometry through use of total energy minimization. To treat relaxation effects for this transition metal system, we have implemented a force methodology based on our full-potential LMT total energy technique and have applied this to vacancy formation energies in both FeAℓ and $Fe_3A\ell$. We will next calculate the divacancy binding energy (or the absence thereof).

The vacancy energy is calculated by first calculating the total energy of the initial perfect (without vacancy) supercell. We then subtract from that the energy the sum of the total energy of the supercell with a vacancy plus the energy contribution of the removed atom. The atomic energy contribution is taken from the bulk energy of the element (iron) scaled to reproduce the total energy of the intermetallic compound.

In $Fe_3A\ell$ there are two types of iron site. Type A has eight iron nearest neighbors at a distance of $\sqrt{3}\,a/4$; while type B has four iron and four aluminum nearest neighbors. This then leads to there being two types of vacancy and the possibility of three types of divacancy (AA, AB, BB). We have carefully examined the density of states for the two types of iron site (see Fig. 1), and they are quite different.

In order to have sufficient degrees of freedom to fully investigate the effects of lattice relaxation, we have used a 32-atom supercell (eight formula units of $Fe_3A\ell$). For the type A iron sites, the unrelaxed vacancy formation energy is 3.8 eV, and there is an energy lowering of 0.8 eV caused by lattice relaxation. This gives a net vacancy formation energy of 3.0 eV. Interestingly, the changes in bond lengths are quite large, up to 13% of the nearest neighbor distance. For the type B sites, the unrelaxed vacancy formation energy is 2.8 eV, and there is an energy lowering of 1.01 eV associated with lattice relaxation. For B sites, this gives a net vacancy formation energy of 1.79 eV. Again, the changes in bond lengths are quite large, up to 15% of the nearest neighbor distance.

Significantly for the possibility of vacancy clustering, our preliminary calculations in the 32-atom supercell indicate a strong interaction between vacancies of about 0.3 eV. During the coming year we will refine this estimate by performing the divacancy calculations for much larger supercells.

EXPERIMENTAL PROGRAM

Materials

Alloys used in this study were fabricated at Oak Ridge National Laboratory (ORNL) by vacuum induction melting and casting into graphite molds. The ingots were then hot forged (two passes, 25% per pass) at 1000°C followed by hot rolled at 800°C for seven passes (15% per pass) to produce finished plate thickness of 6.35 mm. The finished plates were either heat treated at 900°C for one hour then air quenched to produce partially ordered B2 structure or heat treated at 900°C for one hour followed by 550°C for 72 hours then air quenched to produce DO_3 structure. Table 1 shows the alloy composition of FA-186, FA-187 and FA-189.

Single-edge-notched (SEN) specimens were cut from the plates using an EDM machine and specimen surfaces were hand-polished with fine grid sandpapers followed by thorough solution cleaning. Figure 2 shows the test specimen geometry. The notch of each specimen was cut using 0.1 mm diameter EDM wire with notch direction parallel to the rolling direction.

Test Apparatus

An environmental materials testing chamber was constructed to conduct crack growth tests of iron aluminides using moire interferometry under controlled gas content (air, argon, hydrogen gas or dry oxygen) environments. The chamber can also be filled with water to conduct crack growth test in water. Figure 3 shows a schematic drawing of the environmental test chamber. For crack growth tests under oxygen environment, the chamber was first pumped down to about 10^{-2} torr, and oxygen with research purity of 99.999% was filled in the chamber at a pressure of 1.2 atm. The pumping and filling cycle was done 4 or 5 times before the crack growth test. Additionally, a moisture trap with absorption capacity of 25 grams H_2O was put inside the chamber to reduce the residual moisture in the test environment. It should be noted that unless the chamber is pumping down to a high vacuum state (say 10^{-8} torr), some amount of residual moisture is still present in the chamber, particularly, near the EDM-cut crack tip region. We did a preliminary residual gas measurement of the chamber under the above mentioned "oxygen" environment using RGA and estimate that the partial pressure of residual moisture and hydrogen is about 0.25-0.04 and 0.06-0.05 times of the atmospheric air, respectively.

Moire interferometry is capable of high sensitivity full-field surface deformation measurement[7]. At WVU, we have demonstrated that moire interferometry can be applied to study environmental assisted cracking problems.[8,9] Figure 4 shows a schematic drawing of the optical setup for moire interferometry test with the environmental chamber mounted on the optical bench.

Crack Growth Tests

Table 2 shows the test matrix. As shown, a total of sixteen comparative crack growth tests under various environments were conducted. Figure 5 shows representative moire fringe patterns of FA-189 under air environment. Figure 6 shows representative SEM fractographs of alloys tested in air environment. Figure 7 shows the measured crack extension versus time data, and Figure 8 shows the measured crack growth rate versus applied stress intensity factor.

For alloy FA-186 tested in air or oxygen condition, multiple cracks were formed as soon as the initial crack started to grow. The extension of these multiple microcracks formed an expanding damage zone which grew stably leading to final failure. This feature of extensive multiple microcracking was not found for alloys FA-187 and FA-189. Instead, a clear single crack growth pattern was observed (e.g. Figure 5).

As shown in Table 2, for alloys FA-186, FA-187, and FA-189 tested in water environment, accelerated effect of hydrogen embrittlement was observed and resulted in lower fracture toughness and fast fracture behavior, i.e. no slow stable crack growth was observed comparing to the specimens tested in air or oxygen environment. Test results in Table 2 also showed that with the same applied stress intensity factor, specimens tested in oxygen lasted 3 to 9 times longer than those tested in air, indicating the effect of moisture embrittlement for all three iron aluminides. Also, specimens with partially ordered B2 condition have slightly better fracture resistance than those in DO_3 condition for all three alloys. However, the susceptibility of hydrogen embrittlement varies among the test alloys. As shown in Figures 7 and 8, crack growth tests of the ternary alloy FA-186 tested in air showed some small amount of increased crack growth rate compared to those tested in oxygen; only crack growth test in water showed significant effect of hydrogen embrittlement for FA-186. This is not the case for alloys FA-187 and FA-189, which showed substantial faster crack growth rate in air than when tested in oxygen.

Overall, our test results indicate that among the three alloys, the ternary alloy FA-186 has the best fracture resistance, highest fracture toughness and least sensitivity to hydrogen embrittlement (Table 2). This finding is quite surprising since the purpose of micro-alloying addition to the ternary alloy (0.5% Zr0.05%C (FA-187) or 0.5% Zr0.05%C0.005%B (FA-189)) is to enhance its resistance to hydrogen embrittlement. It should be noted that recently Alven and Stoloff[10] conducted fatigue crack growth tests of several iron aluminides including FA-186 and FA-187 under air, oxygen, vacuum or 1.3 atm hydrogen environment. Their results, in contrast, showed that FA-187 has lower fatigue crack growth rate than that of FA-186. Since hydrogen embrittlement is a diffusion-controlled process and past studies have indicated that low strain rate loading can promote hydrogen embrittlement[1], the 0.5%Zr0.05%C addition (FA-187) may provide stronger grain boundary bonding for better fatigue resistance than the base ternary alloy (FA-186), but under constant static loading condition and with its smaller grain size, at the high-stress crack tip region, initial intergranular microcracks may assist the diffusion of atomic hydrogen (which is generated due to the chemical reaction of the aluminum atoms in the aluminides react with moisture, $2Al+3H_2O$ - Al_2O_3+6H) along crack-tip grain boundaries which subsequently caused accelerated dislocation motion at cleavage plans that resulted in brittle cleavage fracture. Further research is needed to clarify or validate the above assertion.

Failure characteristics of the tested alloys are tabulated in Table 3. We roughly divided the fractured surface into three areas corresponding to the changes of failure mode. For alloys FA-187 and FA-189, initial crack growth always started with intergranular mode (e.g. Figure 6) then shifted to mixed intergranular/transgranular cleavage mode and finally to transgranular failure. As the moisture content is increased in the test environment (i.e. from oxygen to air to water), we observed an increased intergranular failure pattern in area 2.

For ternary alloy FA-186, except for the sample tested in water which showed intergranular mode in area 1, transgranular cleavage is the dominate failure mode. However, the sample tested in air had rougher cleavage facets (i.e. more tilt and twist boundaries). In hydrogen-free environment cleavage generally takes place along crystallographic planes with the lowest packing density, and thus resulted in larger cleavage facets (Figure 6). While in hydrogen-containing environment, hydrogen embrittlement is proposed to be associated with dislocation transport of hydrogen[2], which occurred along crystallographic planes with the highest packing density, i.e. more rougher cleavage facets as we observed in the fractographic analyses.

Our test results indicated that FA-187 and FA-189 are intrinsically more brittle than FA-186. As discussed in ref. 11, the level of zirconium addition needs to be carefully controlled. Some amount of zirconium addition (say about 0.1%) is beneficial to promote scale adhesion for protection against corrosion in harsh environment; however, too much zirconium addition (such as 0.5% Zr in FA-187) may produce intrinsically brittle iron aluminide alloy.

The purpose of adding a small amount of boron in FA-189 was to improve the strength of grain boundaries so that intergranular failure can be minimized. However, our test results indicate just the opposite. This may be related to the composition of the alloy. In a similar system, $Ni_3A\ell$, where the stoichiometric proportion of binary alloy is 25%$A\ell$, it has been reported[12-14] that when boron is introduced to $Ni_3A\ell$ alloy, aluminum has to be reduced to 23-24% in order to strengthen grain boundaries and to optimize ductility. Similar modifications of stoichiometric proportion may be necessary for FA-189. Systematic experiments are needed to determine the best stoichiometric proportion of $Fe_3A\ell$ when boron is added to the material system.

CONCLUSIONS

Interestingly, there are two types of iron sites and hence two rather different vacancy formation energies. Both types of vacancy site involve quite large atomic movements, of the order 13-15% of the unrelaxed relative position, for the nearest neighbors. Significantly for the possibility of vacancy clustering, our preliminary calculations in the 32-atom supercell indicate a strong interaction between vacancies of about 0.3 eV. During the coming year we will refine this estimate by performing the divacancy calculations for much larger supercells.

Comparative crack growth tests of FA-186, FA-187 and FA-189 iron aluminides under air, oxygen or air environment were conducted and results showed substantial difference of crack-tip deformation profile and crack growth rate among the alloys. Test results also showed that with the same applied stress intensity factor, specimens tested in oxygen lasted 3 to 9 times longer than those tested in air, indicating the effect of moisture embrittlement for all three iron aluminides. Alloys with partially ordered B2 structure have slightly better fracture resistance than those in DO_3 structure. Finally, our test results indicated that FA-187 and FA-189 are intrinsically more brittle than FA-186.

ACKNOWLEDGMENTS

This research is sponsored by the U.S. Department of Energy, Office of Fossil Energy, Advanced Research and Technology Development (AR&TD) Materials Program at the Oak Ridge National Laboratory under contract no. SUB-19X-ST547C with Lockheed Martin Energy Systems, Inc. Additional support from the WVU NRCCE is also acknowledged. Technical assistance from Dr. C.T. Liu from ORNL is greatly appreciated.

REFERENCES

1. N.S. Stoloff and C.T. Liu,"Environmental Embrittlement of Iron Aluminides - Review," Intermetallics, 2, pp.75-87, (1994).
2. A. Castagna, D.A. Alven and N.S. Stoloff, "Environmental Embrittlement of Iron Aluminides under Cyclic Loading Condition," Proceedings of the Ninth Annual Conference on Fossil Energy Materials, Oak Ridge, TN, pp. 377-386, May 16-18 (1995).
3. L.S. Muratov and B.R. Cooper, Bull. Am. Phys. Soc. 42, 737 (1997).
4. D.L. Price and B.R. Cooper, Phys. Rev. B 39, 4945 (1989).
5. D.L. Price, B.R. Cooper and J.M. Wills, Phys. Rev. B 46, 11368 (1992).
6. D.L. Price, J.M. Wills and B.R. Cooper, Phys. Rev. B 48, 15301 (1993).
7. D. Post, Moire interferometry, Chapter 7 in SEM, Handbook on Experimental Mechanics, ed. A.S. Kobayashi. Prentice-Hall, Englewood Cliffs, NJ, pp.314-387, (1987).
8. F.X. Wang and B.S.-J. Kang, "Moire Interferometry in Liquid Medium," SEM, Proceeding of the VII International Congress on Experimental Mechanics, PP.1711-1716, Las Vegas, NA, June 8-11 (1992).

9. B.S.-J. Kang, G. Zhang, P. Liu and M. Ellathur, "Stress Accelerated Grain Boundary Oxygen Embrittlement on Creep Crack Growth of Ni-base Superalloys", 1995 ASME Winter Conference, San Francisco, CA, November, 20-24 (1995).
10. D.A. Alven and N.S. Stoloff, "The Influence of Composition on Environmental Embrittlement of Iron Aluminides," Proceedings of the Tenth Annual Conference on Fossil Energy Materials, Oak Ridge, TN, pp. 225-235, May 14-16 (1996).
11. C.G. McKamey, P.J. Maziasz and Y. Marrero-Santos, "Effects of Composition and Heat Treatment at 1150^0C on Creep-Rupture Properties of Fe_3Al-based Alloys," Proceedings of the Ninth Annual Conference on Fossil Energy Materials, Oak Ridge, TN, pp. 369-376, May 16-18 (1995).
12. J.T. Guo, C. Sum, H. Li, Z.Y. Zhang, Y.J. Tang, and Z.Q. Hu, Mater. Res. Soc. Symp. Proc. Vol.213, pp.655-659, (1991).
13. J.A. Horton and M.K. Miller, Mater. Res. Soc. Symp. Proc. Vol.81, pp.105-110, (1987).
14. H.P. Karnthaler, R. Kozubski, W. Pfeiler, and C. Renteberger, Mater. Res. Soc. Symp. Proc. Vol.364, pp.309-314, (1995).

Table 1 Chemical Composition of Iron Aluminides (at %)

Alloy	Fe	$A\ell$	Cr	Zr	C	B
FA-186	balance	28	5			
FA-187	balance	28	5	0.5	0.05	
FA-189	balance	28	2	0.5	0.05	0.005

Table 2 Test Matrix

Iron aluminide	Specimen	Structure Condition	Initial Crack	Environment	Initial K $MPa\sqrt{m}$	Lasting Time
FA-186	86-1	B2	FP	Air	36.9	7 min
	86-5	B2	FP	Dry Oxygen	36.8	21 min
	86-10	DO3	EDM	Air	25 28.3	94 min[c] 1 min
	86-9	DO3	EDM	Dry Oxygen	25 28.7	19 hr[d] 21 min
	86-w1	DO3	EDM	Water	13.35 22.12	2 hr[d] 8 second
FA-187	87-1	B2	EDM	Air	25	3.5 min
	87-5	B2	EDM	Dry Oxygen	25	15 min
	87-8	DO3	EDM	Air	25	2 min
	87-7	DO3	EDM	Dry Oxygen	25	18 min
	87-w1	DO3	EDM	Water	15.43	46 second
FA-189	89-2	B2	EDM	Air	17.36	7 min
	89-1	B2	EDM	Dry Oxygen	17.36	20 min
	89-7	DO3	EDM	Air	17.36	3 min
	89-6	DO3	EDM	Dry Oxygen	17.36	12 min
	89-w1	DO3	EDM	Water	13.1	60 second
	89-w2	DO3	EDM	Water	20.76	8 second

[a] All tests were conducted at room temperature;

[b] FP: Fatigue Pre-cracked; EDM: Electron-Discharge Machining;

[c] Slow crack growth;

[d] Almost no crack growth.

Table 3. Failure mode and illustration of the fractured surfaces studied

Alloy	Specimen	Environment	Area 1	Area 2	Area 3
FA-186	86-1	Air	mixed	mixed	transgranular
	86-5	Dry Oxygen	mixed	transgranular	transgranular
	86-10	Air	mixed	mixed	transgranular
	86-9	Dry Oxygen	mixed	transgranular	transgranular
	86-w1	Water	intergranular	mixed	transgranular
FA-187	87-1	Air	intergranular	mixed	mixed
	87-5	Dry Oxygen	intergranular	mixed	transgranular
	87-8	Air	intergranular	mixed	transgranular
	87-w1	water	intergranular	intergranular	mixed
	87-7	Dry Oxygen	intergranular	transgranular	transgranular
FA-189	89-2	Air	intergranular	mixed	transgranular
	89-1	Dry Oxygen	intergranular	transgranular	transgranular
	89-7	Air	intergranular	mixed	transgranular
	89-6	Dry Oxygen	intergranular	transgranular	transgranular
	89-w2	water	intergranular	intergranular	mixed

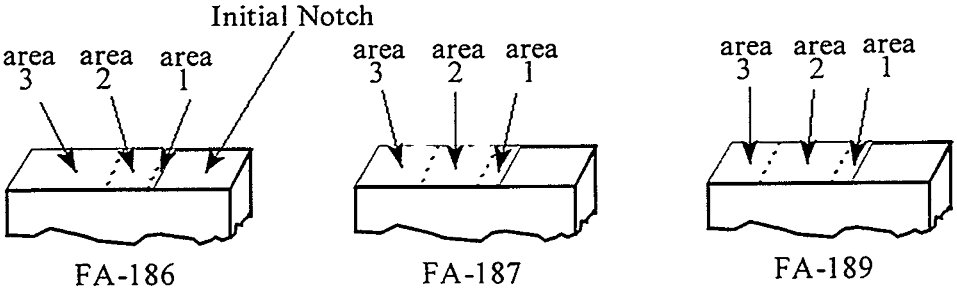

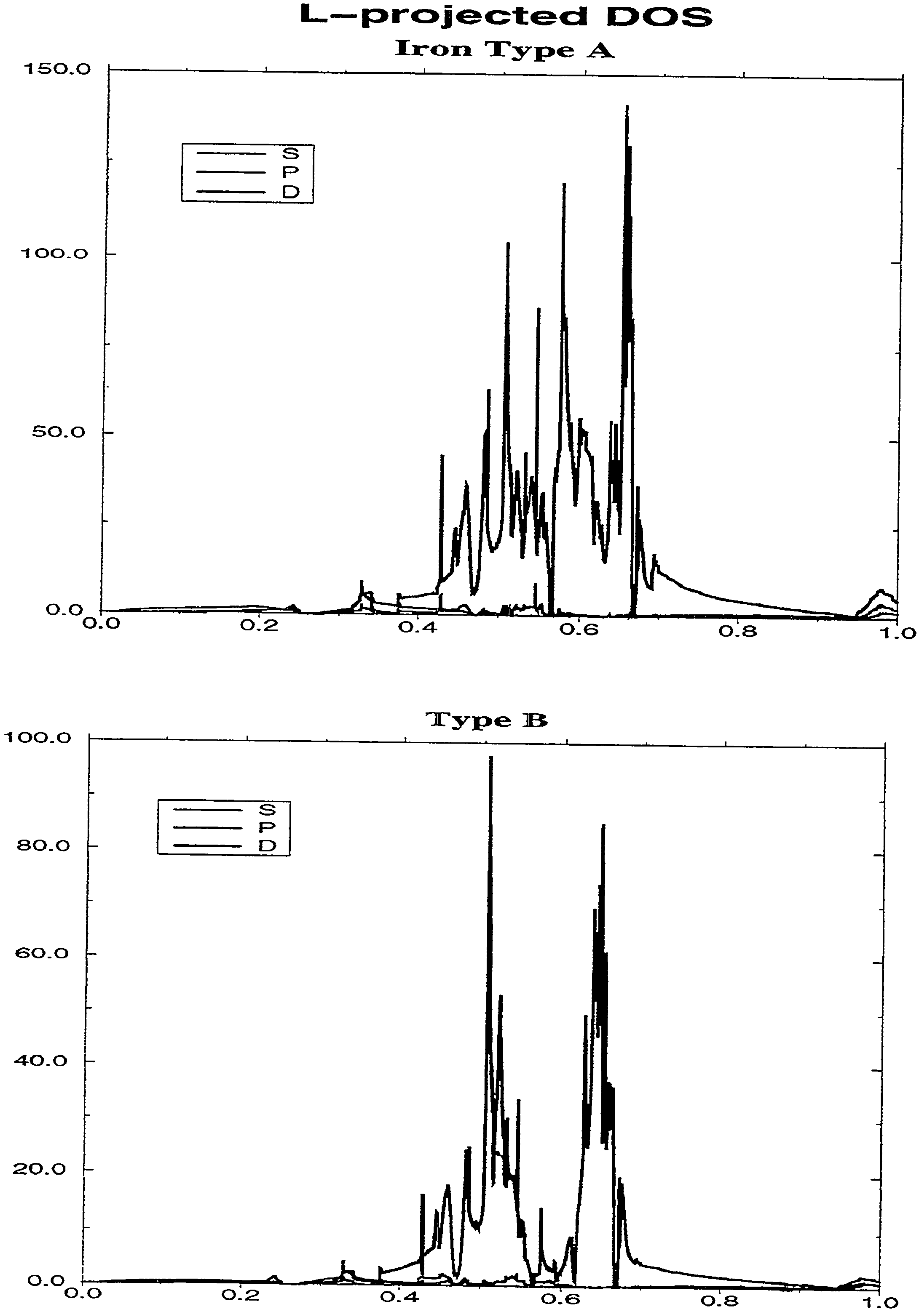

L−projected DOS

Iron Type A

Type B

Fig. 1

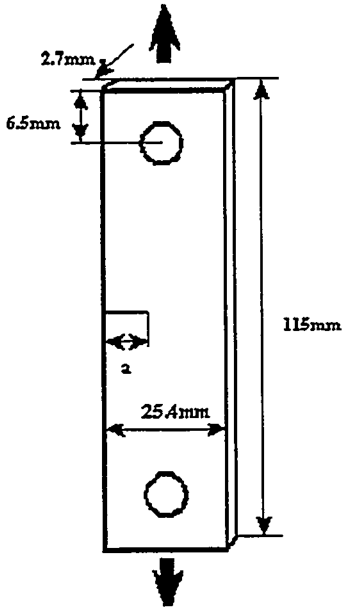

Fig.2 Single-edge-notched specimen

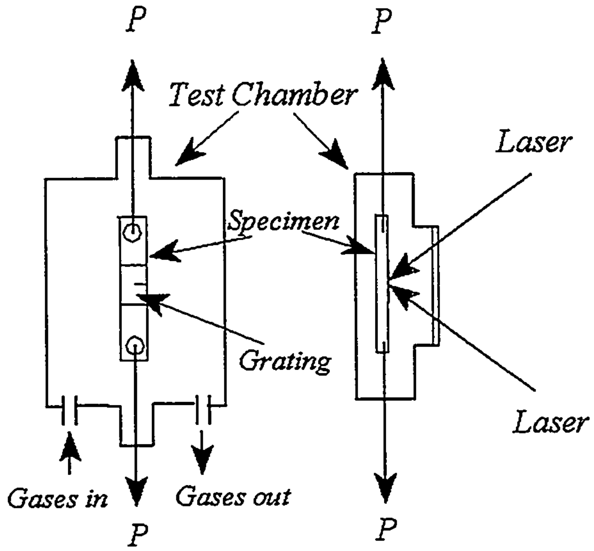

Fig.3 Schematic drawing of the enviromental testing chamber

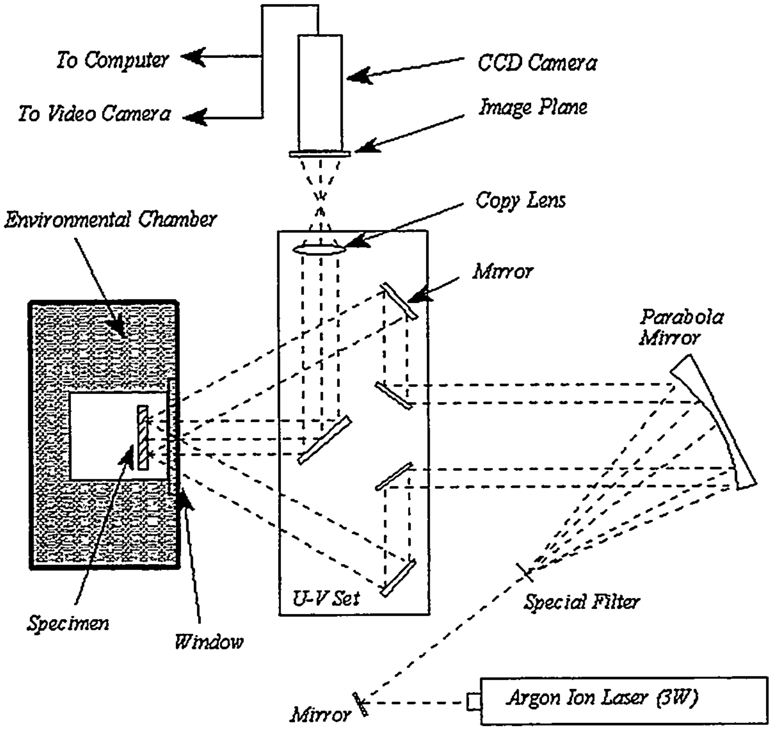

Fig.4 Optical setup for moire interferometry test

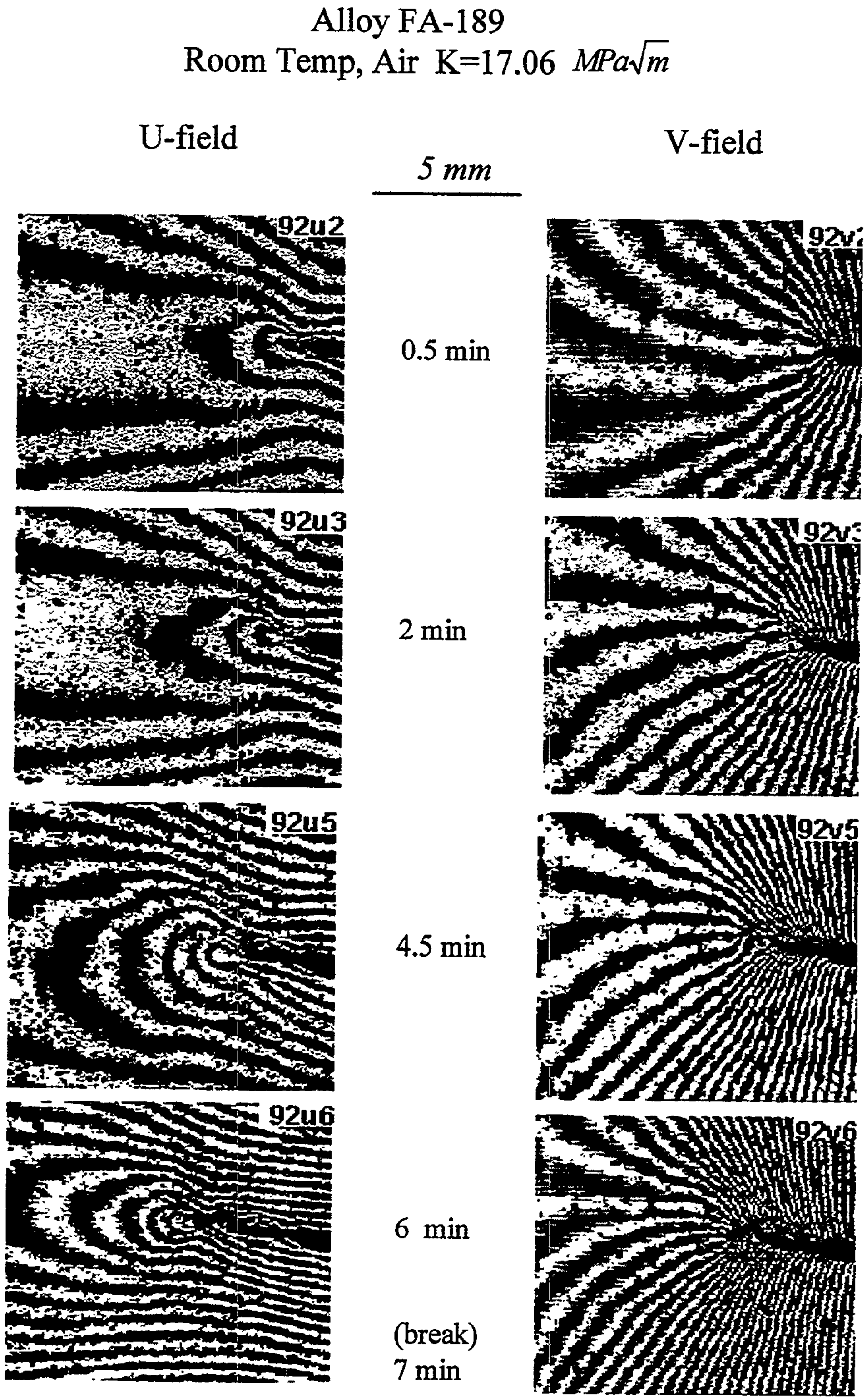

Fig. 5 u- and v- displacement fields of alloy FA-189 SEN specimen tested in air

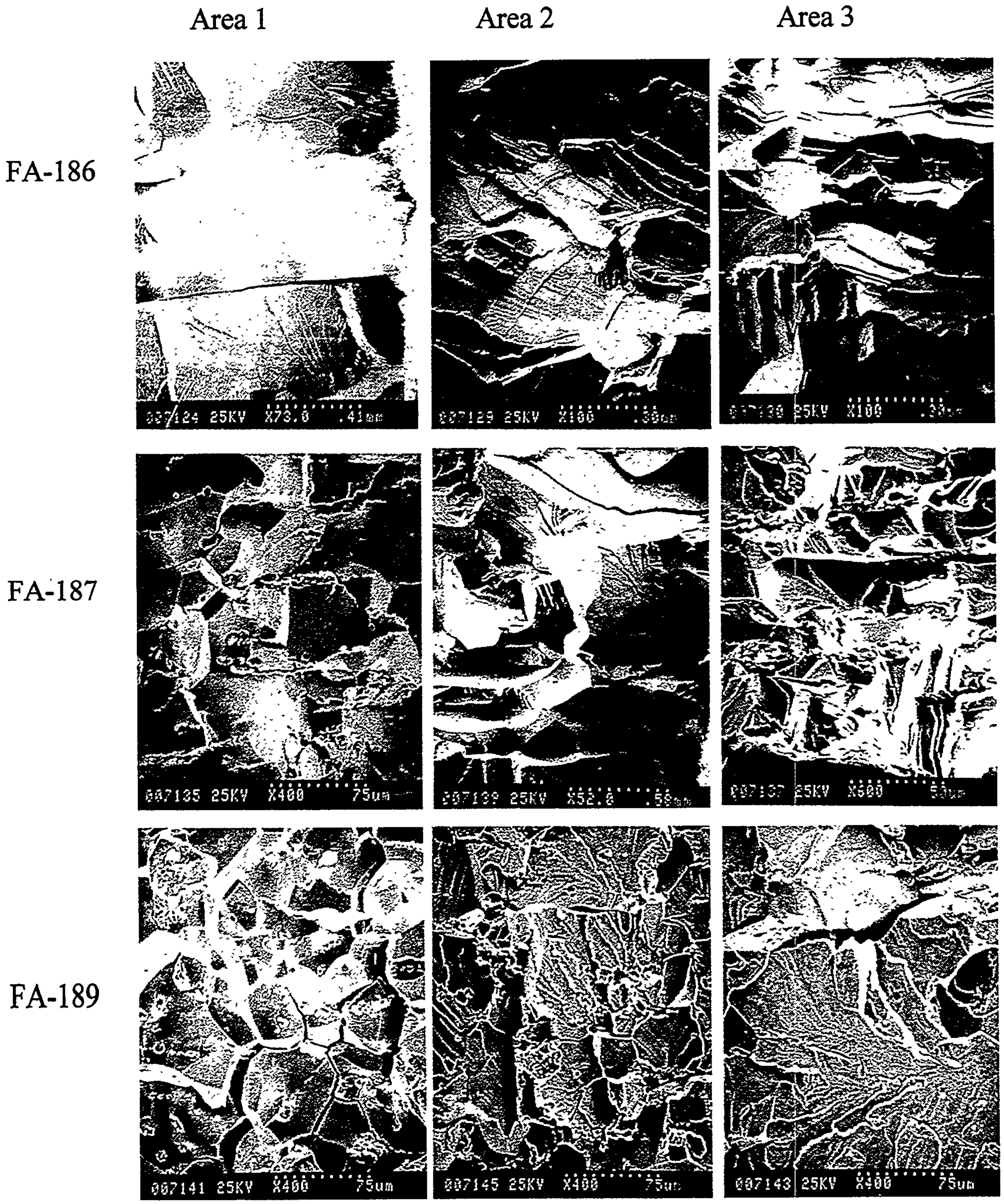

Fig.6 Representive fractographies for FA-186, FA-187 and FA-189 tested in the air environment

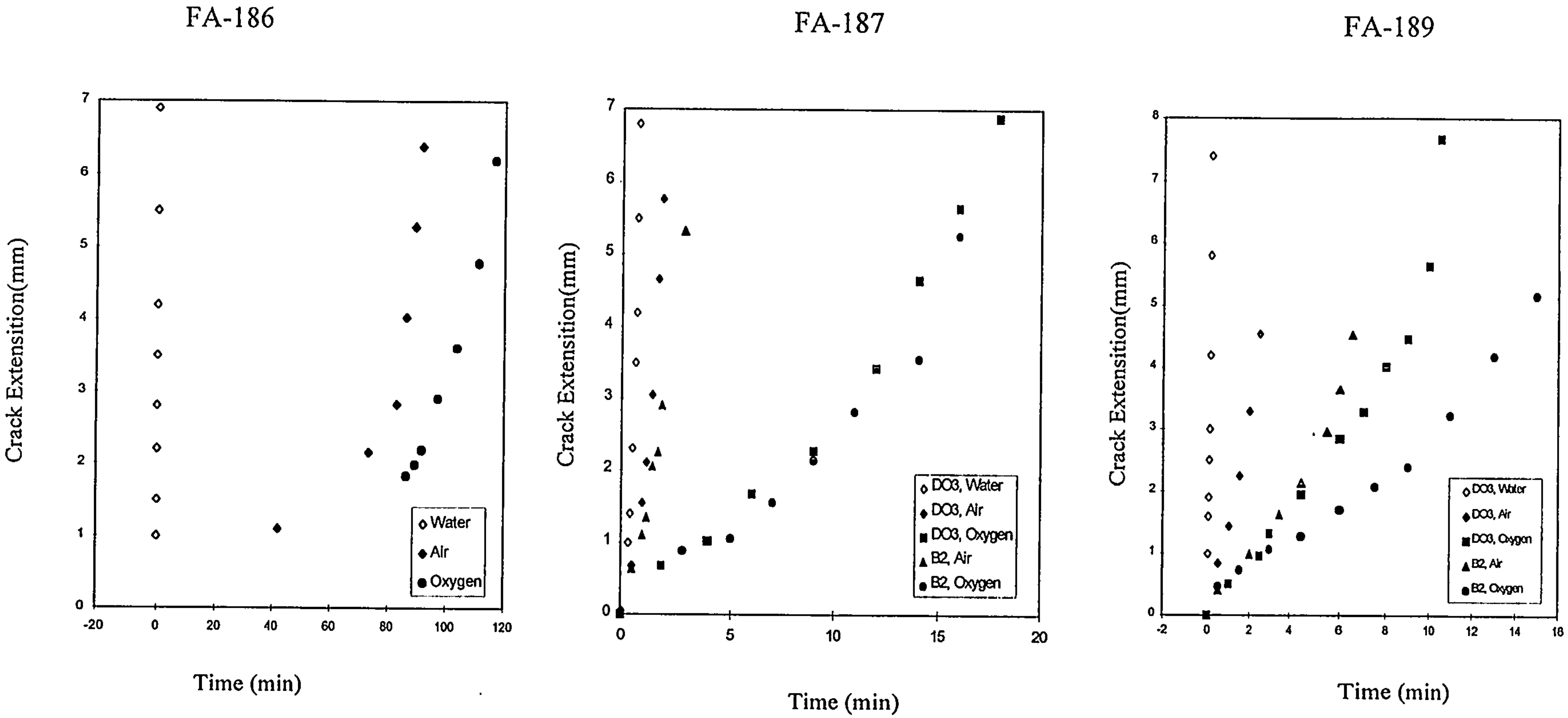

Fig.7 Crack ExtensionVesus Time

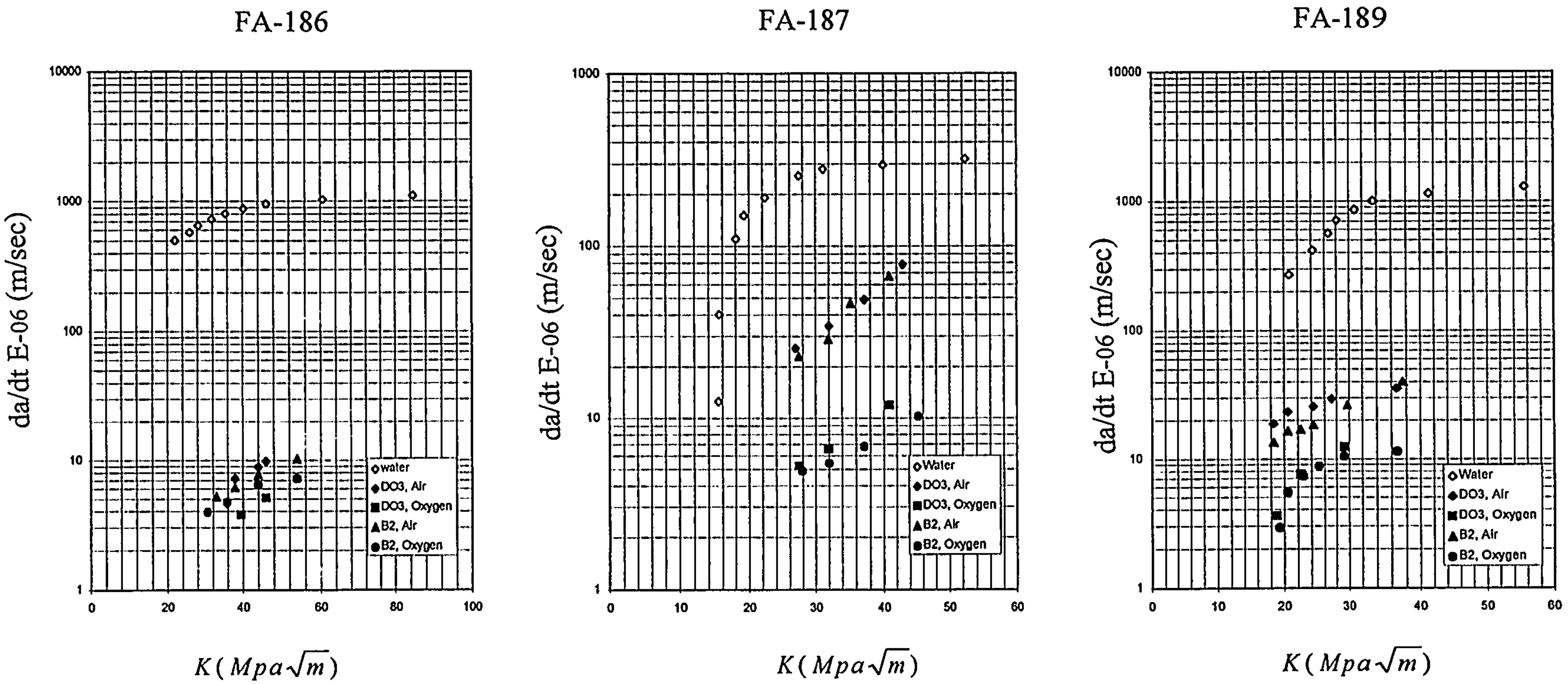

Fig.8 Environmental crack growth rate for FA-186, FA-187 and FA-189

ULTRAHIGH TEMPERATURE INTERMETALLIC ALLOYS

M. P. Brady, J.H. Zhu, C. T. Liu, P. F. Tortorelli, J.L. Wright, C.A. Carmichael, and L.R. Walker

Metals and Ceramics Division
Oak Ridge National Laboratory
Oak Ridge, Tennessee, U. S. A.

ABSTRACT

A new family of Cr-Cr_2X based alloys with fabricability, mechanical properties, and oxidation resistance superior to previously developed Cr-Cr_2Nb and Cr-Cr_2Zr based alloys has been identified. The new alloys can be arc-melted/cast without cracking, and exhibit excellent room temperature and high-temperature tensile strengths. Preliminary evaluation of oxidation behavior at 1100°C in air indicates that the new Cr-Cr_2X based alloys form an adherent chromia-based scale. Under similar conditions, Cr-Cr_2Nb and Cr-Cr_2Zr based alloys suffer from extensive scale spallation.

INTRODUCTION

The objective of this work is to develop a new generation of structural materials based on intermetallic alloys for use at high-temperatures in advanced fossil energy conversion systems. Target applications of such ultrahigh strength alloys include hot components (for example, air heat exchangers) in advanced energy conversion systems and heat engines. However, these materials may also find use as wear-resistant parts in coal handling systems (for example, nozzles), drill bits for oil/gas wells, and valve guides in diesel engines.

The developmental effort to date has focused on the Cr_2Nb and Cr_2Zr Laves phases[1-6]. Such Laves phases possess high melting points[7-9] and offer the potential for exceptional high-temperature strength[1-5]. However, they are extremely brittle at ambient temperatures[1-5,8]. In order to improve ambient temperature mechanical properties, two-phase "CN" alloys based on a soft Cr-rich solid solution phase reinforced with the hard Cr_2Nb or Cr_2Zr Laves phases have been developed[1-5].

For some Cr-Cr_2Nb based alloys, very high strengths at temperatures of 1200°C have been obtained[1,2]. However, improvements in ambient-temperature toughness and ductility have been modest[1,2]. This is thought to be due in part to thermal expansion mismatch between the Cr solid solution phase and the Cr_2Nb Laves phase, which leads to defects during fabrication, and extensive precipitation of the Cr_2Nb phase in the Cr solid solution phase[1].

The $Cr-Cr_2Zr$ system shows better fabricability and crack resistance than the $Cr-Cr_2Nb$ system, possibly due to a smaller mismatch of the coefficients of thermal expansion of the Cr solid solution and Laves phases[1]. The solubility of Zr in Cr is also much lower than that of niobium[9], which prevents extensive Cr_2Zr Laves phase preciptation in the Cr solid solution phase. However, the $Cr-Cr_2Zr$ based alloys have poor oxidation resistance, and generally tend to be weaker at high-temperatures than the $Cr-Cr_2Nb$ based alloys[1]. Significant property improvements in the $Cr-Cr_2Zr$ based alloys beyond those already achieved appear unlikely.

The metallurgical insights gained from the study of the $Cr-Cr_2Nb$ and $Cr-Cr_2Zr$ systems have provided the basis for the selection of a promising new $Cr-Cr_2X$ system with superior properties. Current efforts are focused on compositional optimization of alloys based on this new system. This report presents an overview of microstructural characterization, mechanical properties, and oxidation behavior for a near-optimized $Cr-Cr_2Zr$ based alloy and several promising new $Cr-Cr_2X$ based alloys.

ALLOY PREPARATION AND PROCESSING

CN alloys based on the $Cr-Cr_2Zr$ and $Cr-Cr_2X$ systems weighing 400-500 g were prepared by arc melting and drop casting in a copper mold (2.5 cm diam x 7.6 cm long) preheated to 200°C. Small 40 g castings of $Cr-Cr_2X$ based alloys were also prepared by arc melting and drop casting in a chilled copper mold. High-purity chromium and other metal chips were used as charge materials. In particular, the $Cr-Cr_2X$ based alloys were easily cast and showed no evidence of cracking. After heat treatment, the large 400-500 g alloy ingots were clad inside Mo billets and hot extruded at 1480°C and an extrusion ratio of 4:1. The hot-extruded material was then heat treated and used for tensile specimens. The small 40 g castings were used as-cast to provide specimens for oxidation exposures.

MICROSTRUCTURAL ANALYSIS

Figure 1 shows optical and scanning electron micrographs of hot-extruded CN129, which is a near-optimized $Cr-Cr_2Zr$ based alloy containing four alloying additions (see Table 1). The microstructure consists of patches of the Cr solid solution phase surrounded by interconnected Cr_2Zr Laves phase. It is important to note that, unlike the $Cr-Cr_2Nb$ system[1], no precipitation of Cr_2Zr particles was found in the primary Cr-rich patches (by scanning electron microscopy). Wavelength dispersive electron probe microanalysis (pure element standards) of the Cr solid solution and Laves phases in CN129 are shown in Table 1.

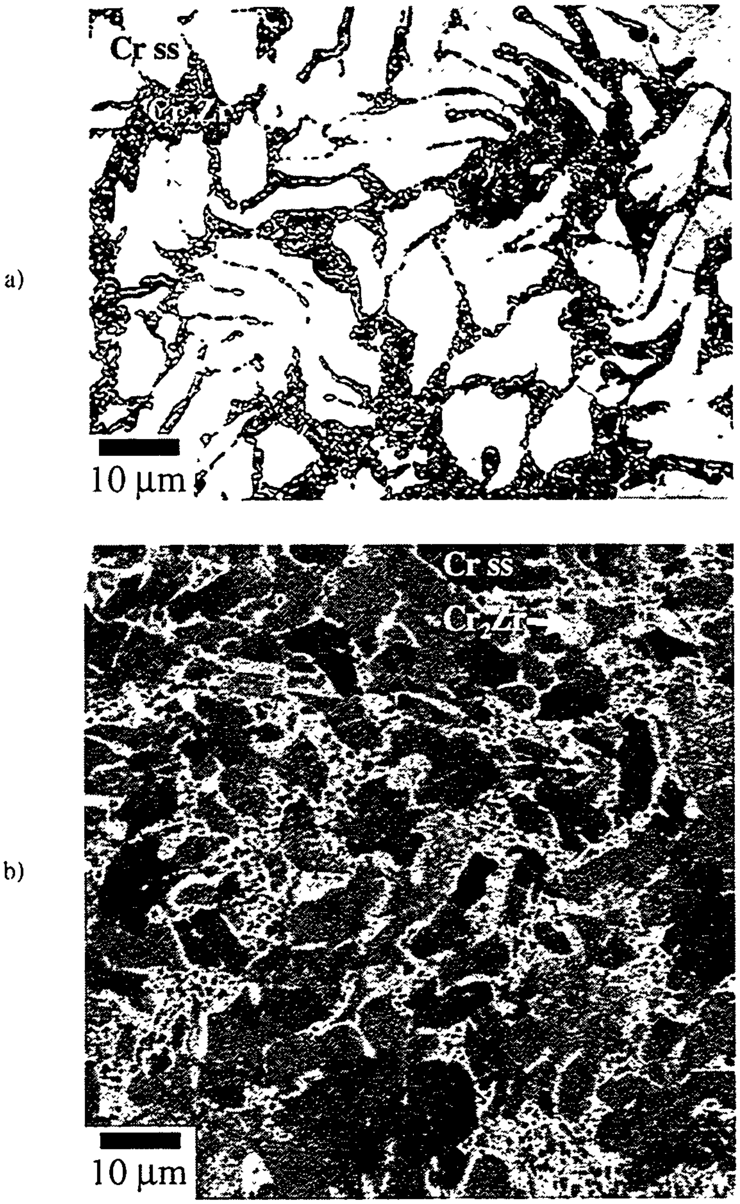

Fig. 1- Microstructure of hot-extruded CN129. a) Optical (light microscopy): Cr solid solution (Cr ss) light, Cr_2Zr Laves dark b) Scanning Electron (secondary): Cr ss dark, Cr_2Zr Laves light.

Table 1- Electron probe microanalysis of hot-extruded CN129 (at.%). An average of 3-6 measurements for each phase is reported. The data is estimated to be accurate within ± 1-2 at.%.

CN129	Cr	Zr	X1	X2	X3	X5
Cr solid solution	93.04	0.02	4.99	0.53	1.27	0.16
Laves	49.12	26.08	6.37	11.19	3.30	3.94
Nominal	84	5	5	3	2	1

Figure 2 shows optical and scanning electron micrographs of hot-extruded CN130, which was one of the first Cr-Cr_2X based alloys to be studied. The microstructure consists of a fine dispersion of spherodized Cr_2X Laves phase particles dispersed in a Cr solid solution matrix. Such a microstructure is expected to be nearly ideal for achieving optimum mechanical properties. Electron microprobe analysis of CN130 is shown in Table 2.

TENSILE PROPERTIES

Button-type tensile specimens with gage dimensions 0.31 cm diam x 0.95 cm long were machined by electro-discharge machining from hot-extruded material, followed by grinding and polishing with "0" Emery paper. The tensile specimens were tested in an Instron Testing Machine at room temperature, 800°C, and 1000°C in air, and at 1200°C in vacuum (crosshead speed of approximately 0.25 cm/minute).

Table 3 summarizes the tensile properties of two near-optimized Cr-Cr_2Zr based alloys, CN128 and CN129. No macroscopic yielding prior to fracture was observed. However, room-temperature fracture strengths of greater than 80 ksi (550 MPa) were obtained. These fracture strengths are slightly higher than that of the best Cr-Cr_2Nb based alloys[1,2].

The alloy CN129 also showed no macroscopic tensile ductility at 1000°C, but was extremely ductile at 1200°C. This suggests that the ductile to brittle transition temperature (DBTT) of Cr-Cr_2Zr based alloys is around 1100°C. At 1200°C, the alloy is very strong, with an ultimate tensile strength of greater than 58 ksi (400 MPa).

The tensile properties of the first generation of Cr-Cr_2X based alloys are summarized in Table 4. Strengths of over 100 ksi (689 MPa) were obtained at room temperature (no macroscopic yielding prior to fracture was observed). At 800°C, elongation on the order of 1% and fracture strengths in excess of 130 ksi (896 MPa) were obtained. Although not yet optimized, this first generation of Cr-Cr_2X based alloys already exhibits much better lower-temperature tensile behavior than the best Cr-Cr_2Nb and Cr-Cr_2Zr based alloys[1]. The tensile elongation increases with temperature, and reaches around 20% at 1200°C. At 1200°C, one Cr-Cr_2X based alloy exhibited an ultimate tensile strength of greater than 50 ksi (345 MPa), which is in the range of the tensile properties obtained for the Cr-Cr_2Nb and Cr-Cr_2Zr based alloys at 1200°C[1].

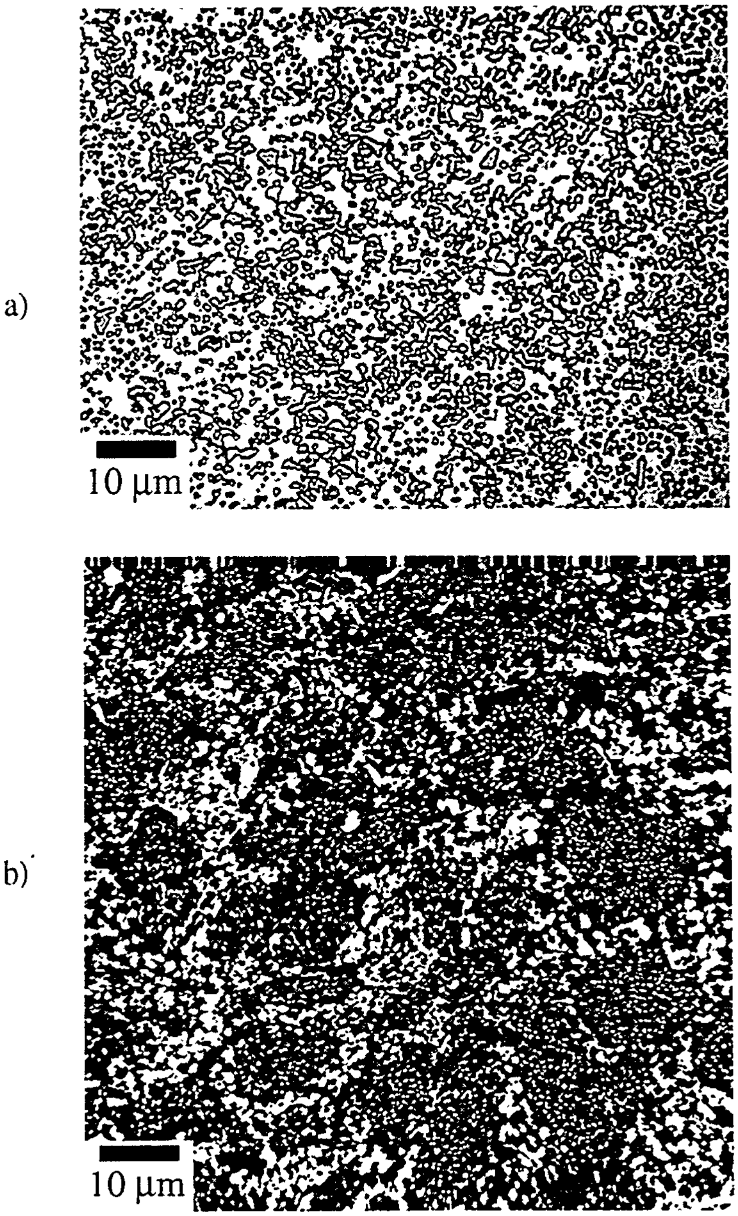

Fig. 2- Microstructure of hot-extruded CN130. a) Optical (light microscopy): Cr ss matrix, Cr_2X Laves second phase b) Scanning Electron (secondary): Cr ss dark, Cr_2X Laves light, Oxide inclusion black.

Table 2- Electron probe microanalysis of hot-extruded CN130 (at.%). An average of 3-6 measurements for each phase is reported. The data is estimated to be accurate within ± 1-2 at.%.

*CN130	Cr	X	X1	X3
Cr solid solution	93.69	0.95	5.33	0.03
Laves	68.01	27.16	4.824	0.003
Nominal	86.5	8	5	0.5

*X3-rich oxide particles and a very minor volume fraction phase of Cr-33X-8.5X1 were also observed.

Table 3- Tensile properties of hot-extruded Cr-Zr base alloys.

Alloy No.	Alloy Composition (at. %)	Yield Strength (ksi)	Fracture Strength (ksi)	Elongation (%)
	Room Temperature			
CN128	Cr-6Zr-5X1-3X2-1X3-1X5	>83.6	83.6	*
CN129	Cr-5Zr-5X1-3X2-2X3-1X5	>81.5	81.5	*
	1000°C			
CN129		>81.3	81.3	*
	1200°C			
CN129		45.1	58.6	>63+

* Fracture prior to macroscopic yielding

+ The test was stopped after straining to 63%

While it is unlikely that CN alloys will ever be able to exhibit appreciable room-temperature tensile ductility, significant room-temperature fracture toughness may be possible because of the two-phase microstructure. Quantitative measurements of room temperature fracture toughness of the $Cr-Cr_2X$ based alloys have not yet been made. However, qualitative assessment of room-temperature toughness by simple "drop" and "hammer-impact" tests suggest that the $Cr-Cr_2X$ based alloys possess superior toughness to the $Cr-Cr_2Nb$ and $Cr-Cr_2Zr$ based alloys. The best $Cr-Cr_2Nb$ and $Cr-Cr_2Zr$ based alloys to date exhibit room-temperature fracture toughness on the order of 7-8 $MPa\sqrt{m}$. The $Cr-Cr_2X$ based alloys are therefore expected to have fracture toughness greater than this range.

OXIDATION BEHAVIOR

All CN alloys will require an oxidation-resistant coating at temperatures above approximately 1000°C because of chromia (Cr_2O_3) scale volatility[10]. Previous and ongoing work at The Ohio State University has demonstrated that silicide coatings applied by a pack cementation process can substantially improve the isothermal and cyclic oxidation resistance of CN alloys at temperatures above 1000°C in air[11-13]. However, in application, the CN alloys must demonstrate a degree of oxidation resistance at these high temperatures to provide for survivability in the event of coating failure. Therefore, a screening test that consisted of 1100°C exposures in room air was adopted to evaluate the high-temperature oxidation resistance of the newly developed CN alloys.

Table 4- Tensile properties of hot-extruded Cr-8X based alloys.

Alloy No.	Alloy Composition (at. %)	Yield Strength (ksi)	Fracture Strength (ksi)	Elongation (%)
	Room Temperature			
CN130	Cr-8X-5.0X1-0.5X3	>104	104	*
CN132	Cr-8X-5.0X1-3.0X2-0.5X3-0.05X6	>71	71	*
CN133	Cr-8X-2.5X1-3.0X2-0.5X3	>101	101	*
	800°C			
CN130		120	120	0.8
CN132		134	137	1.2
CN133		>69	69	*
	1000°C			
CN130		86	97	7.6
CN132		97	104	3.0
CN133		81	89	8.6
	1200°C			
CN130		37	45	16.6
CN132		42	51	18.5
CN133		30	36	22.0

*Fracture prior to macroscopic yielding.

Disk shaped oxidation specimens of 8-13 mm in diameter and 1 mm thickness were sectioned from as-cast or hot-extruded material and polished to a 600 grit finish using SiC paper. The oxidation specimens were placed in an alumina crucible and covered with an alumina lid. At intervals of 1, 4, 10, 30, 48, and 120 hours, the samples were removed from the furnace at temperature, air-cooled, weighed, and returned to the furnace at temperature. Using this interrupted weight change procedure, both isothermal and cyclic oxidation resistance may be surveyed. Volatilization of chromia occurred during the test, as evidenced by a green stain on the inside surfaces of the alumina crucible and lid.

The interrupted weight change oxidation data for Cr-10X, Cr-10Nb, and pure Cr are shown in Figure 3. Comparison data for the Cr-Cr_2Zr based alloy CN129 are also provided. Cr-10X exhibited excellent oxidation resistance for a chromia-former at this high-temperature and was the only one to survive the interrupted weight change screening intact. After 6 cycles and 120 h of exposure at 1100°C, a uniform scale with only very slight evidence of spallation at the sample edges was observed. In contrast, Cr-10Nb and pure Cr suffered from extensive scale spallation. CN129 catastrophically failed between the 10 and 30h cyclic intervals. Preliminary cross-section analysis of isothermally oxidized CN129 indicates that Zr in the

Cr_2Zr Laves phase is extensively internally oxidized. This may have led to catastrophic failure during the interrupted weight change exposure as a result of coefficient of thermal expansion mismatch between the internal zirconium oxide and the surrounding metal.

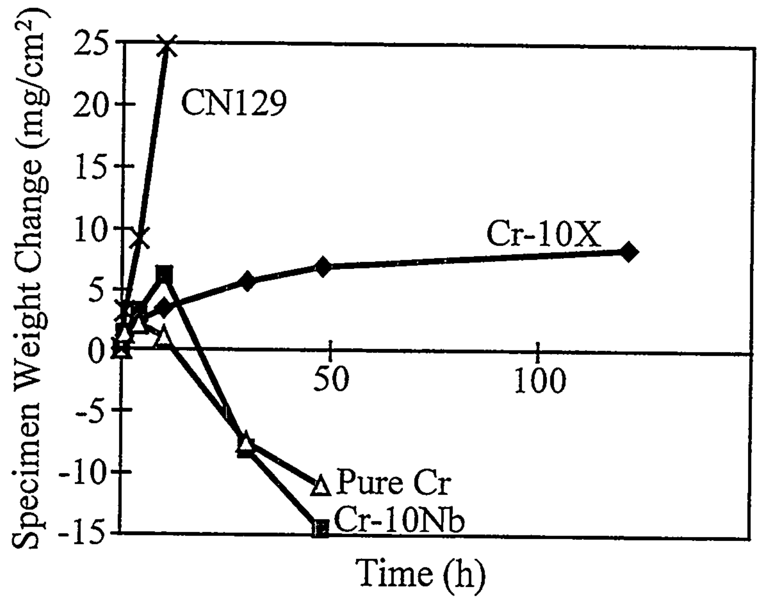

Fig. 3- Interrupted weight change data for as-cast Cr-10X, Cr-10Nb, and pure Cr at 1100°C in room air (at.%). Data for hot-extruded CN129 (Cr-5Zr-5X1-3X2-2X3-1X5 at.%) are also shown.

Cross-section scanning electron micrographs of Cr-10X, Cr-10Nb, and pure Cr after 6 cycles and 120 hours of exposure at 1100°C are shown in Figure 4. A continuous chromia scale formed on Cr-10X. Microhardness measurements in the metal beneath the metal/scale interface showed no evidence of interstitial O or N penetration (note that this technique is only sensitive to within about 5-10 microns of the metal/scale interface). The scale that formed on Cr-10Nb consisted primarily of a complex mixture of chromium and/or chromium plus niobium oxides. X-ray diffraction data from 1200°C exposed Cr-10Nb suggests the presence of Cr_2O_3 and $CrNbO_4$, in agreement with prior observation on Cr-Cr_2Nb alloys oxidized at 950°C[14]. No scale remained on pure Cr. Microhardness measurements in both Cr-10Nb and pure Cr indicate significant hardening and embrittlement in the metal beneath the metal/scale interface.

Figures 5 and 6 show 1100°C interrupted weight change data for alloying additions of X1 or X2 to a Cr-8X based alloy. Cr-8X was less oxidation resistant than Cr-10X due to a tendency to spall, but was preferred from a mechanical property standpoint. Additions of X1 to Cr-8X resulted in comparable oxidation resistance to Cr-10X (Figure 5). However, additions of X2 were deleterious to the oxidation resistance of Cr-8X (Figure 6). These results are surprising because the reverse effect had been observed for additions of X1 and X2 to Cr-Cr_2Nb based alloys[15], although that data was obtained isothermally at lower temperatures. The reasons for these differences are under investigation.

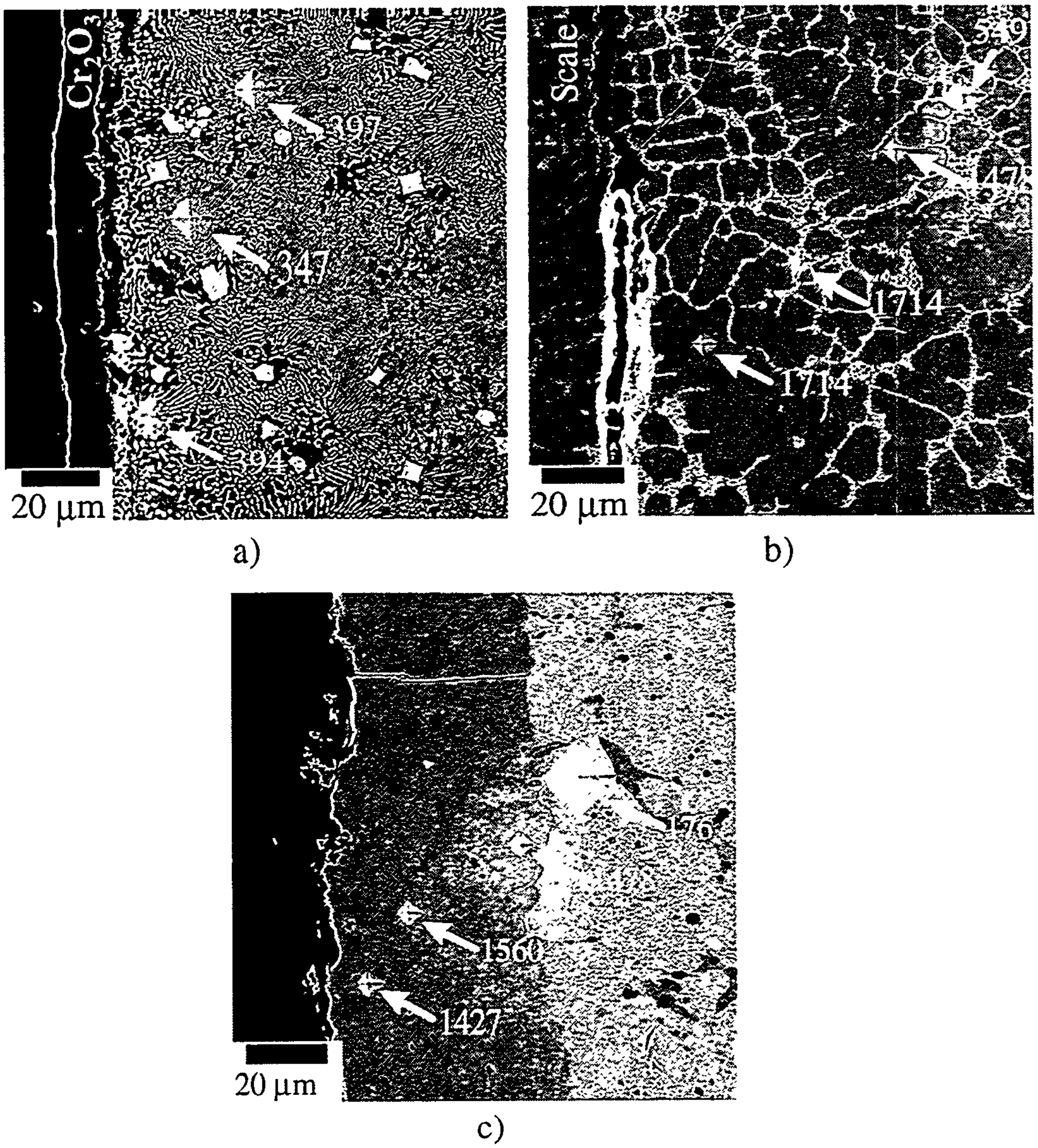

Fig. 4- Cross-section scanning electron (secondary) micrographs of as-cast (a) Cr-10X (≅ 15µm thick scale), (b) Cr-10Nb (≅ 550 µm thick scale), and (c) pure Cr (complete scale spallation) after 6 cycles and 120 h at 1100°C in room air. The Vicker's hardness indentation was performed at a load of 100 g for 15 seconds.

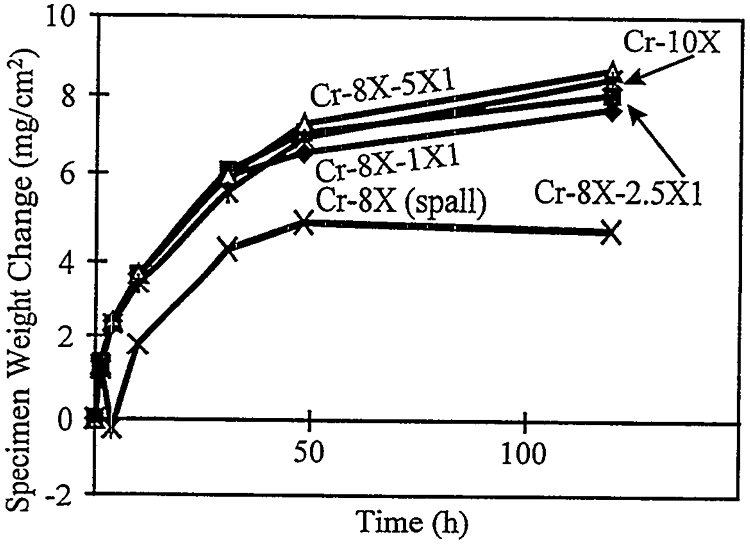

Fig. 5- Interrupted weight change data for as-cast Cr-8X-1X1, Cr-8X-2.5X1, Cr-8X-5X1, Cr-8X, and Cr-10X at 1100°C in room air (at.%).

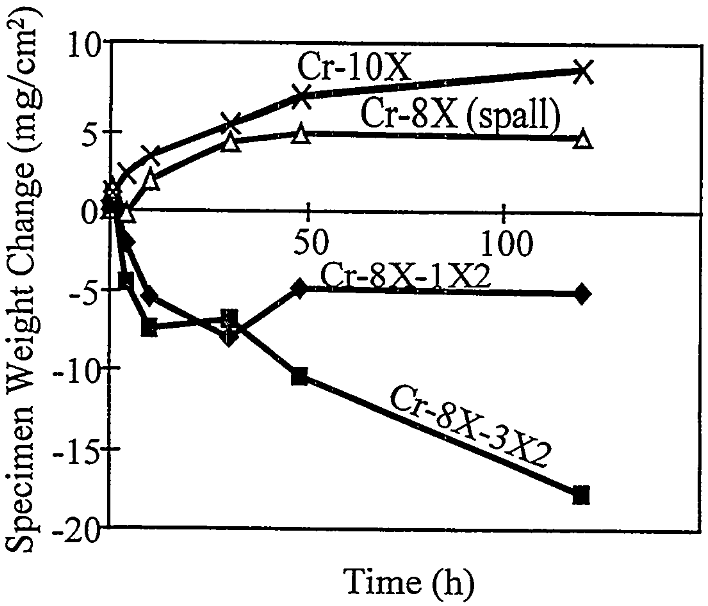

Fig. 6- Interrupted weight change data for as-cast Cr-8X-1X2, Cr-8X-3X2, Cr-8X, and Cr-10X at 1100°C in room air (at.%).

SUMMARY AND FUTURE WORK

A new family of Cr-Cr_2X based alloys has been identified, whose fabricability, mechanical properties, and oxidation resistance are dramatically better than that of previously developed Cr-Cr_2Nb and Cr-Cr_2Zr based alloys. Future work will concentrate on a more complete evaluation of mechanical properties, including room temperature fracture toughness, and compositional modification for optimum mechanical properties and oxidation resistance.

ACKNOWLEDGMENTS

The authors thank Dewey Easton for the hot extrusions, and Bruce Pint, Joachim Schneibel, and Jim Distefano for their reviews of the manuscript. This research was sponsored by the Fossil Energy Advanced Research and Technology Development (AR&TD) Materials Program, U S. Department of Energy, under contract DE-AC05-96OR22464 with Lockheed Martin Energy Research Corporation.

REFERENCES

1. C. T. Liu, P. F. Tortorelli, J. A. Horton, D. S. Easton, and L. Heatherly, pp. 477-89 in *Proc. Tenth Annual Conf. Fossil Energy Materials*, N. C. Cole and R. R. Judkins (comp.), U. S. Department of Energy, August 1996.
2. C. T. Liu, P. F. Tortorelli, J. A. Horton, D. S. Easton, J. H. Schneibel, L. Heatherly, C. A Carmichael, M. Howell, and J. L. Wright, pp. 415 - 26 in *Proc. Ninth Annual Conf. Fossil Energy Materials*, N. C. Cole and R. R. Judkins (comp.), U. S. Department of Energy, August 1995.
3. C. T. Liu, J. A. Horton, and C. A. Carmichael, pp. 377-390 in *Proc. 8th Annual Conf. on Fossil Energy Materials*, N. C. Cole and R. R. Judkins (comp.), U. S. Department of Energy, August 1994.
4. C. T. Liu, J. A. Horton, and C. A. Carmichael, pp. 297-307, in *Proc. 7th Annual Conf. on Fossil Energy Materials*, N. C. Cole and R. R. Judkins (comp.), U. S. Department of Energy, July 1993.
5. C. T. Liu, pp. 375-383 in *Proc. 6th Annual Conf. Fossil Energy Materials*, N. C. Cole and R. R. Judkins (comp.), U. S. Department of Energy, July 1992.
6. F. Laves, p. 124 in Theory of Alloy Phases, American Society for Metals, Metals Park, OH, 1956.
7. D. J. Thoma and J. H. Perepezko, Mat. Sci. and Eng. A156 (1992) 97.
8. H. J. Goldschmidt and J. A. Brand, J. Less-Common Met. 3 (1961) 44.
9. T. B. Massalski, J. L. Murray, L. H. Bennett, and H. Baker (eds.), Binary Alloy Phase Diagram, American Society for Metals, Metals Park, OH, 1986.
10. P. Kofstad, High-temperature Corrosion, Elsevier, London, 1988.
11. Y-R. He, M. Zheng, and R.A. Rapp, 465-476, in *Proc. Tenth Annual Conf. Fossil Energy Materials*, N. C. Cole and R. R. Judkins (comp.), U. S. Department of Energy, August 1996.
12. Y-R. He, R. A. Rapp, and P. F. Tortorelli, "Oxidation-Resistant Ge-Doped Silicide Coating on Cr-Cr_2Nb Alloys by Pack Cementation," pp. 109-117, *Mater. Sci. and Eng. A*, A222, 1997.
13. Y-R. He and R. A. Rapp, these proceedings.
14. P.F. Tortorelli and B.A.. Pint, pp.174-185 in Fundamental Aspects of High-Temperature Corrosion, D.A.. Shores, R.A.. Rapp, and P.Y. Hou (eds.), Proceedings Volume 96-26, The Electrochemical Society, Pennington, New Jersey, 1997.
15. P.F. Tortorelli and J.H. DeVan, pp.391 - 400 in *Proc. Eighth Annual Conf. Fossil Energy Materials*, N.C. Cole and R.R. Judkins (comp.), CONF-9405143, U. S. Department of Energy, August 1994.

STUDY OF FATIGUE AND FRACTURE BEHAVIOR OF $NbCr_2$-BASED ALLOYS: PHASE STABILITY IN Nb-Cr-Ni TERNARY SYSTEM

J. H. Zhu*, P. K. Liaw*, and C. T. Liu+

*Department of Materials Science and Engineering
The University of Tennessee, Knoxville, TN 37996

+Metals and Ceramics Division, Oak Ridge National laboratory
Oak Ridge, TN 37831-6115

ABSTRACT

Phase stability in a ternary Nb-Cr-Ni Laves phase system was studied in this paper. Our previous study in $NbCr_2$-based transition-metal Laves phases has shown that the average electron concentration factor, e/a, is the dominating factor in controlling the phase stability of $NbCr_2$-based Laves phases when the atomic size ratios are kept identical. Since Ni has ten out-shell electrons, the substitution of Ni for Cr in $NbCr_2$ will increase the average electron concentration of the alloy, thus leading to the change of the crystal structures from C15 to C14. In this paper, a number of pseudo-binary $Nb(Cr,Ni)_2$ alloys were prepared, and the crystal structures of the alloys after a long heat-treatment at 1000°C as a function of the Ni content were determined by the X-ray diffraction technique. The boundaries of the C15/C14 transition were determined and compared to our previous predictions. It was found that the electron concentration and phase stability correlation is obeyed in the Nb-Cr-Ni system. However, the e/a ratio corresponding to the C15/C14 phase transition was found to move to a higher value than the predicted one. The changes in the lattice constant, Vickers hardness and fracture toughness were also determined as a function of the Ni content, which were discussed in light of the phase stability difference of the alloys.

INTRODUCTION

Laves phases with AB_2 composition comprise the single largest class of intermetallics, yet they are the least studied, compared with the conventional intermetallics, such as B2, $L1_2$, etc. Transition-metal Laves phases are currently being considered for many practical applications, e.g., $(Hf,Zr)V_2$ as superconducting material, $Zr(Cr,Fe)_2$ as hydrogen storage material, etc.[1,2] More recently, HfV_2-, $HfCr_2$- and $NbCr_2$-based two-phase alloys[3-9] are being developed for high-temperature structural uses, because of their good retention of mechanical properties at elevated temperatures. However, their low ductility and brittle fracture characteristics at ambient temperatures are the main concerns for structural applications of these materials.

Laves phases generally crystallize into one of the three topologically close-packed structures: cubic C15 – $MgCu_2$ structure, hexagonal C14 – $MgZn_2$ structure, and dihexagonal C36 – $MgNi_2$ structure.[10] Although Laves phases are generally stabilized by the size-factor principles, the stability of each crystalline structure is also influenced by the electron concentration factor (e/a). The classic work by Laves and Witte[11,12] showed that for several quasi-binary alloy systems involving $MgCu_2$ and $MgZn_2$, with increasing valence electron concentration, the three Laves types, $MgCu_2$, $MgNi_2$, and $MgZn_2$, exist in that order. One attractive way to improve the deformability of complex Laves phases is to control their crystalline structure in a way that stress-assisted phase transformation and/or mechanical twinning can be triggered during plastic deformation.[13,14] It is thus important to know the factors governing the phase stability in transition-metal Laves alloys.

In our previous investigation[15], a number of binary and ternary phase diagrams were surveyed, and the phase stability criteria in the $NbCr_2$-based Laves phase systems, binary X-Cr and Nb-X and ternary Nb-Cr-X, were studied. It was shown that when the atomic size ratios are kept identical, the average electron concentration factor, e/a, is the dominating factor in controlling the phase stability of $NbCr_2$-based transition-metal Laves phases. The e/a ratios for different Laves polytypes were determined as follows: with $e/a < 5.76$, the C15 structure is stabilized; at an e/a range of 5.88-7.53, the C14 structure is stabilized; with $e/a > 7.65$, the C15 structure is stabilized again. A further increase in the electron concentration factor ($e/a > 8$) leads to the disordering of the alloy. The results are summarized in Fig. 1.

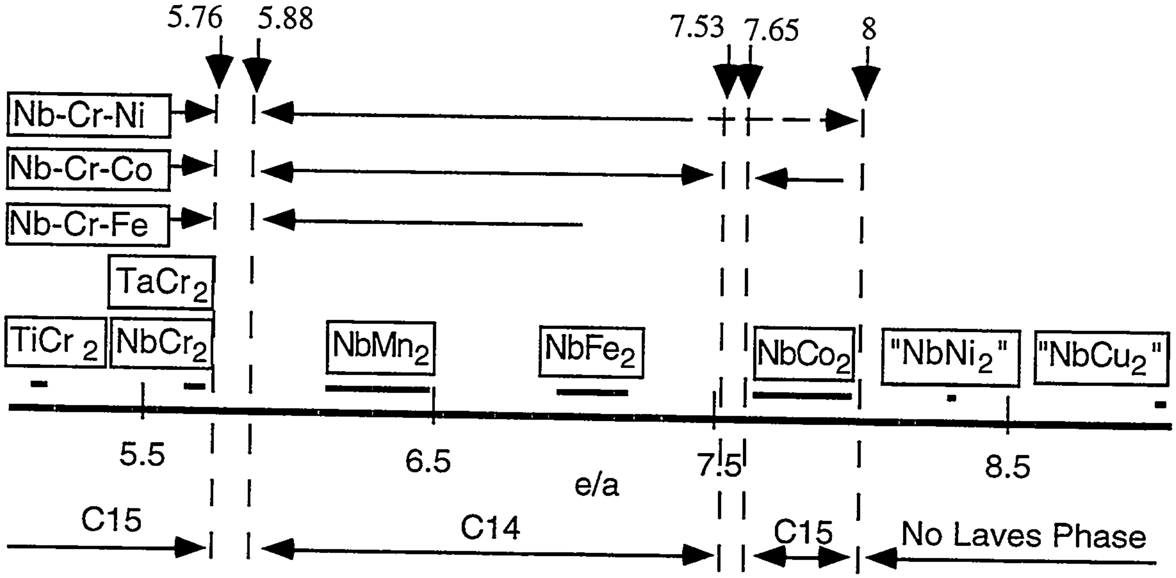

Fig. 1 Effect of average electron concentration (e/a) on phase stability in binary and ternary $NbCr_2$-based systems[15]

In this investigation, the Laves-phase stability in the ternary Nb-Cr-Ni system was studied experimentally to verify the observed e/a/phase stability correlation. Since Ni has ten outshell electrons, the addition of Ni to substitute for Cr ($e/a = 6$) in $NbCr_2$ is very effective in increasing the average electron concentration. By a systematic replacement of Cr with Ni, it is possible to see a whole spectrum (e.g., C15→ C14→C15) of changes in the crystal structure of the Laves-phase based $Nb(Cr,Ni)_2$ alloys. The results reported here include the phase structures, lattice constants, hardness, and fracture toughness of the Laves phases as a function of the Ni content.

EXPERIMENTAL PROCEDURES

A series of pseudo-binary $Nb(Cr,Ni)_2$ alloys with 0, 1, 3, 5, 10, 20, 35 at % Ni were produced by replacing Cr with Ni, while keeping the percentage of Nb constant (33.3 at.%). Table 1 lists the nominal chemical compositions (at.%) and the average electron concentrations (e/a) and the predicted crystal structures (using the data shown in Fig. 1) of the alloys studied in this work. These alloys are in the C15 region, the C15/C14 transition region, and the C14 region, respectively, according to the prediction of Fig.1.

Table 1 The chemical compositions, e/a ratios, and predicted structures of pseudo-binary $Nb(Cr,Ni)_2$ alloys

Alloy No.	1	2	3	4	5	6	7
Ni Content	0	1	3	5	10	20	35
e/a Ratio	5.67	5.71	5.79	5.87	6.07	6.47	7.07
Structure	C15	C15	C15/C14	C15/C14	C14	C14	C14

All the alloys of about 50 grams were prepared by arc-melting techniques using starting materials of 99.8% Nb, 99.99% Cr, and 99.95% Ni. An excess amount (typically 1%) of Cr was added to compensate for the evaporation loss of Cr during melting. Arc-melting was carried out in a chamber which was evacuated by a mechanical pump and flushed with ultra-high purity (UHP) argon gas four or five times, and finally backfilled with UHP argon gas. A Zr sample was melted prior to melting the alloy charge each time in order to getter the oxygen in the chamber. The arc-melting was done using a thoriated tungsten electrode on a water-cooled copper hearth. Each ingot was inverted and remelted at least 7 times to ensure macroscopic compositional homogeneity. The alloys were homogeneized in vacuum at 1300°C for 90 hours, then slowly cooled in the furnace, except two alloys with 20 and 35 at% Ni, which were homogenized at 1100°C for 120 hours. Finally, all the alloys were heat treated at 1000°C for 1000 hours, then water quenched to retain the equilibrium condition at 1000°C.

X-ray diffraction measurements were made using a Scintag XD2000 diffractometer with the Cu K_a (λ = 0.15406 nm) radiation. Powdered samples were used, and the lattice parameter determination was furnished by using a Si standard for internal calibration. The microhardness was measured using a load of 500 g with a holding time of 15 seconds. For fracture toughness determination, a load of 200 g was used for indentation, and the crack lengths were measured immediately after the indentation to eliminate the possibility of slow crack propagation after removal of the indentor. The following equation was used to calculate the fracture toughness of the alloy[16,17]:

$$K_{IC} = A\left(\frac{E}{H}\right)^n \frac{P}{L^{3/2}} \tag{1}$$

where K_{IC} = fracture toughness ($\mathrm{MPa}\sqrt{\mathrm{m}}$), E = Young's modulus (GPa), H = Vickers hardness (GPa), P = load (N), and L = average length of the 4 radial cracks from the center of the indent to the crack tip. A and n are constants, which are taken here as 0.016 and 0.5 respectively.

RESULTS AND DISCUSSIONS

X-ray diffraction results show that the Laves phase after the addition of up to 5 at.% Ni maintains its original C15 structure, while the C14 structure is stabilized for alloys with 10, 20, and 35 at% Ni. Thus, the C15-->C14 phase transition is observed for the ternary system. Figure 2 shows the diffraction patterns for alloys with 5 and 10 at.% Ni, which were indexed as C15 and C14, respectively. However, the phase boundaries of the C15/C14 transition seem to move to higher electron concentration values, compared to the results predicted from Fig. 1. As an example, according to Fig. 1 and Table 1, the alloy with 5 at.% Ni

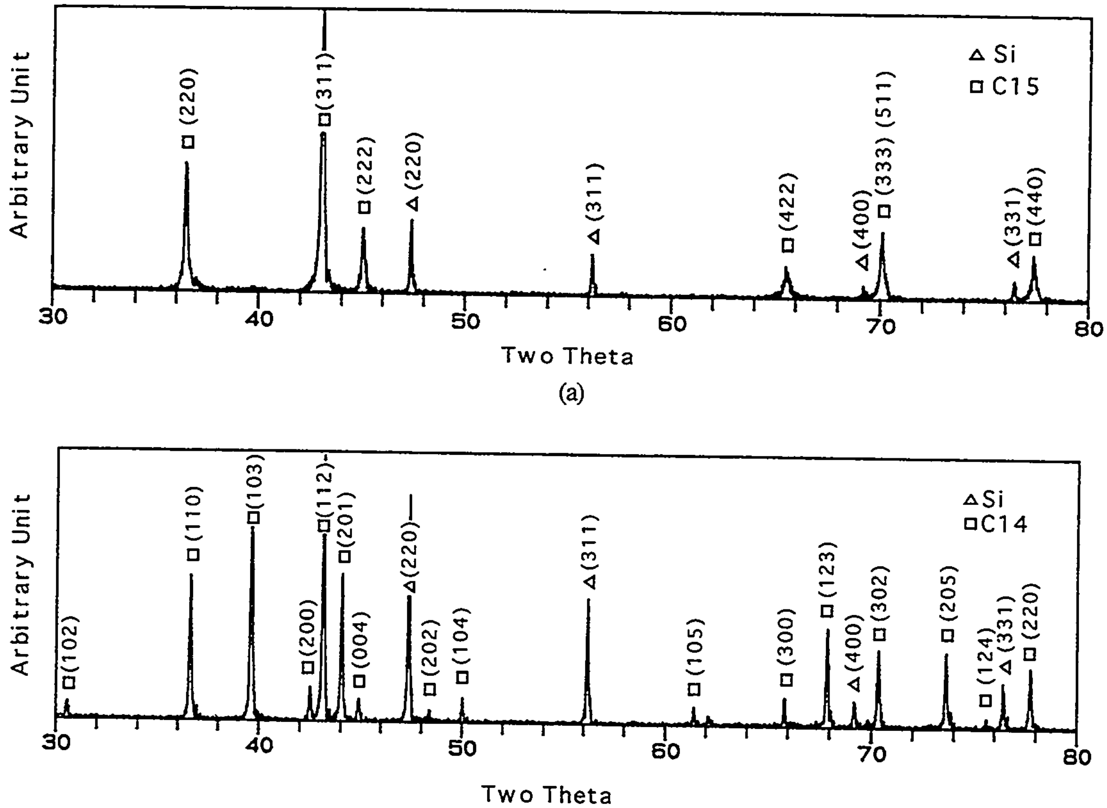

(a)

(b)

Fig. 2 X-ray diffraction patterns of $Nb(Cr, Ni)_2$ alloys with (a) 5 at.% Ni and (b) 10 at.% Ni, which were indexed as C15 and C14, respectively alloy should be in the transition region, i.e., either C14 and C15 two phases coexist or some intermediate structures other than C14 and C15 will be stabilized. It is still in the C15 region from the experimental data (see Fig. 2(a)). It is thus clear that the maximum electron concentration for stabilizing the C15 structure will be greater than 5.87. More alloys with the Ni contents between 5 and 10 at.% are being prepared, and the precise phase boundaries will be determined.

The crystal lattice parameters of the C15 and C14 Laves phases were measured for the pseudo-binary $Nb(Cr,Ni)_2$ alloys with various Ni contents. Figure 3 shows the graph for the dependence of the lattice constant a of the cubic C15 $Nb(Cr,Ni)_2$ alloy on the nickel content. As the Ni content increases, the lattice constant decreases linearly. Figure 4 illustrates the dependence of the lattice parameters a and c of the hexagonal C14 $Nb(Cr,Ni)_2$ alloy on the nickel content. As the Ni content increases, both a and c decrease linearly. Extrapolation of these dependence to 0 per cent Ni, i.e. to pure $NbCr_2$ gives us the lattice parameters of the high-temperature modification (C14) of the compound $NbCr_2$ (a = 4.9322 Å, c = 8.1312 Å), which were also plotted in 4. The dependence of the c/a ratio of the hexagonal C14 $Nb(Cr,Ni)_2$ alloy on nickel content is plotted in Fig. 5. As the Ni content increases, the c/a decreases linearly. It will be interesting to prepare some pseudo-binary $Nb(Cr,Ni)_2$ alloys with higher Ni contents and study the crystal structure and the lattice parameter of the alloys, since some work has indicated that the solubility of Ni in NbCr2 is less than 40 at. %. According to our prediction of the e/a correlation with phase stability, the Ni can substitute a higher percentage of Cr from the electron concentration point of view. Our work in the ternary Nb-Cr-Cu system has demonstrated that in addition to the e/a criterion, the electronegativity may also be an important factor in limiting the solubility of the solute atom in $NbCr_2$ compound.[15]

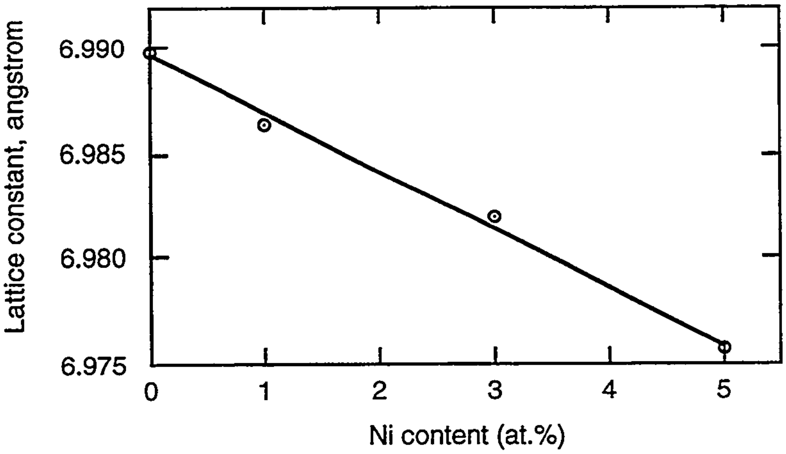

Fig. 3 Dependence of lattice constant, a, of cubic C15 phase on the nickel content

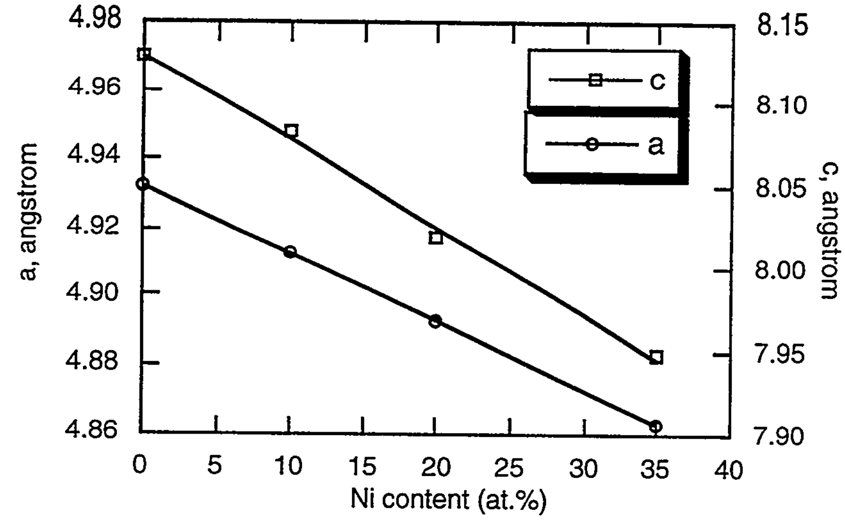

Fig. 4 Dependence of lattice parameters, a and c, of hexagonal C14 on the nickel content

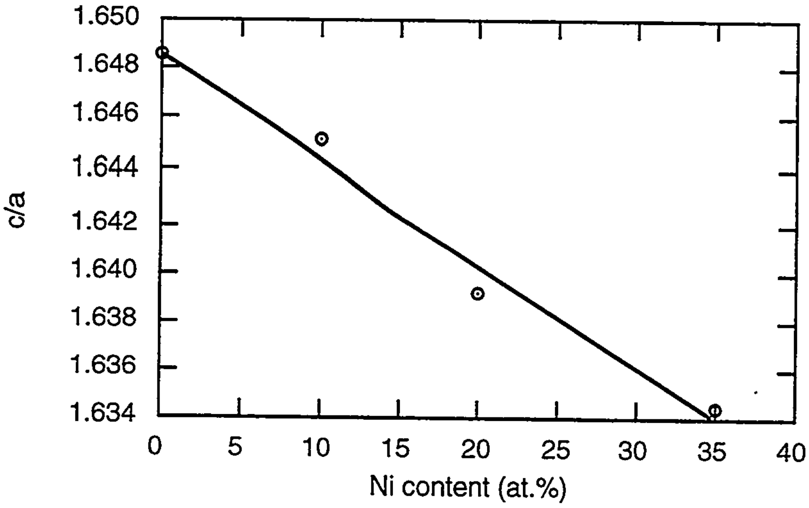

Fig. 5 Dependence of c/a of hexagonal C14 phase on the nickel content

The Vickers hardness of the pseudo-binary $Nb(Cr,Ni)_2$ alloys with various Ni contents is plotted in Fig. 6. It is clear from this figure that the addition of the nickel to substitute for Cr increases the hardness of the Laves phase. Also, the trend is that the Ni increases the hardness of the C15 structure more significantly than that of the C14 structure. The decreased lattice constants by the addition of Ni signifies the close-up of the close-packed lattice structure and an increase in the interatomic bonding. This can be used to explain the hardness increases as the Ni content in the alloy increases.

Figure 7 shows the cracking situation in the area near the indentation for a $Nb(Cr.Ni)_2$ alloy with 10 at% Ni, from which we can measure the average crack length, L. The fracture toughness calculated using Eq. (1) as a function of Ni content is shown in Fig. 8. Basically, the fracture toughness of the monolithic Laves phase is very low, about 1 MPa$\sqrt{m}$, which is a consequence of the topologically close packing manner of the structure and the subsequent difficulty in activating dislocation sources in the material. No general trend regarding the effect of the Ni content on the fracture toughness of the Laves alloys can be deduced from this curve. The toughness value near the phase boundary may increase, due to the fact that the associated structure is metastable, and it is easy to transform from one structure to another during deformation. Unfortunately, none of the alloys used in this investigation falls in the transition region. More alloys in the transition region is being prepared, and the fracture toughness of these alloys will be determined.

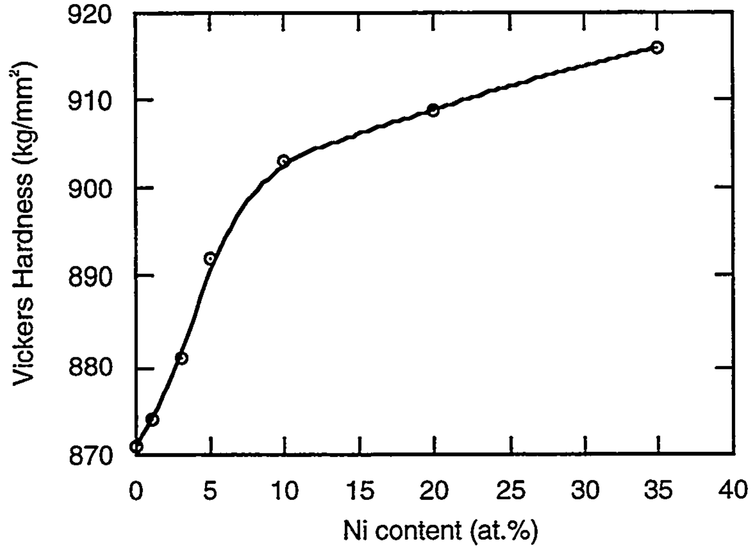

Fig. 6 The effect of Ni content on the Vickers hardness of $NbCr_2$ alloys

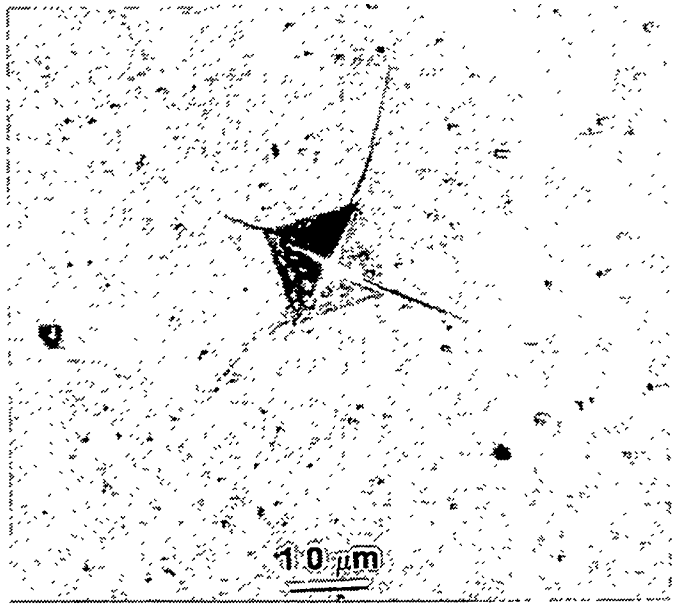

Fig. 7 Cracking phenomenon near the indented region for the alloy with 10 at.% Ni

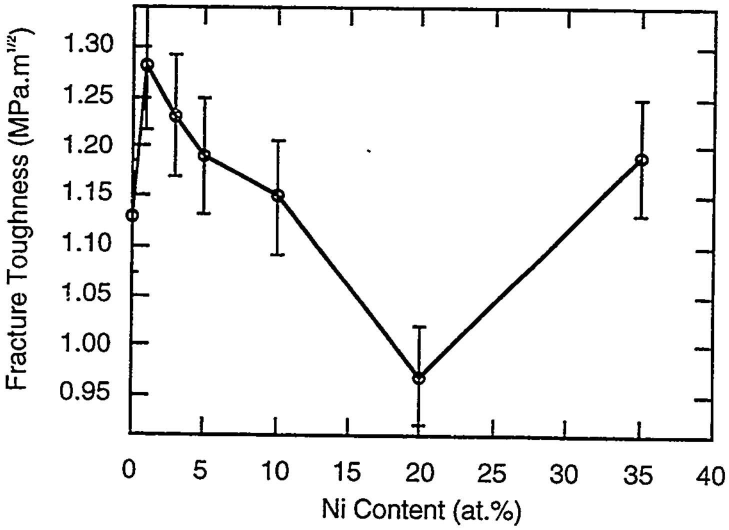

Fig. 8 Fracture toughness values of the laves phases as a function of the Ni content

CONCLUSIONS

It has been shown that the average electron concentration factor, e/a, is the dominating factor in controlling the phase stability of the ternary Nb-Cr-Ni Laves phase system. The substitution of Ni for Cr in $NbCr_2$ increases the average electron concentration of the alloy, thus leading to the change of the crystal structures from C15 to C14. X-ray diffraction results show that for the alloys with ≤ 5 at.% Ni, the C15 structure is stabilized and for the alloys with ≥ 10 at.% Ni the C14 structure is stabilized. From this result, it is clear that the e/a ratio corresponding to the C15/C14 phase transition must be at a value higher than the one previously predicted. The changes in the lattice constant, Vickers hardness, and fracture toughness were also determined as a function of the Ni content. As the Ni content increases, the lattice constants decrease for both C15 and C14 structures, while the Vickers hardness increases over the whole range of the Ni concentration investigated. The fracture toughness is low for all the alloys, and no general trend regarding the fracture toughness can be detected as the Ni content increases. Further investigation will concentrate on alloy compositions containing 5-10 at.% Ni. The phase boundaries of C15/C14 structures will be precisely determined, and the fracture toughness of the alloys near phase boundaries will be studied to see if mechanical twinning and/or stress assisted phase transformation can be triggered, and toughness can be increased for such alloys.

ACKNOWLEDGMENTS

We would like to thank Nancy Cole, Rod Judkins and Paul Carlson of the Oak Ridge National Laboratory for programmatic support, and Joe Wright, Elmer Lee and Cecil Carmichael for their technical assistance. The research was sponsored by the Fossil Energy AR & TD Materials Program, U.S. Department of Energy, under subcontract 11X-SP173V to the University of Tennessee with Lockheed Martin Energy Research Corp.

REFERENCES

1. K. Inoue and K. Tachikawa, IEEE Trans. Magnetics, vol. 15, p. 635, 1979.
2. D. Ivey and D. Northwood, J. of Less- Common Met., vol. 115, p. 23, 1986.
3. F. Chu and D.P. Pope: in High-Temperature Ordered Intermetallic Alloys V, MRS. Symp. Proc. 288, p. 561, 1993.
4. K. S. Kumar and D.B. Miracle, Intermetallics, vol. 2, p. 257, 1994.
5. M. Takeyama and C.T. Liu, Mater. Sci. & Eng. A, vol. 132, p. 61, 1991.
6. J.A. Cook, P.K. Liaw, and C.T. Liu: in Fatigue and Fracture of Ordered Intermetallics, W. O. Soboyejo, T. S. Srivatsan & R. O. Ritchie, eds., TMS, Warrendale, PA, p. 155, 1995,.
7. J.A. Cook, P.K. Liaw, C.T. Liu, and S.B. Bhaduri: in the Johannes Weertman Symposium, R. J. Arsenault et al., eds., TMS, Warrendale, PA, p. 47, 1996.
8. K.S. Chan and D.L. Davidson, JOM,, p. 62, Sept. 1996.
9. D.J. Thoma and J.H. Perepezko, Mater. Sci. & Eng. A, vol. 156, p. 97, 1992.
10. T.B. Massalski: in Physical Metallurgy Part 1, R. W. Cahn & P. Hassen, eds., North-Holland Physics Publishing, NY, p. 190, 1983.
11. F. Laves & H. Witte, Metallwirschaft, vol. 14, p. 645, 1935.
12. F. Laves & H. Witte, Metallwirschaft, vol. 15, p. 840, 1936.
13. Y. Liu, J.D. Livingston, and S.M. Allen, Metall. Tran. A, vol. 23, p. 3303, 1992.
14. M. Grujicic, S. Tangrila, O.B. Cavin, W.D. Porter, and C.R. Hubbard, Mater. Sci. & Eng. A, vol. 160, p. 37, 1993.
15. J. H. Zhu, P. K. Liaw, and C. T. Liu, "Electron Concentration and Phase Stability in $NbCr_2$-Based Laves Phase Alloys", Final Report, U. S. Dept. of Energy, Fossil Energy AR & TD Materials Program, ORNL/Sub/93-SP173/02, National Technical Information Service, Springfield, VA, May, 1997; submitted to Metall. Trans.
16. M. Sakai and R.C. Bradt, Inter, Mat. Rev., vol. 38, No.2, p. 53, 1993.

17. G.R. Anstis, P. Chantikul, B.R. Lawn, and D.B. Marshall, J. of Amer. Ceramics. Soc., vol. 64, No. 9, p. 533, 1981.

WELD OVERLAY CLADDING WITH IRON ALUMINIDES

G. M. Goodwin

ABSTRACT

We have established a range of compositions for these alloys within which hot cracking resistance is very good, and within which cold cracking can be avoided in many instances by careful control of welding conditions, particularly preheat and postweld heat treatment. For example, crack-free butt welds have been produced for the first time in 12-mm thick wrought Fe_3Al plate. Cold cracking, however, still remains an issue in many cases.

We have developed a commercial source for composite weld filler metals spanning a wide range of achievable aluminum levels, and are pursuing the application of these filler metals in a variety of industrial environments. Welding techniques have been developed for both the gas tungsten arc and gas metal arc processes, and preliminary work has been done to utilize the wire arc process for coating of boiler tubes.

Clad specimens have been prepared for environmental testing in-house, and a number of components have been modified and placed in service in operating kraft recovery boilers.

In collaboration with a commercial producer of spiral weld overlay tubing, we are attempting to utilize the new filler metals for this novel application.

INTRODUCTION

To utilize the excellent properties of alloys based on the Fe_3Al nominal composition, particularly resistance to high temperature oxidation and corrosion, we are continuing to develop welding filler metals, procedures, and parameters aimed at introducing these new alloys into commercial service. Although emphasis is still placed on conventional weld overlay techniques, considerable progress has been made recently toward joining thick section monolithic materials, and applying alternative cladding techniques, including spiral weld cladding and wire arc thermal spraying.

Prior efforts (1-6) have identified the causes of hot cracking in these alloys, and, by compositional modification, essentially eliminated it. Cold cracking, however, remains an issue, although recent efforts have made progress toward minimizing it, primarily by control of composition and welding parameters, especially preheat and postweld heat treatment.

Development of filler metals, processes, and procedures is ongoing concurrent with introduction of the materials into service in a variety of industrial applications.

Filler Metal Development

Using the approach described earlier (6), we have developed and now have available a family of filler metal compositions spanning a range of aluminum content from less than 8 to greater than 26 weight percent (Table I). These composite wires are 0.0625-in (1.6mm) diameter, in spooled form, and can thus be used with automatic wire feeders in a number of welding and cladding processes. The actual deposit composition can be modified as desired by control of dilution, deposition rate, and other welding parameters.

Heat Treatment Effects

It was established earlier (4,5) that weld preheat and postweld heat treatment could be effective at avoiding cold cracking of the weld deposits. Based on extensive testing over the range of filler metal compositions, efforts to reduce preheat below 350°C, or postweld heat treatment below 750°C have consistently been unsuccessful at preventing cracking. We conclude, therefore, that these conditions are required, as a minimum, to reliably avoid cold cracking. Using these parameters, however, we have been able to use

TABLE I. COMPOSITION OF IRON ALUMINIDE ALLOY FILLER METALS

	WEIGHT %	Al	Cr	C	Zr	Mo
Stoody I	Aim, all weld metal	20.0	7.0	0.10	0.25	0.25
	Actual, all weld metal	21.8	7.3	0.06	0.40	NA[c]
	Actual, clad deposit [a]	12.6	6.0	0.08	0.20	0.44
	Actual, clad deposit [b]	15.3	12.7	0.05	0.22	0.40
Stoody II	Aim, all weld metal	20.0	--	0.10	0.25	0.25
	Actual, all weld metal	21.5	--	0.08	0.25	NA
	Actual, clad deposit [a]	12.6	--	0.10	0.12	0.40
Stoody III	Aim, all weld metal	12.0	--	0.10	0.25	0.25
	Actual, all weld metal	12.5	--	0.06	0.40	NA
	Actual, clad deposit [a]	7.6	--	0.07	0.32	0.40
Stoody IV	Aim, All weld metal	26.0	--	0.10	0.25	0.25
	Actual, all weld metal	26.5	--	0.08	0.60	NA
	Actual, clad deposit [a]	14.1	--	0.09	0.32	0.40

[a] Single layer automatic gas metal arc on 1-in. thick type 2 1/4 Cr-1Mo steel

[b] Single layer manual gas tungsten arc on 1/2-in. thick type 310 stainless steel

[c] NA - Not Analyzed

the new filler metals to join monolithic sections of plate material which had previously been considered unweldable. Figure 1 shows a metallographic cross-section of a multipass gas tungsten arc weld in 1/2-in (12.7mm) thick alloy FA-129 plate. To match the aluminum level of the base plate (16 weight %), we chose the 20 weight % weld wire (Stoody II), thus allowing for arc losses and dilution by the base plate. As is seen in figure 1.b, the weld microstructure is free of cracks and porosity, and has a narrow heat affected zone and relatively fine-grained fusion zone.

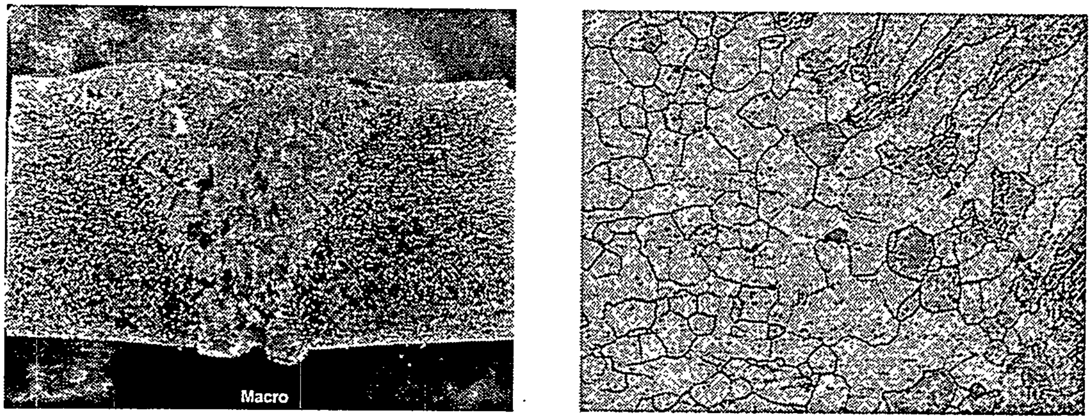

Fig. 1. Multipass Gas Tungsten Arc Weld in 12.7-mm Thick Alloy FA-129 Plate
a) Macrosection, and b) Microstructure; note narrow heat affected zone, fine grained fusion zone, and absence of cracks and porosity.

Industrial Service Testing

Pursuing the tasks started earlier (6), we have prepared several additional components for in-service testing in commercial paper mill recovery boilers, and continue to monitor the condition of parts previously modified by weld overlay. As a basis for comparison, we have also prepared components using high-chromium commercial filler wires, E-Brite 26-1 and Inconel 617 with 26% and 23% chromium, respectively. These alloys would be considered the primary competition for the iron aluminides in high temperature oxidizing/sulfadizing environments.

Wire Arc Cladding*

Wire arc cladding, also known as arc spraying, is being investigated as an alternative to conventional gas tungsten arc or gas metal arc weld cladding. The process is shown schematically in figure 2, from (7). Basically, an arc is struck between two independently fed wires, and compressed gas is used to detach molten droplets from the arc zone and propel them to the substrate. It is a high velocity, high deposition rate process, with droplet temperatures high enough to assure good bond strength. Figure 3.a is an overall view and figure 3.b shows a cross-section of 3-in (76mm) OD carbon steel boiler tube clad with composite filler wire. Spray parameters were 100 amperes DC, 30 volts, and 90 psi air pressure. As seen in figure 3, the coating is heterogeneous,

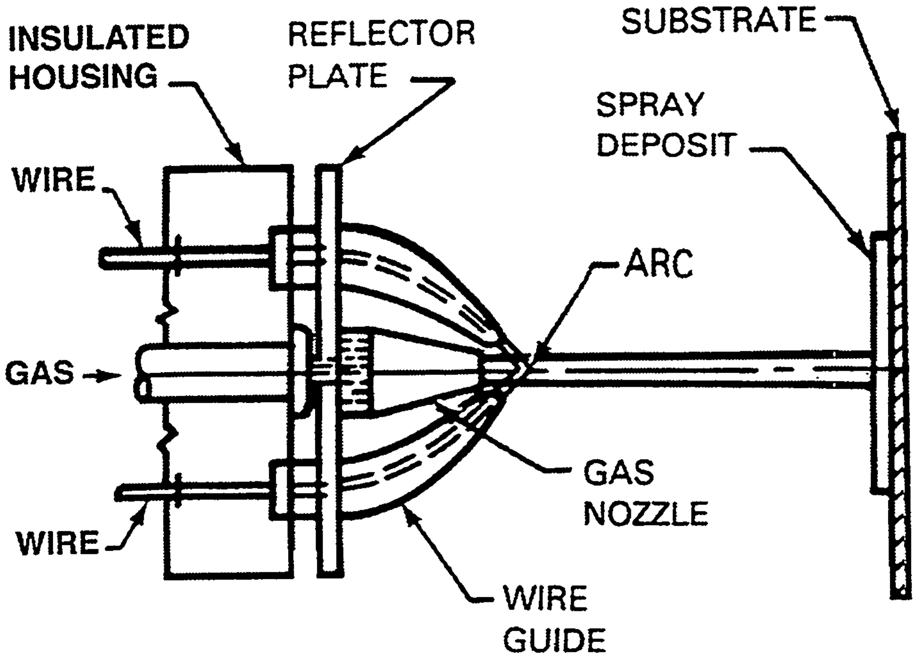

Fig. 2. Wire Arc Spray Process

---

*This task is being performed in collaboration with E. A. Franco-Ferreira of the Engineering Technology Division.

but sound. Thermal cycling of clad specimens to 427°C in air has shown no evidence of spalling after 25 cycles. In order to control the degree of oxidation of the coating, additional specimens are being prepared using nitrogen and argon as carrier gases.

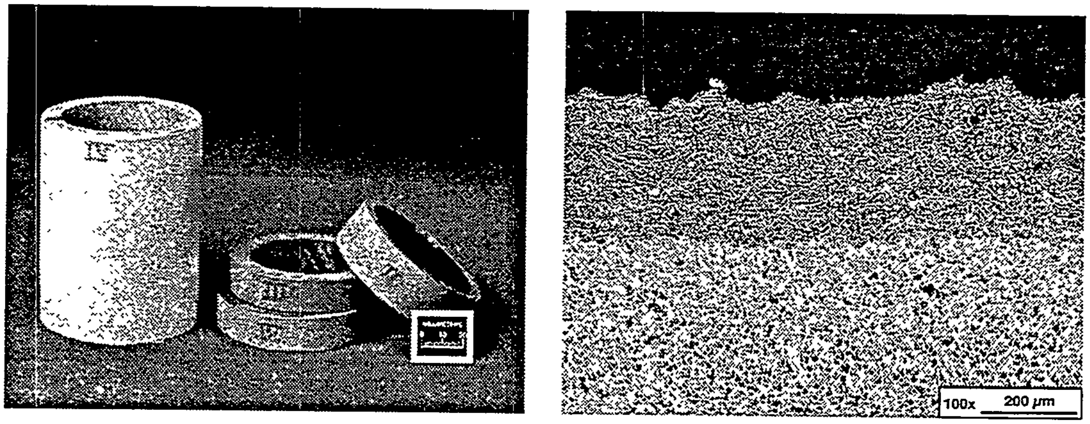

Fig. 3. Boiler Tube Coated by Wire Arc Cladding: a) Overall and b) Microstructure

Spiral Weld Cladding

The spiral weld cladding technique (figure 4 shows an example) uses a combination of gas metal arc and gas tungsten arc welding to overlay boiler tubing prior to fabrication of tube panels. In collaboration with a commercial supplier of spiral welded product, we are using the process to clad carbon steel with the Stoody I composite filler wire composition. If this approach is successful, it will provide a viable alternative to coextruded bimetallic tubing.

CONCLUSIONS

- Hot cracking has essentially been eliminated, but cold cracking still remains an issue in many cases; preheat (350°C minimum) and postweld heat treatment (750°C minimum) are required to reliably avoid it.
- We have developed and have available a family of filler metal compositions from less than 8 to greater than 26 weight % aluminum.

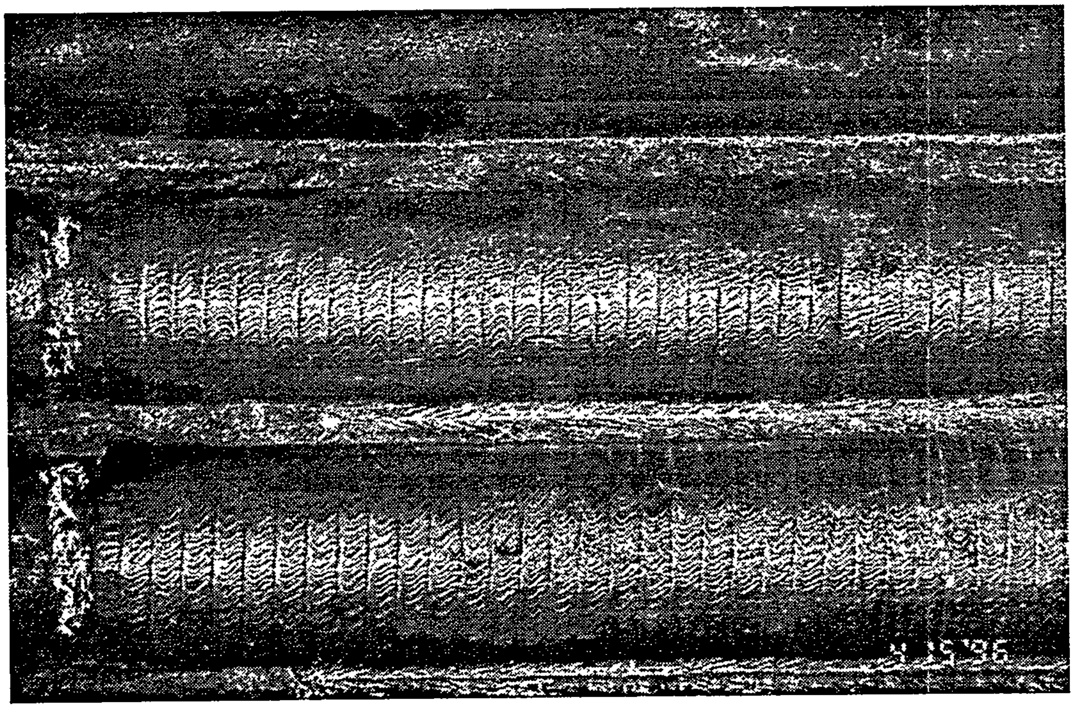

Fig. 4: Spiral Weld Clad Tubing

- Plate thicknesses can be successfully welded under proper conditions.
- Industrial service testing in recovery boilers is continuing.
- Wire arc cladding is being developed as an alternative to conventional weld overlay cladding.
- Spiral weld cladding is being investigated as a replacement for coextruded bimetallic tubing.

REFERENCES

1. T. Zacharia and S.A. David, *"Weldability of Iron Aluminides,"* proceedings of the Fifth Annual Conference on Fossil Energy Materials, ORNL/FMP-91/1, Oak Ridge National Laboratory, September 1991.

2. T. Zacharia, P.J. Maziasz, S.A. David, and C.G. McKamey, *"Weldability of Fe_3Al Based Iron Aluminide Alloys,"* proceedings of the Sixth Annual Conference on Fossil Energy Materials, ORNL/FMP-92/1, Oak Ridge National Laboratory, July 1992.

3. G.M. Goodwin, C.G. McKamey, P.J. Maziasz, and V.K. Sikka, *"Weldability of Iron Aluminides,"* proceedings of the Seventh Annual Conference on Fossil Energy Materials, ORNL/FMP-93/1, Oak Ridge National Laboratory, July 1993.

4. G.M. Goodwin, P.J. Maziasz, C.G. McKamey, J.H. Devan, and V.K. Sikka, *Weldability of Iron Aluminides,"* proceedings of the Eighth Annual Conference on Fossil Energy Materials, ORNL/FMP-94/1, Oak Ridge National Laboratory, August 1994.

5. G.M. Goodwin, *"Weld Overlay Cladding With Iron Aluminides,"* proceedings of the Ninth Annual Conference on Fossil Energy Materials, ORNL/FMP-95/1, Oak Ridge National Laboratory, August 1995.

6. G.M. Goodwin, *"Weld Overlay Cladding with Iron Aluminides,"* proceedings of the Tenth Annual Conference on Fossil Energy Materials, ORNL/FMP-96/1, Oak Ridge National Laboratory, August 1996.

7. Welding Handbook, **2**, Eighth Ed., pp. 872-74, American Welding Society, Miami, Fla., 1991.

CERAMIC MEMBRANES FOR HIGH TEMPERATURE HYDROGEN SEPARATION

K. D. Adcock, D. E. Fain, D. L. James, L. E. Powell, T. Raj,
G. E. Roettger, and T. G. Sutton

East Tennessee Technology Park
P. O. Box 2003
Oak Ridge, TN 37831-7271

ABSTRACT

The separative performance of our ceramic membranes has been determined in the past using a permeance test system that measured flows of pure gases through a membrane at temperatures up to 275°C. From these data, the separation factor was determined for a particular gas pair from the ratio of the pure gas specific flows. An important project goal this year has been to build a Mixed Gas Separation System (MGSS) for measuring the separation efficiencies of membranes at higher temperatures and using mixed gases.

The MGSS test system has been built, and initial operation has been achieved. The MGSS is capable of measuring the separation efficiency of membranes at temperatures up to 600°C and pressures up to 100 psi using a binary gas mixture such as hydrogen/methane. The mixed gas is fed into a tubular membrane at pressures up to 100 psi, and the membrane separates the feed gas mixture into a permeate stream and a raffinate stream. The test membrane is sealed in a stainless steel holder that is mounted in a split tube furnace to permit membrane separations to be evaluated at temperatures up to 600°C. The compositions of the three gas streams are measured by a gas chromatograph equipped with thermal conductivity detectors. The test system also measures the temperatures and pressures of all three gas streams as well as the flow rate of the feed stream. These data taken over a range of flows and pressures permit the separation efficiency to be determined as a function of the operating conditions. A mathematical model of the separation has been developed that permits the data to be reduced and the separation factor for the membrane to be determined.

INTRODUCTION

The primary purpose of this project is to develop methods for producing highly efficient gas separation membranes for separating hydrogen from gasified coal at temperatures of 1000°F (538°C) or higher. This work has been focused on the development of alumina membranes having extremely small pores that can separate gas molecules on the basis of molecular size, i.e., by molecular sieving. A hard sphere diffusion model was developed earlier, which provided a basis for estimating the extremely high separation factors that should be achievable (for a binary gas mixture) as the membrane mean pore size is reduced and approaches the molecular diameter of the larger gas molecule.[1] Since ceramic membranes typically have some pores that are substantially larger than the mean pore size, a more recent study modeled the effects of oversized pores on the performance of gas separation membranes and showed the importance of limiting the size and frequency of such oversized pores.[2]

In our membrane development work, alumina membranes having estimated mean pore diameters as small as 5 Angstroms have been produced and tested, and very high separation factors have been measured.[3] The separation factors of our ceramic membranes have been determined to date from pure gas flow data measured at several temperatures up to a maximum of 275°C. An important project goal for FY 1997 has been to build a new test system for measuring the separation efficiencies of membranes at much higher temperatures and using mixed gases.

DISCUSSION OF CURRENT ACTIVITIES

Mixed Gas Separation System

A Mixed Gas Separation System (MGSS) has been designed and built at the East Tennessee Technology Park to provide the capability to measure separation efficiencies of membranes with mixed gas streams of interest at temperatures up to 600°C and pressures up to 100 psi. Construction, calibration, and startup of the MGSS have been completed. An initial membrane has been installed in the test system, and it is being tested to check out and verify overall system operations. The primary purpose of the MGSS is to evaluate the ability of membranes to separate gases. That can be done most effectively using a binary gas mixture. The test system can also be used to evaluate the functional performance of membranes with gas mixtures containing many gases.

Description of the MGSS

A diagram of the new test system is shown in Fig. 1, and a view of the completed system is shown in Fig. 2. In this test system, the membrane separates the constituents of a binary gas mixture that normally contains hydrogen as one of the constituents. A mixture of gases, such as hydrogen and methane, are supplied to the test system from compressed gas cylinders. The test gases are passed through a molecular sieve dryer to remove residual water. The test gas is then metered, and the flow rate measured, by one of four orifices that are sealed in an orifice manifold. The gas mixture flows through stainless steel tubing that passes through a preheater that heats the gas to approximately the desired test temperature. The heated gas flows immediately into a split-tube furnace (Fig. 3) where the temperature is accurately controlled at any specified temperature up to 600°C.

The membrane being tested is sealed in a stainless steel holder (Fig. 4) located at the center of the split-tube furnace. The test gas mixture, e.g., hydrogen and methane, flows into the feed end of the tubular membrane. As the gas flows axially through the membrane, the smaller gas molecules (i.e., hydrogen) preferentially pass through the ultra-small pores in the wall of the molecular sieve membrane. This provides a permeate stream containing a higher concentration of hydrogen. The raffinate stream flowing out the exit end of the tubular membrane contains a reduced concentration of hydrogen but an increased concentration of methane.

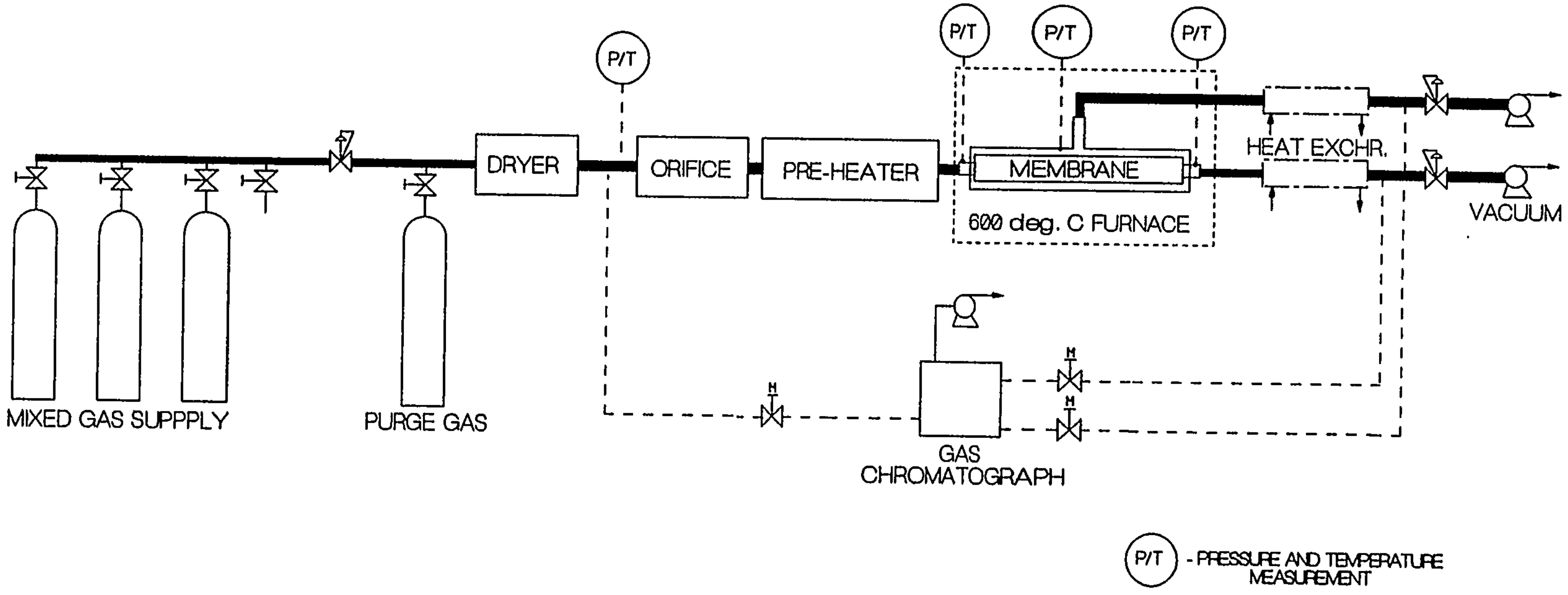

Fig. 1. Diagram of the Mixed Gas Separation System that has been built to measure the separation efficiency of membranes at temperatures up to 600 degrees C.

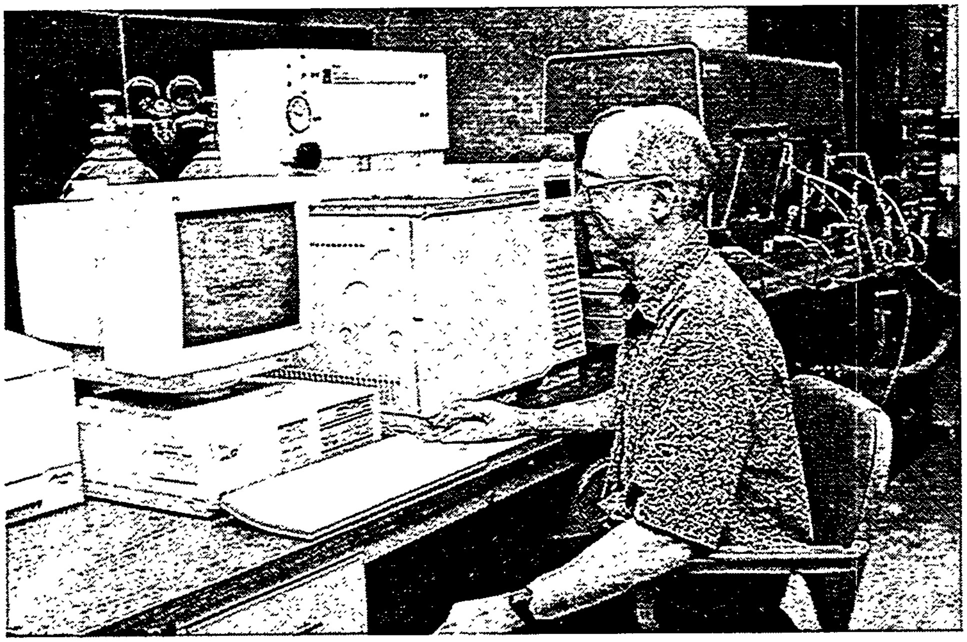

Fig. 2. Recently completed Mixed Gas Separation System.

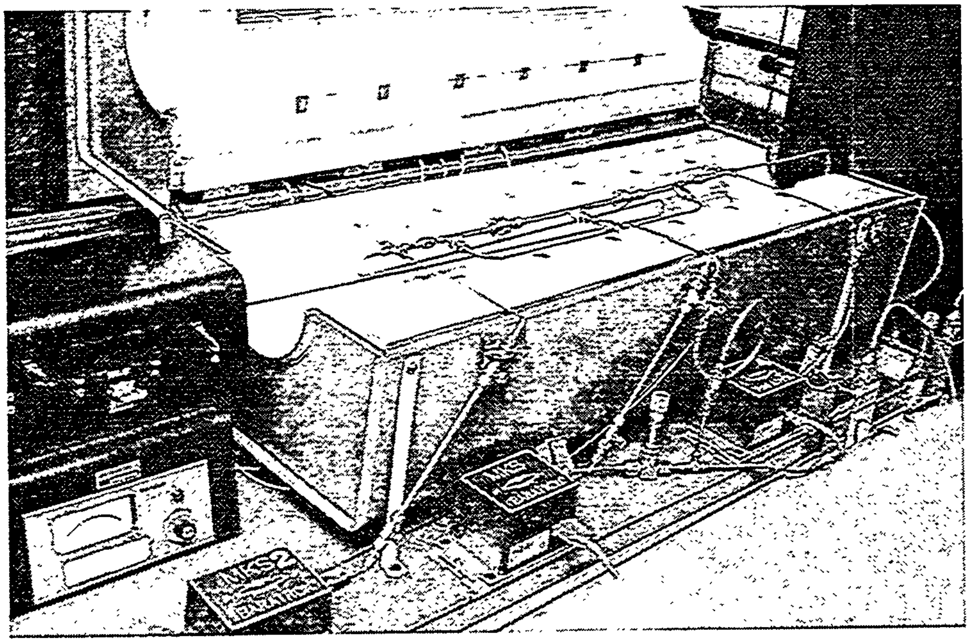

Fig. 3. Split tube furnace containing membrane holder that permits membrane separations to be evaluated at temperatures up to 600°C.

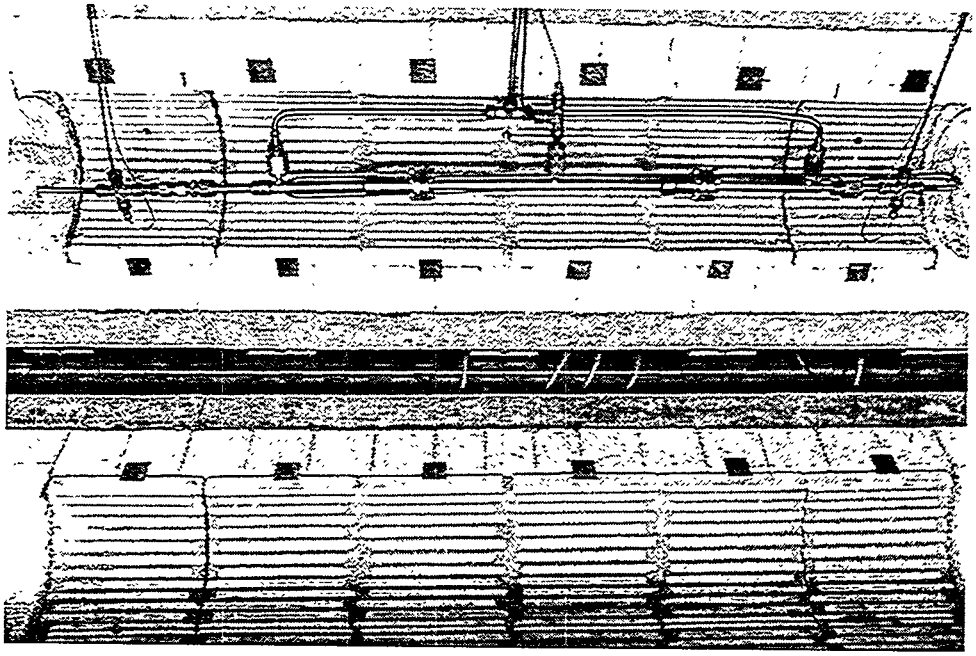

Fig. 4. Stainless steel holder containing membrane being tested in the MGSS.

The temperatures and pressures of the feed, permeate, and raffinate streams are measured by thermocouples and pressure transducers. Pressure taps and thermocouples are sealed into the tubing that connects to the two ends of the membrane holder as well as in the shell (permeate stream) of the holder as can been seen in Fig. 4. The feed, permeate, and raffinate streams are periodically sampled and analyzed by a gas chromatograph (Fig. 5) with thermal conductivity detectors (TCDs) to determine the compositions of the three gas streams. Data from all the measuring devices are collected, stored, and displayed on a dedicated computer. These data are reduced to determine the separation factor of the membrane.

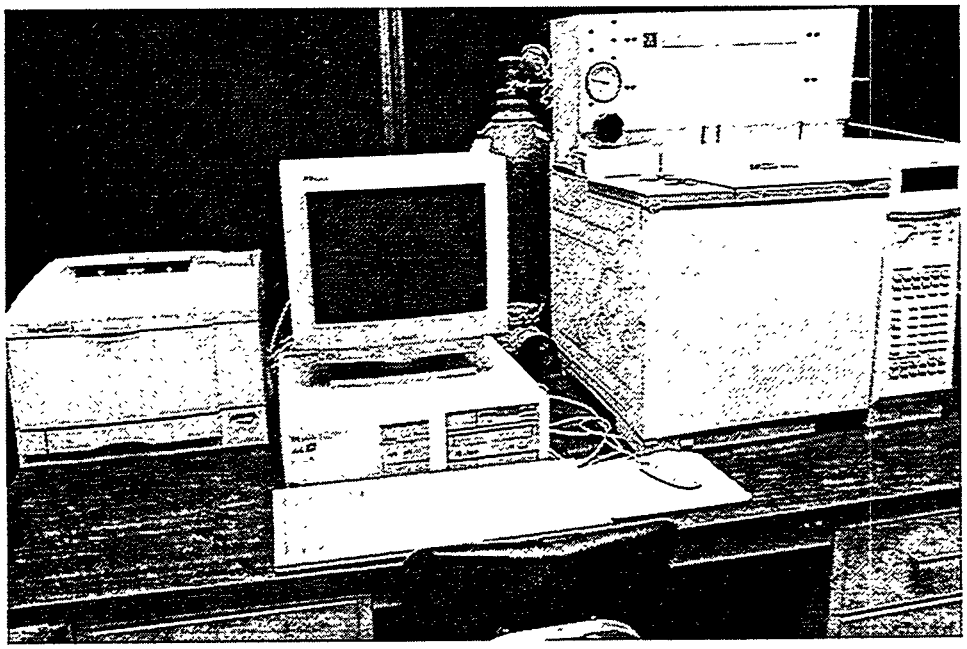

Fig. 5. Gas chromatograph used to analyze composition of feed, permeate, and raffinate streams.

Model for Data Evaluation

Introduction

The major function of our MGSS is the evaluation of fundamental characteristics of membranes. In many cases, a separation system is used to measure practical separations for evaluation of commercial applications. There are some basic differences in the design of systems for these two purposes. If the separation system is to be used only to evaluate potential commercial applications, it is a simple matter of measuring the performance of a membrane at some specified operating conditions. In this case, the mole fractions of the feed, permeate, and raffinate streams are measured directly and compared with results from other membranes or other processes.

The usual procedure to learn fundamental characteristics of membranes is to measure the flow of individual pure gases. The ideal separation factor, f*, (a fundamental membrane characteristic) is then the ratio of the specific flows [molar flow/(area x time x pressure drop)] of the individual gases. This assumes no interaction between the different molecules. However, interaction is likely except in very special limits, therefore, it is important to actually measure the separation with mixtures of gases.

The ideal maximum difference in mole fraction between the permeate and feed streams can be expressed by the relation,

$$\Delta C^* = \frac{C_1(1 - C_1)(f^* - 1)(1 - w)}{f^*(1 - C_1) + C_1} \quad .$$

The measured value is $\Delta C = C_1 - C_0$.

A good measure of membrane performance is $\Delta C/\Delta C^*$.

In these equations, C_0 is the feed mole fraction and C_1 is the permeate mole fraction, and w is the ratio of permeate pressure to the feed pressure.

The evaluation of data from a separation system can be complicated by many factors; for example, momentum exchange between molecular species which is generally proportional to the pressure drop across the membrane. It is also related to the recovery fraction or to the ratio of permeate to feed flow rate, herein referred to as the cut. The separation can also produce concentration polarization, which reduces the effect of the membrane separation factor. Separation data must be acquired in such a way that the data can be extrapolated to meaningful results. Therefore, the MGSS was designed and constructed to allow a wide range of operating conditions to provide for a significant range in recovery or cut and pressure and temperature to allow accurate extrapolation.

Information about the membrane can be acquired by measuring the mole fractions of all three streams as a function of the cut for several appropriate pressure drop levels. For a fixed pressure drop, the ratio of the mole fraction change between the feed and the permeate streams to the change expected for an ideal separation factor is plotted against the cut and extrapolated to zero cut. An example of such an evaluation is shown in Fig. 6. In this example, it was assumed that there was no concentration polarization. The values

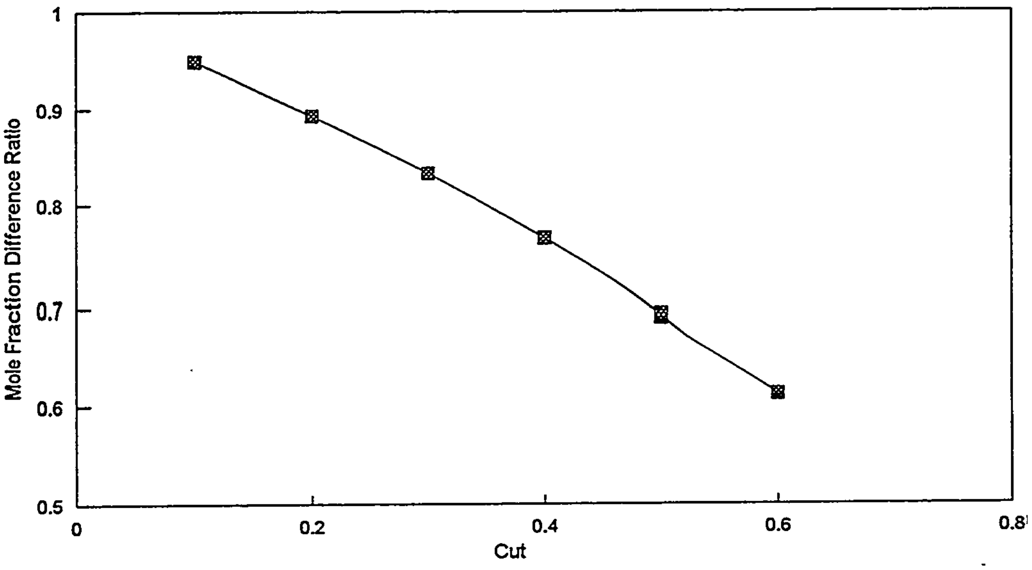

Fig. 6. An example of the membrane performance factor as a function of cut assuming no concentration polarization.

obtained at zero cut are then plotted against the pressure drop as shown in Fig. 7. The value extrapolated to zero pressure drop will be indicative of the real separation factor compared to the ideal separation factor. Such an evaluation requires a large amount of experimental data, but also provides significant information about the variation in separation factor as a function of operating parameters.

Computational Fluid Dynamic Calculations

A more explicit method is being developed to evaluate the separation factor directly. A computational fluid dynamic algorithm is being adapted to make direct calculation of the separation factor at various operating conditions. This will significantly reduce the amount of experimental data needed for the membrane evaluation and will give more insight into the dynamics of the separation process. Once perfected, it can also be used to optimize the economic operation of a membrane in a given separation system.

Boundary conditions have been established for the problem, and procedures are being developed for performing iterative calculations to determine a separation factor that will produce the measured feed, permeate, and raffinate stream mole fractions.

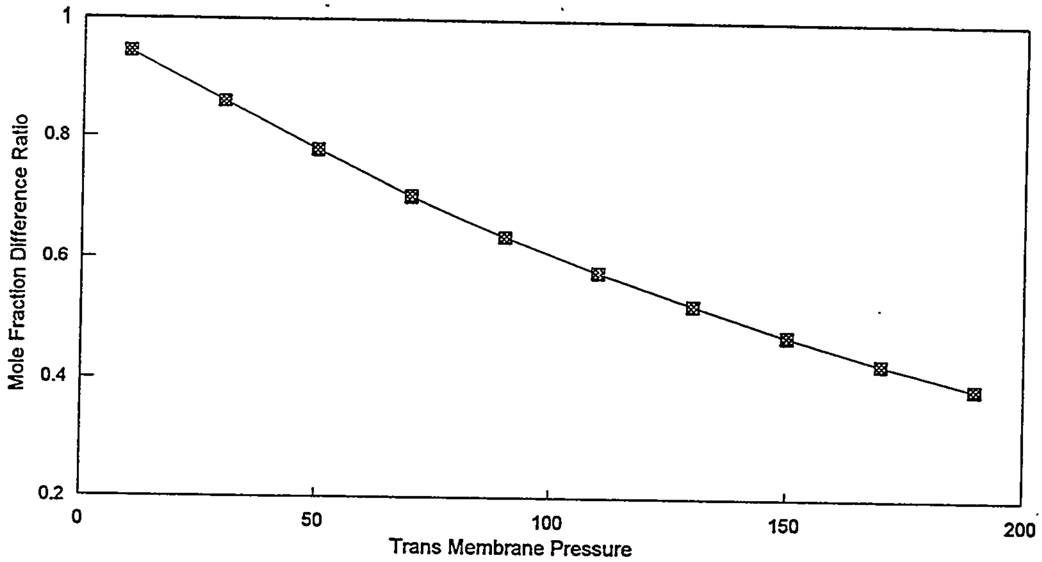

Fig. 7. An example of the membrane performance factor as a function of pressure difference across the membrane.

The current startup tests being conducted with the MGSS are providing data to check out and verify the overall system operation and provide data to use with these data reduction models.

REFERENCES

1. D. E. Fain and G. E. Roettger, "Coal Gas Cleaning and Purification with Inorganic Membranes," *Transactions of the ASME*, 115 (3), pp. 628-633 (July 1993).

2. G. E. Roettger and D. E. Fain, *Effects of Leaks on Gas Separation Performance of Nano Pore Size Membranes*, K/TSO-24, Lockheed Martin Energy Systems, Inc. Oak Ridge, K-25 Site, Oak Ridge, Tennessee, October 1996.

3. D. E. Fain and G. E. Roettger, "High Temperature Inorganic Membranes for Separating Hydrogen," in *Proceedings of the Ninth Annual Conference on Fossil Energy Materials*, Oak Ridge, Tennessee, May 16-18, 1995, pp. 185-193.

HIGH-TEMPERATURE CORROSION BEHAVIOR OF IRON-ALUMINIDE ALLOYS AND COATINGS

P. F. Tortorelli, B. A. Pint, and I. G. Wright

Oak Ridge National Laboratory
Oak Ridge, Tennessee, U. S. A.

ABSTRACT

The long-term oxidation performance of ingot- and powder-processed Fe-28 at.% Al-(2-5)% Cr alloys with minor oxygen-active element or oxide additions was characterized for exposures in air at 1000-1300°C. Additions of Zirconium or yttria substantially improved the adhesion of alumina scales grown on iron aluminides. At lower temperatures, the ingot-processed alloys performed similarly to ODS Fe_3Al alloys and other alumina-formers. However, at 1200 and 1300°C, the oxidation resistance of the ingot-processed Fe_3Al was degraded due to deformation of the substrate and some localized reaction product growth. Other oxidation experiments showed that the addition of an oxide dispersion to iron aluminides reduced the critical aluminum concentration for protective alumina scale formation. Oxide-dispersion-strengthened Fe_3Al alloys made from commercially prepared powders and an iron-aluminide coating with 21% Al and 1% Cr, prepared by a gas metal arc weld-overlay technique, showed excellent oxidation/sulfidation resistance.

INTRODUCTION

Iron aluminides containing greater than about 20-25 at.% Al have oxidation/sulfidation resistance at temperatures well above those at which these alloys have adequate mechanical strength.[1,2] In addition to alloying and processing modifications for improved creep resistance of wrought material, this strength limitation is being mitigated by development of oxide-dispersion-strengthened (ODS) iron aluminides[3,4] and by evaluation of Fe_3Al alloy compositions as coatings or claddings on higher-strength, less corrosion-resistant materials.[5-9] As part of these efforts, the high-temperature oxidation and oxidation-sulfidation behaviors of iron-aluminide weld overlays and ODS alloys are being characterized and compared to results for ingot-processed material. Other recent oxidation results for ODS Fe_3Al, as related to lifetime prediction, can be found elsewhere.[4]

OXIDATION OF Fe_3Al ALLOYS

The long-term oxidation performance of ingot- (I/M) and powder-processed (P/M) Fe-28% Al-(2-5)% Cr alloys was characterized for isothermal and cyclic exposures in air at 1000-

The submitted manuscript has been authored by a contractor of the U. S. Government under contract no. DE-AC05-96OR22464. Accordingly, the U. S. Government retains a nonexclusive, royalty-free license to publish or reproduce the published form of this contribution, or allow others to do so, for U. S. Government purposes.

1300°C. (All compositions are in at.%.) The P/M alloys were prepared by mechanically blending powders of gas-atomized Fe-28% Al-2% Cr (FAS) and submicron oxides in a flowing Ar atmosphere using a high-speed attritor and stainless steel balls.[3,10] The blended powder was canned, degassed, and extruded at 1100°C. For comparison, ingot-processed Fe-28% Al-2 or 5% Cr alloys and a commercial ZrO_2-dispersed (0.06% Zr) Fe-20% Cr-10% Al composition (Kanthal alloy APM) were also oxidized. The APM alloy is used as the benchmark for oxidation resistance as it typically displays low scale-growth and spallation rates at high temperatures under both isothermal and thermally cycled conditions.[11]

As illustrated in Figs. 1-4, the I/M Fe-28% Al-2% Cr (denoted FASN in this paper) consistently showed rapid weight gain kinetics under cyclic oxidation conditions at 1000-1300°C. At 1000°C (Fig. 1) and 1100°C (Fig. 2), Fe-28% Al-5% Cr-0.1% Zr (FAL) and P/M FAS-Y_2O_3 displayed similar oxidation resistance. However, while not apparent from the gravimetric data in Fig. 2, the alumina scales that developed on FAL and FAS-Y_2O_3 at 1100°C showed different characteristics: after about 500 h, the product on the former was thicker, more convoluted, and cracked on cooling, while the oxide on the latter showed a greater spallation tendency. Nevertheless, comparison of the data for these alloys to those for FASN clearly indicates that additions of zirconium or yttria substantially improved the adhesion of alumina scales grown on iron aluminides. These results are not unexpected;[2,9,12] the present observations simply reinforce the importance of small amounts of oxygen-active elements, and oxides based on the same, in improving oxidation resistance.[13] The two iron aluminides with such dopants had oxidation rates comparable to that of ZrO_2-dispersed FeCrAl (APM) at 1000°C (Fig. 1). At 1100°C (Fig. 2), APM showed superior oxidation resistance.

While the oxidation resistance of FAL was about the same as that of the FAS-Y_2O_3 at 1000 and 1100°C, significant differences between these two alloys were noted at 1200 and 1300°C (see Figs. 3 and 4). At these temperatures, the aluminum consumption rate, as measured by the total weight gain (that of the specimen as well as any oxide that has spalled) was higher for the FAL alloy. (With respect to the data shown in Fig. 4, the FAS-Y_2O_3 specimen went into breakaway oxidation[14] before the FAL simply because it was about half the thickness of the latter and thus had a substantially smaller aluminum reservoir to continually form protective Al_2O_3.[15-17]) This difference in oxidation behavior between the FAL and FAS-Y_2O_3 alloys may be at least partially explained by some localized inward growth of alumina observed for the former specimens (see Fig. 5). These areas of accelerated reaction could possibly be related to sites of casting/forming defects.

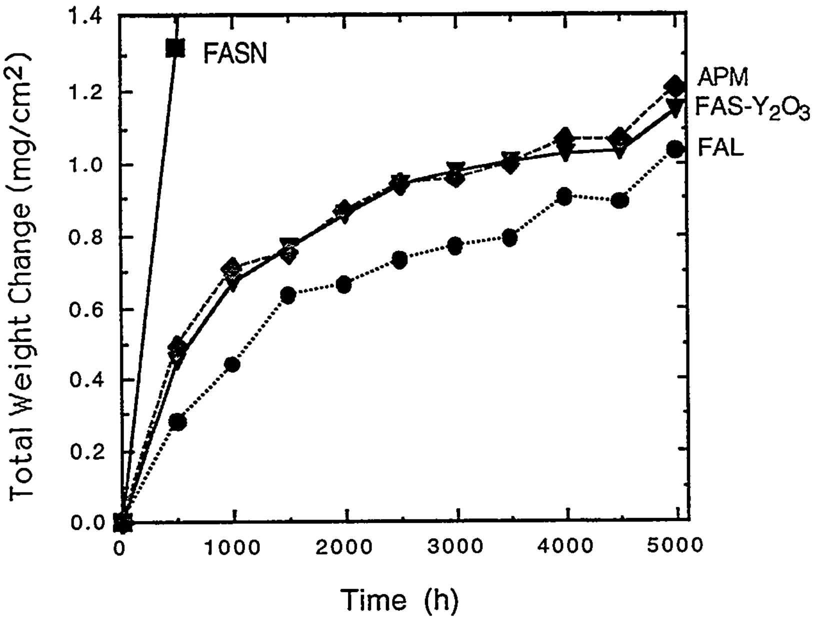

Fig 1. Total weight gain (specimen + spall) for 500-h cycles at 1000°C in laboratory air.

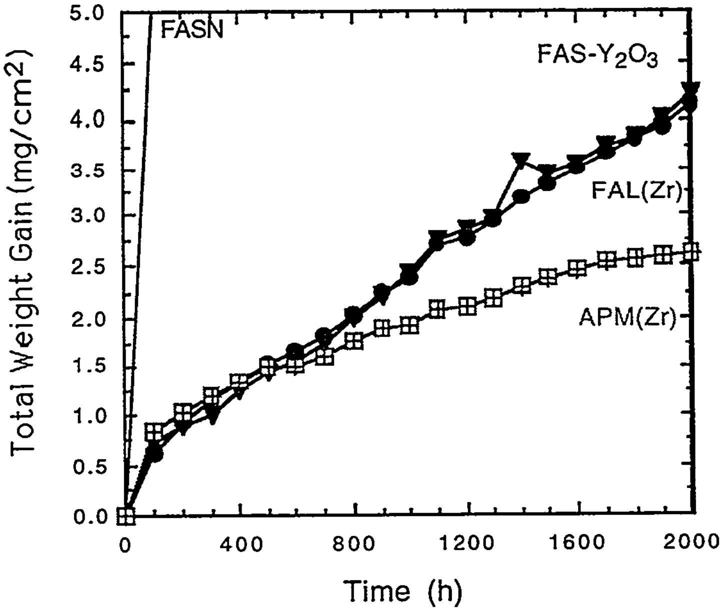

Fig. 2. Total weight gain (specimen + spall) for 100-h cycles at 1100°C in laboratory air.

A second factor contributing to the higher oxidation rate of FAL very well may be substrate strength. While the creep strengths of these alloys have not been determined, it appeared from evaluation of the as-oxidized specimens that the I/M FAL was weaker than the P/M Y_2O_3-containing FAS in that it was more easily deformed during high-temperature oxidation. Evidence for such has been shown previously for 1300°C oxidation[15,18] and from

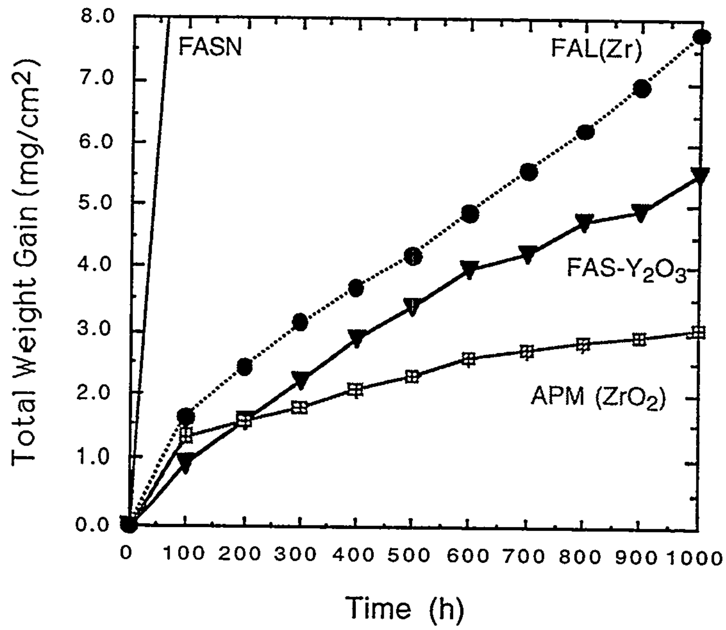

Fig. 3. Total weight gain (specimen + spall) for 100-h cycles at 1200°C in laboratory air.

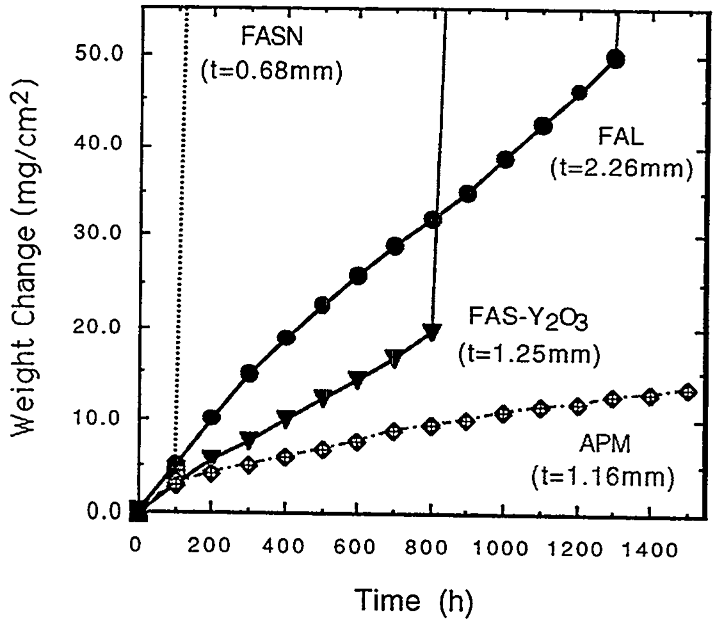

Fig. 4. Total weight gain (specimen + spall) for 100-h cycles at 1300°C in laboratory air. Starting specimen thicknesses (t) are noted.

the present experiments at this temperature. For example, Fig. 5 shows that the growth of alumina on FAL apparently significantly deformed the substrate. This ultimately results in a highly convoluted and cracked alumina scale. This deformation compromises the ability of the alumina scale formed on FAL to fully protect the substrate from reaction with the oxidizing

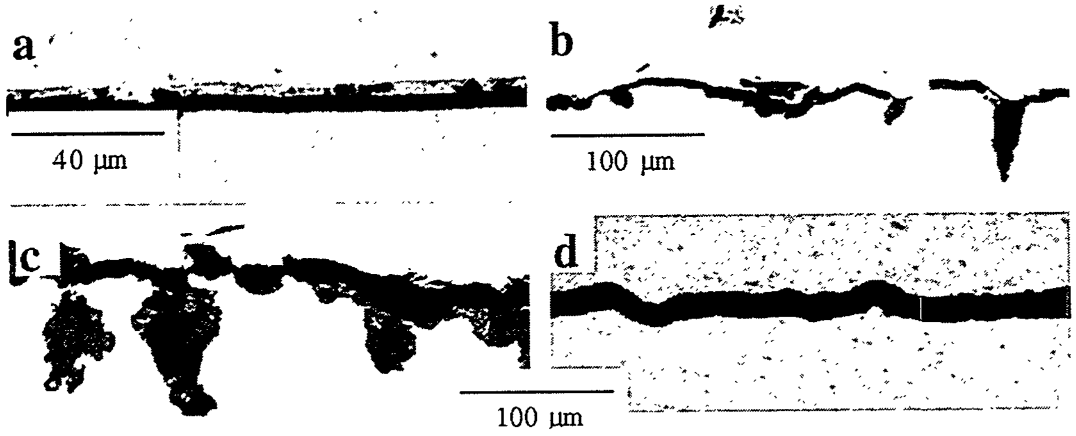

Fig. 5. Optical micrographs of cross sections of alumina-forming alloys exposed isothermally for 100 h in laboratory air (a) - (c) FAL, 1300°C; (d) APM, 1200°C. Specimens were coated with copper (upper light area) before sectioning. Comparison of (b) and (d) shows the scale grown on FAL is convoluted while the oxide on APM is relatively flat. Intermittent inward growth of alumina can be seen in (b) and (c).

species. Observations of a FAL specimen oxidized at 1200°C using 1-h cycles revealed similar scale convolutions and cracking. In contrast, the ODS iron aluminides exposed under the same conditions tended to show scale spallation due to interfacial void formation.

Although Y_2O_3 in FAS and Zr in FAL have beneficial effects on oxidation resistance, previous and present results indicate that these dopants are not as effective in the iron aluminides as when they are added to FeCrAl and β-NiAl.[18] As shown in Figs. 1-5, neither of these additions resulted in oxidation behavior as good as that of APM at 1100°C and above. The APM alloy remained relatively flat and the substrate-oxide interface was void-free (Fig. 5d). The reasons for the variations in oxidation performance between these different alumina-forming alloy systems are not known, but substrate strength and associated effects on scale buckling and void formation[18] are probably contributing factors.

As the high-temperature corrosion resistance of iron aluminides critically depends on the ability to grow and maintain a protective alumina layer, the minimum aluminum concentration necessary for formation of a continuous Al_2O_3 scale in air (c_{Al}) has been determined to be approximately 19% for I/M Fe-Al(-Cr) alloys.[19] As shown by the solid circles in Fig. 6, aluminum concentrations lower than this value lead to substantially greater weight gains for similar oxidation conditions. For 100-h exposures at 900°C, it was found that the oxidation product contained significant amounts of iron oxide and thus was not protective when weight gains were greater than about 1 mg/cm^2. Using weight gain as an indicator of alumina formation, it has been shown that c_{Al} for selected ODS (P/M) Fe_3Al alloys was lower than the value determined for I/M Fe-Al(-Cr) alloys . This shift in c_{Al} is illustrated in Fig. 6,

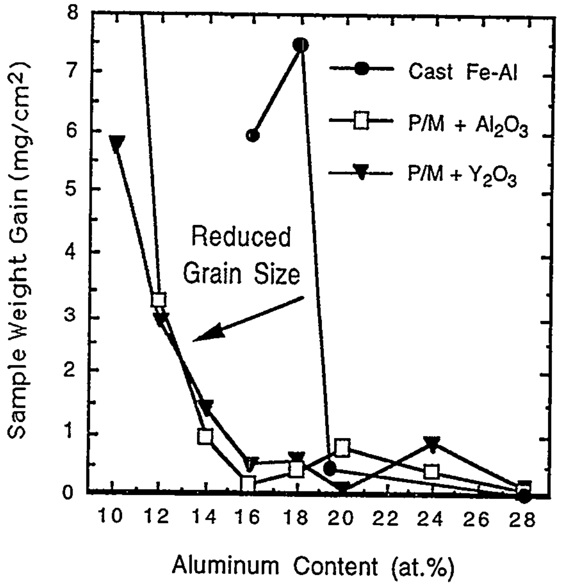

Fig. 6. Specimen weight change versus aluminum content after 100 h in air at 900°C for P/M and I/M Fe-Al alloys.

which shows that the critical aluminum concentration for the P/M alloys was ~13%. The addition of Y_2O_3 to the P/M alloy (which always contains a dispersion of Al_2O_3) did not significantly change this value. Similarities between Al_2O_3- and Y_2O_3-dispersed Fe-Al and c_{Al} values were observed from 600-1300°C.[20]

In attempting to explain the difference in c_{Al} between I/M and P/M versions of Fe_3Al alloys, the respective starting grain sizes of these materials must be considered. For the I/M alloys, average grain size is approximately 40 μm (or even larger) versus ~1 μm for the as-extruded P/M products. In addition, the oxide dispersions in the P/M alloys help to maintain the small grain size during elevated-temperature exposures. Because of this, the finer grain size of the P/M iron aluminides can promote more rapid transport of aluminum to the oxidizing surfaces. This would lower the apparent c_{Al} ,as the time to the onset of nonprotective oxide formation (breakaway) is also dependent on (proportional to) the diffusion coefficient of aluminum in the alloy.[14,16,17]

OXIDATION-SULFIDATION OF ODS Fe_3Al ALLOYS

Iron aluminides produced by conventional I/M procedures, have excellent sulfidation resistance in H_2S-containing environments.[2,19,21,22] Therefore, it has been of continuing interest to learn whether ODS iron aluminides show similar corrosion behavior. Preliminary data, obtained by exposing as-extruded P/M FAS and FAS-Y_2O_3 to 5.4% H_2S-79.4% H_2-1.6%

H_2O-13.6% Ar (by volume) showed that the oxidation/sulfidation rates of these iron aluminides were similar to that of many I/M Fe_3Al alloys.[9] Specifically, the isothermal weight gains of these P/M FAS alloys were somewhat greater than I/M FAS, but less than Fe_3Al-5% Cr produced by I/M processing. Subsequently, alloys of FAS-Y_2O_3 were produced from commercially-prepared powders.[4] These products were designated PMWY to distinguish them from the earlier ODS FAS-Y_2O_3 alloys; their detailed compositions and metallurgical characteristics are described elsewhere.[4] Specimen coupons were cut from recrystallized PMWY1 and PMWY2 (see ref. 4) and exposed to the same aggressive oxidizing/sulfidizing (H_2S-H_2-H_2O-Ar) environment at 800°C under both isothermal and thermal cycling conditions. The oxygen partial pressure, as determined by a solid-state oxygen cell, was 10^{-22} atm, and the sulfur pressure was calculated to be 10^{-6} atm. The isothermal results are shown in Fig. 7, which compares the thermogravimetric results for the PMWY alloys with similar data for I/M Fe_3Al alloys with 2 and 5% Cr and the previous as-extruded P/M FAS and FAS-Y_2O_3.[9] Note that the gravimetric curves for the PMWY alloys essentially mimic that for the benchmark I/M FAS composition. These weight gains are extremely low given the aggressiveness of the H_2S-H_2-H_2O-Ar gas. Indeed, under similar conditions, weight gains for Fe-20% Cr-10% Al alloys (such as APM) and stainless steels would be 1-3 orders of magnitude higher.[21,22] Furthermore, sulfidation resistance was maintained after a few thermal cycles; there was essentially no change in the rate of weight gain when a thermogravimetric experiment was periodically interrupted by cooling to room temperature and reheating to the exposure temperature.

The more rapid initial weight gains of the P/M FAS and FAS-Y_2O_3 specimens relative to those of the PMWY-1 and PMWY-2 in the oxidizing-sulfidizing environment may be related to grain size. It was previously hypothesized that the former alloys showed greater weight gains than the I/M FAS because their fine grain size allowed a more rapid diffusion of chromium to the reaction front and resulted in higher initial weight gains due to formation of chromium sulfides.[9] This argument may also explain the lower weight gains of the PMWY alloys shown in Fig. 7; the average grain size of the PMWY coupons was much larger than that of the as-extruded P/M FAS and FAS-Y_2O_3 specimens due to the recrystallization heat treatment.[4]

OXIDATION-SULFIDATION OF IRON-ALUMINIDE WELD OVERLAYS AT 800°C

This section contains corrosion data on weld deposits produced by gas metal arc (GMA) welding. Results for coatings produced by the gas tungsten arc (GTA) process as well as initial data for GMA overlays have been reported previously.[7,9] The development efforts associated

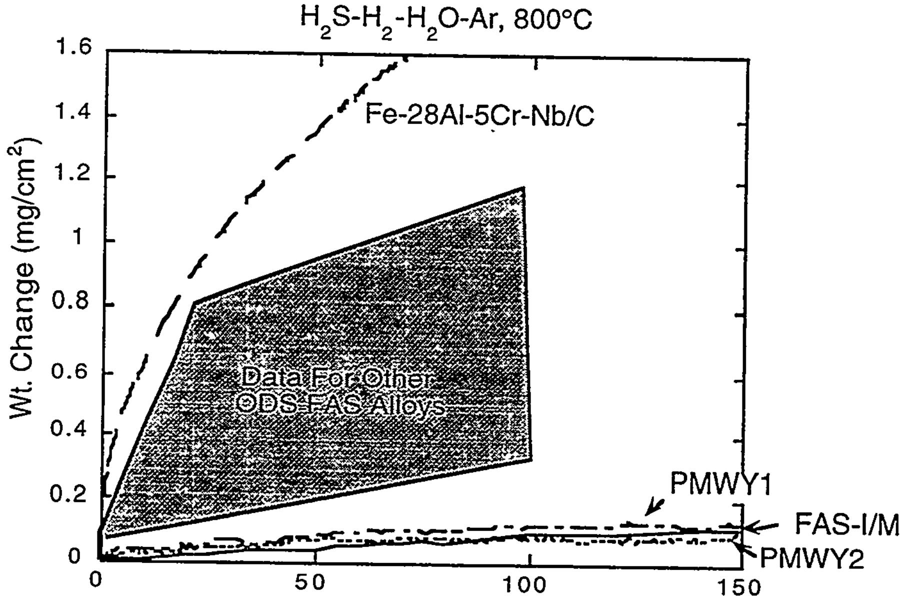

Fig. 7. Weight change versus time for specimens isothermally exposed to $H_2S-H_2-H_2O$-Ar at 800°C. The PMWY alloys are FAS-Y_2O_3 produced from commercially prepared powders and were exposed in the as-recrystallized condition. The specimen designated FAS-I/M was produced by ingot metallurgy processing and represents the benchmark behavior in this environment. The Fe_3Al - 5% Cr alloy was also produced by ingot metallurgy and contains 1% Nb and 0.2% C. The shaded area represents the range of data reported previously (see ref. 9) for as-extruded FAS and FAS-Y_2O_3 prepared from laboratory-produced powder mixtures.

with the GTA and GMA processes used to produce the weld overlays are described elsewhere.[5,6]

Weld overlays were deposited on Fe-2.25 Cr-1 Mo (wt%) steel substrates by GMA welding. As in previous oxidation-sulfidation studies,[7,9] coupons were prepared by cutting rectangular specimens from the overlay pad and then grinding away all the substrate material so that only weld metal (approximately 1-2 mm thick) remained. In this way, only the corrosion behavior of the weld deposit, rather than the coating/substrate system, is evaluated.[7,9] Oxidation-sulfidation behavior was characterized by use of a continuous-recording microbalance to measure the weight of these specimens during exposure at 800°C to the $H_2S-H_2-H_2O$-Ar mixed gas described above.

The use of welding to produce iron-aluminide coatings results in a loss of selected elements from the rod/wire by vaporization and significant mixing of the filler metal and substrate alloys (dilution) during deposition.[5,6] Because there is essentially no aluminum in the Fe-Cr substrates, the concentration of this element in the overlay is significantly less than in the weld rod/wire used to produce it. The extent of this dilution in aluminum depends on vaporization losses during welding and the relative amount of substrate material melted. Thus, it is affected by parameters such as current, voltage, polarity, travel speed, etc. When dilution is controlled such that the aluminum content of the weld deposit exceeds about 20%, good oxidation-sulfidation resistance results.[7,9] A GMA weld overlay with 21% Al and 1% Cr (denoted, for the purposes of this paper, as S2) consistently showed gravimetric behavior equivalent to the baseline FAS composition, which serves as the benchmark by which all other alloys are judged with respect to this mixed gas environment[21] (see Fig. 8). As shown in Fig. 9, S2 specimens showed better oxidation-sulfidation resistance than a previously examined GMA weld overlay[9] with the same Al level, but a significantly higher Cr concentration (because it was produced with a different weld wire). The deleterious effect of chromium on corrosion resistance in this environment is well documented,[2,21,22] and can explain the differences between the present and prior GMA results. Interestingly, as also shown in Fig. 9, the GMA S2 weld overlay had better oxidation-sulfidation resistance than a GTA one with 37% Al. This Al level normally offsets the deleterious effect of Cr,[21] so, in this case, there may be compositional inhomogeneity in the GTA weld overlay. As discussed previously,[9] the GMA process, which involves a substantially higher energy input into the weld, may promote more complete mixing of the deposit, and therefore result in more reproducible and better corrosion resistance in this environment than overlays produced by GTA.

The present results indicate that, in combination with a low chromium concentration, the aluminum level of the S2 weld overlay appears to be sufficient to show excellent corrosion

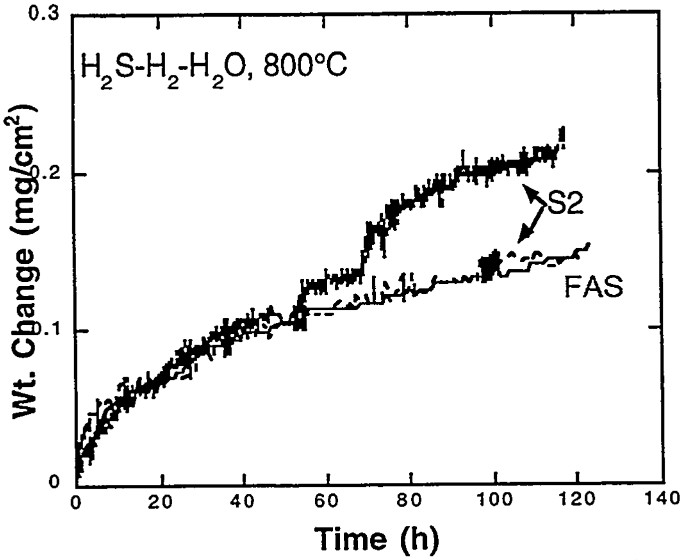

Fig. 8. Weight change versus time for I/M FAS and two specimens from a GMA weld overlay with a composition of Fe - 21% Al - 1% Cr (S2). Differences in behavior are negligible on this scale.

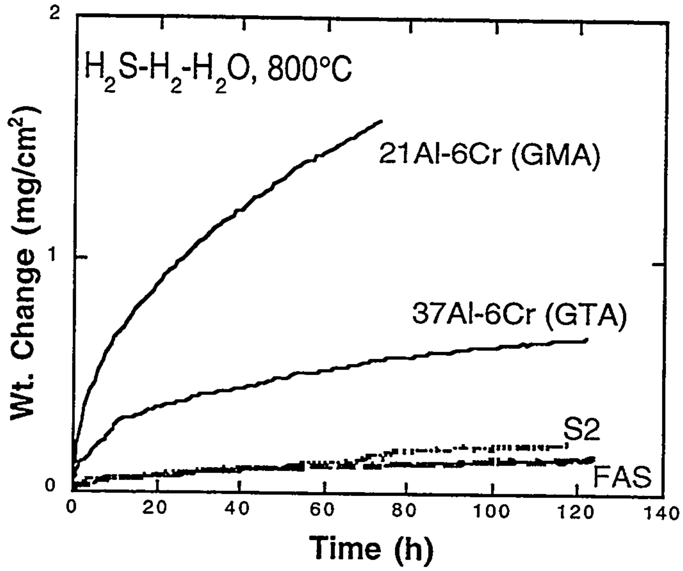

Fig. 9. Weight change versus time for I/M FAS and specimens from GMA and GTA weld overlays with compositions as shown. The curves designated S2 are the same as shown in Fig. 8 and are for a GMA weld overlay with a composition of Fe - 21% Al - 1% Cr. The FAS (I/M) curve is also the same as shown in Fig. 8.

resistance in an aggressive oxidizing/sulfidizing environment under isothermal conditions. However, aluminum concentrations of 20 - 21% are marginal with respect to maintaining low corrosion rates over extended periods of time, particularly if thermal cycling exacerbates the aluminum depletion process.[9] Weldability problems notwithstanding,[5,6] higher aluminum concentrations in the overlays would delay any onset of accelerated reaction caused by depletion of this element and improve the corrosion behavior of iron-aluminide coatings containing substrate elements, such as chromium and nickel, that are deleterious to sulfidation resistance (compare the 21Al-6Cr and 37Al-6Cr gravimetric curves in Fig. 9).[21,22]

SUMMARY AND CONCLUSIONS

The long-term oxidation performance of ingot- and powder-processed Fe-28 at.% Al-(2-5)% Cr alloys with minor oxygen-active element or oxide additions was characterized for exposures in air at 1000-1300°C. The oxidation-sulfidation behaviors of oxide-dispersion-strengthened Fe_3Al alloys and iron-aluminide weld overlays were also investigated.

Additions of zirconium or yttria substantially improved the adhesion of alumina scales grown on iron aluminides. At lower temperatures, the ingot-processed alloys performed similarly to ODS Fe_3Al alloys and other alumina-formers. However, at 1200 and 1300°C, the oxidation resistance of the ingot-processed Fe_3Al was degraded due to deformation of the substrate and some localized reaction product growth. Other oxidation experiments showed that the addition of an oxide dispersion to iron aluminides reduced the critical aluminum concentration for protective alumina scale formation.

Alloys of Fe-28 at.% Al-2% Cr-Y_2O_3 were produced from commercially-prepared powders and exposed to an highly aggressive oxidizing/sulfidizing (H_2S-H_2-H_2O-Ar) environment at 800°C under isothermal and thermal cycling conditions. The results from these experiments showed that these alloys had excellent oxidation/sulfidation resistance that was comparable to that of the ingot-processed version of the base alloy.

Iron-aluminide coatings were prepared by a gas metal arc weld-overlay technique. Specimens cut from the weld deposits were isothermally exposed to the H_2S-H_2-H_2O-Ar environment at 800°C. Excellent corrosion resistance was observed for a weld overlay with 21% Al and 1% Cr, but higher aluminum concentrations will be necessary to assure long-term performance in this environment, particularly under thermal cycling conditions.

ACKNOWLEDGMENTS

The authors thank M. Howell for experimental support and J. R. DiStefano, G. M. Goodwin, and J. R. Keiser for their reviews of the manuscript. This research was sponsored by the Fossil Energy Advanced Research and Technology Development (AR&TD) Materials Program, U S. Department of Energy, under contract DE-AC05-96OR22464 with Lockheed Martin Energy Research Corporation.

REFERENCES

1. C. G. McKamey, J. H. DeVan, P. F. Tortorelli, and V. K. Sikka, "A Review of Recent Developments on Fe_3Al-Based Alloys," *J. Mater. Res.* 6 (1991) 1779-1805.

2. P. F. Tortorelli and J. H. DeVan, "Compositional Influences on the High-Temperature Corrosion Resistance of Iron Aluminides," pp. 257-70 in Processing, Properties, and Applications of Iron Aluminides, J. H. Schneibel and M. A. Crimp (eds.), The Minerals, Metals, and Materials Society, Warrendale, PA, 1994.

3. I. G. Wright, B. A. Pint, E. K. Ohriner, and P. F. Tortorelli, "ODS Iron Aluminides," pp. 359-71 in *Proc. Tenth Annual Conf. Fossil Energy Materials*, N. C. Cole and R. R. Judkins (comp.), U. S. Department of Energy, August 1996.

4. I. G. Wright, B. A. Pint, P. F. Tortorelli, and C. G. McKamey, "Development of ODS Fe_3Al Alloys," these proceedings.

5. G. M. Goodwin, P. J. Maziasz, C. G. McKamey, J. H. DeVan, and V. K. Sikka, "Weldability of Iron Aluminides," pp. 205-10 in *Proc. Eighth Annual Conf. Fossil Energy Materials*, N. C. Cole and R. R. Judkins (comp.), CONF-9405143, U. S. Department of Energy, August 1994.

6. G. M. Goodwin, "Weld Overlay Cladding with Iron Aluminides," pp. 381-92 in *Proc. Tenth Annual Conf. Fossil Energy Materials*, N. C. Cole and R. R. Judkins (comp.), U. S. Department of Energy, August 1996.

7. P. F. Tortorelli, J. H. DeVan, G. M. Goodwin, and M. Howell, "High-Temperature Corrosion Resistance of Weld Overlay Coatings of Iron Aluminide," pp. 203-12 in Elevated Temperature Coatings: Science and Technology I, N. B. Dahotre, J. M. Hampikian, and J. J. Stiglich (eds.), The Minerals, Metals, and Materials Society, Warrendale, PA, 1995.

8. K. Natesan and R. N. Johnson, "Corrosion Performance of Fe-Cr-Al and Fe Aluminide Alloys in Complex Gas Environments," pp. 591-99 in Heat-Resistant Materials II, K. Natesan, P. Ganesan, and G. Lai (eds.), ASM International, August 1995.

9. P. F. Tortorelli, B. A. Pint, and I. G. Wright, "High-Temperature Corrosion Behavior of Coatings and ODS Alloys Based on Fe_3Al," pp. 393-403 in *Proc. Tenth Annual Conf. Fossil Energy Materials*, N. C. Cole and R. R. Judkins (comp.), U. S. Department of Energy, August 1996

10. B. A. Pint, K. B. Alexander, and P. F. Tortorelli, "The Effect of Various Oxide Dispersions on the Oxidation Resistance of Fe_3Al," pp. 1315-20 in High-Temperature Ordered Intermetallic Alloys VI, J. A. Horton, I. Baker, S. Hanada, R. D. Noebe, and D. S. Schwartz (eds.), The Materials Research Society, Pittsburgh, PA, 1995.

11. B. A. Pint, A. J. Garratt-Reed, and L. W. Hobbs, "The Reactive Element Effect in Commercial ODS FeCrAl Alloys ," *Mater. High Temp.* 13 (1995) 3-16.

12. B. A. Pint, "Study of the Reactive Element Effect in ODS Iron-Base Alumina-Formers," submitted for publication in *Mater. Sci. Forum,* 1996.

13. B. A. Pint, "Experimental Observations in Support of the Dynamic Segregation Theory to Explain the Reactive Element Effect," *Oxid. Met.* 45 (1996) 1-37.

14. P. Kofstad, High Temperature Oxidation, 1988.

15. J. H. DeVan, P. F. Tortorelli, and M. J. Bennett, "Environmental Effects on Iron Aluminides," pp. 309 - 20 in *Proc. Eighth Annual Conf. Fossil Energy Materials*, N. C. Cole and R. R. Judkins (comp.), CONF-9405143, U. S. Department of Energy, August 1994.

16. W. J. Quaddakers and M. J. Bennett, "Oxidation Induced Lifetime Limits of Thin Walled Iron Based Alumina Forming Oxide Dispersion Strengthened Alloy Components," *Mater. Sci. Technol.*, 10 (1994) 126-31.

17. M. J. Bennett, J. H. DeVan, and P. F. Tortorelli, "The Oxidation Behavior of Iron Aluminides in Air at 1300°C," accepted for publication in *Proc. Third Int'l. Conf. on Microscopy of Oxidation*, S. B. Newcomb and J. A. Little (eds.), The Institute of Materials, London, September 1996.

18. B. A. Pint, P. F. Tortorelli, and I. G. Wright, "The Oxidation Behavior of ODS Iron Aluminides," *Werkst. Korros.* 47 (1996) 663-74.

19. J. H. DeVan and P. F. Tortorelli, "Oxidation-Sulfidation Behavior of Iron Alloys Containing 16 to 40 Atomic Percent Aluminum," *Corros. Sci.* 35 (1993) 1065-71.

20. B. A. Pint and J. Lebowitz, Oak Ridge National Laboratory, unpublished results, 1996.

21. J. H. DeVan, "Oxidation Behavior of Fe_3Al and Derivative Alloys," pp. 107-115 in Oxidation of High-Temperature Intermetallics, T. Grobstein and J. Doychak (eds.), The Minerals, Metals, and Materials Society, 1989.

22. J. H. DeVan and P. F. Tortorelli, "Oxidation/Sulfidation of Iron-Aluminum Alloys," *Mater. at High Temp.* 11 (1993) 30-35.

CORROSION-RESISTANT COATING DEVELOPMENT

D. P. Stinton, D. M. Kupp, and R. L. Martin

ABSTRACT

SiC-based heat exchangers have been identified as the prime candidate material for use as heat exchangers in advanced combined cycle power plants. Unfortunately, hot corrosion of the SiC-based materials created by alkali metal salts present in the combustion gases dictates the need for corrosion-resistant coatings. The well-documented corrosion resistance of CS-50 combined with its low (and tailorable) coefficient of thermal expansion and low modulus makes CS-50 an ideal candidate for this application. Coatings produced by gelcasting and traditional particulate processing have been evaluated.

INTRODUCTION

Gelcasting of sodium-zirconium-phosphate (NZP) based materials[1-3] has been identified as a candidate process for applying high temperature, corrosion resistant coatings on to ceramic substrates. The gelcasting process, normally most useful in producing relatively large or complex ceramic or metallic monoliths, is being considered as a technique for applying conformal coatings to SiC composite heat exchanger tubes. The corrosion resistance of the $Ca_{0.5}Sr_{0.5}Zr_4P_6O_{24}$ (CS-50) material for the prescribed application has been well documented[4,5]. This characteristic, combined with its low (and tailorable) coefficient of thermal expansion (CTE) makes CS-50 an ideal candidate for evaluation in this application. The major hurdle has been in identifying an application technique which is both technically and economically feasible. While various chemical vapor deposition (CVD) and physical vapor deposition (PVD) techniques can be used to apply desirable coatings to idealized substrates, the complex composition of the coatings and the large size of the heat exchanger tubes (up to 15 feet long) makes the use of these techniques difficult and costly. Application techniques such as plasma spraying have also been tried with varying degrees of success.

By combining the attributes of polymer chemistry with those of traditional particulate processing, gelcasting has proven itself to be a viable contender in this area. However, while gelcasting of CS-50 based monoliths has proven to be relatively straightforward, the mechanical interaction of a gelcast body with a rigid substrate throughout the various processing steps addresses some of the most fundamental (and persistent) problems in traditional particulate processing (e.g. drying/sintering shrinkage and thermal expansion).

The development of an NZP-based coating was undertaken from a product development (rather than a scientific interest) point of view in an effort to maximize the amount of applicable progress made. Experiments were conducted using multivariate, small sample sizes. Since both the gelcasting process and the NZP type materials are well understood, it made sense to directly focus upon the new application, i.e. the gelcasting of NZP materials as a coating on a SiC/SiC composite substrate.

Since the gelcasting of CS-50 was previously proven to be feasible in standard gelcasting applications (i.e. monolithic geometries), an effort to improve the basic process was undertaken. The major problems envisioned in the process (and initially addressed) included:

1. Shrinkage of the CS-50 coating during processing leading to catastrophic failure of the coating.
2. Matching of the CTE of the coating to that of the substrate without detrimentally affecting other downstream processes.
3. Selection of a stable material systems which is non-reactive with the substrate and offers maximum corrosion protection.

From a fundamental standpoint, tailoring of the CTE of the coating to match that of the substrate is straightforward. By combining the CS-50 with a material having a CTE greater than that of the substrate in the proper ratios, a material system having the appropriate CTE could be customized. By approximating the CTE of the SiC ceramic matrix composite, the CTE of CS-50 can be increased to that of the SiC substrate by the correct addition of alumina for example. Trials evaluating various coating to substrate CTE ratios must be carried out to determine the optimal coating CTE.

One of the major obstacles in the application of a particulate coating on to a substrate is the accommodation of the shrinkage of the applied coating due to such things as polymer cross linking, drying, binder removal, etc. The most direct way of reducing such shrinkage is through the optimization of the particle packing or solids loading of the powder system (i.e. slurry) being used. While many complex models exist for predicting and interpreting particle packing behavior, it is sufficient for current purposes to simply maximize the amount of solid material per quantity of slurry liquid (water and/or liquid chemicals) while still maintaining a usable slurry rheology. By maximizing the solids loading level, more particle to particle contacts are generated, reducing shrinkage through particle rearrangement and increasing green strength.

Assuming a roughly equiaxed particle morphology where random particle orientation produces a more or less homogeneous, isotropic particle array, a solids loading level can generally be maximized by using a powder with a very narrow (i.e. monosized) or very broad particle size distribution. This distribution width, S_w, can be calculated from the following:

$$S_w = \frac{2.56}{\begin{matrix} d_{90} \\ d_{10} \end{matrix}} \qquad \text{where}$$

d_{90} = particle diameter equivalent to 90% of the cumulative distribution
d_{10} = particle diameter equivalent to 10% of the cumulative distribution

Ideally, the distribution width should be very wide (S_w # 2) or very narrow (S_w ∃ 7) to achieve maximum particle packing density (i.e. solids loading) in a slurry or green/fired component. Since it can be difficult and expensive to produce a monosized powder in reasonable quantities, a powder with a wide particle size distribution is generally more desirable. Since the base low expansion powder will likely be amended with a relatively high CTE material to develop a suitable coating CTE, intelligent selection of the "modifier" in terms of thermomechanical properties and particle size characteristics will also enhance the particle packing and rheological behavior of the powder system.

DISCUSSION

The processability and composition of the components of the corrosion resistant coating were the two basic concerns initially addressed. Sodium-zirconium-phosphate (NZP) material ($Ca_{0.5}Sr_{0.5}Zr_4P_6O_{24}$) was selected as the primary component based on its low CTE and excellent corrosion resistance[4,5]. As previously discussed, the CTE of the NZP material (grade CS-50 from LoTEC, Inc.) was selected as the base material to be amended by another corrosion resistant material in order to tailor the coating CTE. Alumina (grade RCHP/no MgO from Reynolds) was selected as the modifying material based on previous gelcasting performance and its generally excellent corrosion resistance. This specific grade of material has a fine median particle size (<1 Φm) which would enhance the packing and rheological behavior of a CS-50/alumina mixture. Initially, gelcasting of pure CS-50 was carried out to establish a baseline procedure for the NZP family of base materials. Prior art in the gelcasting of these materials established basic formulations and procedures. The standard monomer solution (which is crosslinked in a downstream process) was a 15 wt. % aqueous solution of a 6:1 ratio of MAM (methacrylamide) to MBAM (methylene bisacrylamide). This solution served not only as the polymeric precursor but also as the fluid in which the particulate materials were ball milled and mixed. Since it was critical to maximize the solids loading of the slurry (i.e. volume % ratio of solids to liquids), solids loading levels of the slurries began at ~ 50 vol.% and were gradually increased until the desired viscosity had been reached. Eventual solids loading levels of ~60 vol. % were reached for the pure CS-50 gelcastable slurry.

Milling was carried out in HDPE jars (~750 ml.) with 6 mm. diameter zirconia media. Darvan 821A was added to the precursor solution as a dispersant. Generally, gentle milling was carried out only to disperse, homogenize and wet the powder, not necessarily to modify the particle shapes or size distributions.

Once it was determined that an optimized solids loading level had been reached, the slurry was strained through a -325 mesh screen to remove media and dried mill residue. The slurry was then de-aired using a vacuum dessicator until a bubble-free slurry resulted. At this point the slurry is suitable to begin the casting procedure. A combination of crosslinking catalysts and accelerants [TEMED(tetramethylethyl diamine) and 10% aqueous solution of APS (ammonium persulfate)] is added to convert the monomer precursor solution to a polymeric binder. Since the kinetics of crosslinking is relatively slow (and controllable), time is available to pour the slurry into a mold before complete gelation of the binder/powder system occurs.

Since the gelcasting trials of the pure CS-50 composition were successful, preliminary efforts incorporating the CTE modifier, alumina, were started. By approximating the CTE of the SiC ceramic matrix composite to be ~ 4.5 x 10^{-6}/EC, the CTE of CS-50 (3.0 x 10^{-6}/EC) can be increased to that of the SiC substrate by the correct addition of alumina for example (CTE ~ 8.0 x 10^{-6}/EC). Using the rule of mixtures as a basis for formulation, a body comprised of 70 vol. % CS-50 / 30 vol. % Al_2O_3 (66 wt. % CS-50/34 wt. % Al_2O_3) was formulated, approximating the CTE of the SiC/SiC substrate.

A particle size analysis was completed on the CS-50 powder using a Horiba LA-700 particle size analyzer. The particle size distribution for the powder was bimodal (0.3 Φm and 20 Φm), with a mean particle size of ~ 13.4 Φm. The distribution width, S_w, is calculated to be ~1.4 (very wide). However, visually and to the touch, the powder seemed to contain a fraction of grit (i.e. large, hard agglomerates) which can be broken with moderate pressure. These agglomerates can also be disintegrated somewhat with intensive ultrasonic agitation. The mean particle size for a sample which received intensive agitation with an outboard ultrasonic horn was reduced by 17% from 13.4 Φm to 11.1 Φm with additional agitation (beyond that provided in the Horiba chamber prior to analysis). Furthermore, the percentage of particles greater than ~30 Φm decreased from 8.5 to 4.5%, likely due to the breaking up of the hard agglomerates.

After sustained, but gentle milling, the solids loading level and related rheological behavior of the CS-50 and alumina powder mix appears to be outstanding at 70 vol. % CS-50 / 30 vol. % alumina at 66 vol. % solids loading. Approximately 0.7 wt. % Darvan 821A (based on total solids) was added as a dispersant to the 70/30 slurry in the aqueous MAM/MBAM solution. Most notable from the particle size distribution is the lack of particles greater than 20 Φm in comparison to the standard and ultrasonically agitated slurries which show particle sizes for the as-received and sonicated CS-50 powder to be 60-75 Φm. It appears that the low intensity ball milling done to homogenize the powder/monomer slurry, is sufficient to break up the light aggregate suspected of existing in the as-received CS-50. Once the CS-50 powder is dispersed, along with the addition of 30 vol. % alumina, a very wide distribution width, Sw, of 1.51 is achieved. This wide distribution combined with the deagglomerated slurry components provides the basis for a high solids loading level (>66 vol. % solids). While the particle size distribution of the as-received CS-50 powder is also very wide (Sw = 1.46), the distribution appears to be an artifact of particle agglomeration and fines, not the true, primary particle size distribution measured after mechanical deagglomeration.

Two component slurries at 60/40, 70/30, 80/20 and 90/10 vol.% CS-50/alumina were prepared and evaluated for rheological behavior and powder co-processing behavior related to slurry additives (e.g. dispersants and anti-foaming agents) and critical solids loading levels. Samples 25 mm. x 25 mm. were gelcast and dried without apparent problems. Samples were processed through thermal binder removal (1EC/min. to 600EC, hold for 1 hour) and sintered in air at 1325EC for 4 hours without physical damage. Compositional analysis was not completed on any samples.

Since the processing of a gelcast CS-50/alumina monolith was successful for each composition, the application of a similar slurry to a SiC composite substrate was tried. SiC/SiC tube sections (25 mm. diameter x 20 mm. long) were dipped into each of the CS-50/alumina slurries which had been catalyzed but had not crosslinked. Multiple dips on different samples provided a variety of coating thicknesses for analysis of adhesion and cracking behavior through drying and firing steps. Freshly dipped samples were suspended in a relatively airtight container (since contact with air inhibits gelation) until gelation had completed and residual moisture had dried. After a standard binder burnout cycle was completed, the coated samples were heat treated at 1200EC (in air) for 5 days. While the sintering temperature for CS-50 based materials (especially when "alloyed" with alumina) is >1300EC, a maximum temperature of 1200EC was used to avoid degradation of the SiC composite. Relatively long sintering times were used to promote densification of the coating at the lower firing temperature and also to evaluate the thermomechanical performance of the coating.

Two distinct phenomena were investigated; coating thickness and composition. After long term firing, samples with coating thicknesses greater than about 2 mm. exhibited severe cracking throughout the surface of the coating in the form of continuous crazing, as well as deeper fissures appearing radially on the ends of the tube section. Other substantial cracking occurred on the circumference of the tube section, apparently as a result of the shrinkage of the particulate coating during drying and sintering. Thinner coatings (<1 mm.) did not exhibit the same cracking pattern as the thicker coatings, with only a thin crack occurring at the edge of the tube section (juncture between the tube end and outside diameter). Samples of the composition 90 vol.% CS-50 /10 vol.% alumina also showed reduced overall cracking due to proper tailoring of the CTE. In these cases, a continuous, adherent and somewhat densified coating was developed.

As a result of the improved adhesion and resistance to cracking associated with the reduced coating thickness, the gelcasting technique used to produce these coatings (and in general, much larger monolithic structures) was abandoned in favor of a much more straight forward "non-monomer" slurry approach. By utilizing a traditional aqueous slurry, the need for expensive and toxic monomer precursor materials was eliminated. Furthermore, the problem of gelation being inhibited by exposure to air is no longer an issue since the monomer crosslinking phase is no longer a requirement of the process. The air exposure limitation of gelcasting may have led to some costly and complicated engineering problems if larger tubes were ever to be coated.

As an initial characterization of the fired composite/coating sample, XRD was performed to determine the extent (if any) of the CS-50 degradation related to substrate exposure, prolonged high temperature use and/or the alloying with another material (i.e. alumina). Samples of 70 vol.% CS-50/30 vol.% alumina were prepared using a non-gelcasting slurry to dip coat SiC/SiC tube sections. Samples were dipped and dried followed by a binder burnout at 600EC./1hr. The coated tube sections were sintered at 900, 1000, 1100 and 1200EC for 48 hrs. A standard coating of pure CS-50 was also prepared identically and sintered at 1200EC for 48 hrs. XRD results (Figure 1) show the generation of an unidentified phase in the 70/30 sample at 1200EC. The intensity of this phase decreases with sintering temperature and does not exist in the pure CS-50 coating at 1200EC exposure. Furthermore, three low angle peaks (11-14E 22) which exist in the XRD trace for pure CS-50 at 1200EC decrease in intensity with increasing process temperature. While the XRD data is open to interpretation and is not fully completed, it does indicate that the addition of the alumina to the pure CS-50 as a CTE modifier reacts to form what may be an undesirable phase.

Without further analysis or actual corrosion testing to evaluate the performance of the unidentifiable phase(s), it was decided to consider modification of the CS-50 CTE with other materials such as:

1. 4% Y_2O_3 stabilized ZrO_2
2. 12% CeO stabilized ZrO_2
3. Cr_2O_3

Using established procedures and general compositions, the above materials were used to make three new slurries as follows: 90 vol.% CS-50/10 vol%. modifier at 65 vol.% solids loading. SiC composite tube sections were dip coated with each slurry and dried. Following binder burnout, the samples were heat treated at 1200EC for 4 days.

SUMMARY

Initial trials using alumina modified CS-50 indicated that a relatively thin coating of a 90 vol.% CS-50/10 vol. % alumina provided the best adhesion to the SiC tube section in addition to providing a relatively crack free, continuous coating. Corrosion tests were not performed on these samples, but x-ray diffraction indicated a possible degradation of the CS-50 or generation of a phase non-existent in the as-received raw materials. A new selection of CTE modifiers based on individual corrosion resistance replaced the alumina. Stabilized ZrO_2 and Cr_2O_3 were added to the CS-50 in the same relative volume fraction. It became apparent that it was not the matching of the coating and substrate CTEs, but the relative CTEs which were important. Therefore, as a convenient and comparable starting point, the 90/10 ratio of CS-50/CTE modifier was maintained. The ZrO_2 and Cr_2O_3 modified coatings processed well and remained intact through a 1200EC/5 day soak.

In general, the theory involving maximizing the solids loading of the slurry proved to be useful. Powder particle sizes can be modified "ad nauseum" if necessary to obtain a highly loaded slurry with desirable rheological characteristics. The viscosity of a given slurry is only important as it relates to the coating technique used to apply the slurry to the substrate. If the slurry is fluid enough to mix and/or mill and can be applied by the method of choice (e.g. dipping, painting, spraying etc.) with minimal dripping or deformation, then that is the most appropriate slurry rheology.

The deviation from gelcasting technology to more traditional particulate processing also simplifies the process tremendously. Not only are the expensive and somewhat toxic chemicals avoided, but such things as working time (until gelation) and processing techniques are streamlined as well. Preliminary XRD analysis of the CS-50 plus ZrO_2 and Cr_2O_3 coatings indicated much less degradation of CS-50 than for CS-50 plus Al_2O_3. Samples of each of the new compositions have been fabricated and are awaiting CTE determination and high temperature, flowing gas corrosion tests.

REFERENCES

(1) C.-Y. Huang, D. K. Agrawal, H. A. McKinstry, and S. Y. Limaye, "Synthesis and Thermal Expansion Behavior of $Ba_{1+x}Zr_4P_{6-2x}Si_{2x}O_{24}$ and $Sr_{1+x}Zr_4P_{6-2x}Si_{2-x}O_{24}$ Systems," *J. Mater. Res.*, 9, 2005(1994).

(2) S. Y. Limaye and R. Nageswaran, "Development of NZP Ceramic-Based "Cast-in-Place" Diesel Engine Port Liners," Final Report, LoTEC, Inc., West Valley City, UT, November 1994.

(3) T. B. Jackson, S. Y. Limaye, and W. D. Porter, "The Effects of Thermal Cycling onthe Physical and Mechanical Properties of [NZP] Ceramics"; pp. 63-80 in Ceramics Transactions, Vol. 52, *Low-Expansion Materials*. Edited by D. P. Stinton and S. Y. Limaye, American Ceramic Society, Westerville, OH, 1995.

(4) W. Y. Lee, D. P. Stinton, and D. L. Joslin, "Interaction of Low-Expansion NZP Ceramics with Na_2SO_4 at 1000EC," *J. Am. Ceram. Soc.*, 79, 484(1996).

(5) W. Y. Lee, K. M. Cooley, C. C. Berndt, D. L. Joslin, and D. P. Stinton, "High-Temperature Chemical Stability of Plasma-Sprayed $Ca_{0.5}Sr_{0.5}Zr_4P_6O_{24}$ Coatings on Nicalon/SiC Ceramic Matrix Composite and Ni-Based Superalloy Substrates," *J. Am. Ceram. Soc.*, 79, 2759(1996).